THE UNIVERSITY *of* LIVERPOOL

Development of Advanced Mathematical Morphology Algorithms and their Application to the Detection of Disturbances in Power Systems

Thesis submitted in accordance with the
requirements of the University of Liverpool
for the degree of Master of Philosophy (M.Phil)

in

Electrical Engineering and Electronics

by

Jie Zhu, B.(Eng.)

August 2017

Development of Advanced Mathematical Morphology Algorithms and their Application to the Detection of Disturbances in Power Systems

by

Jie Zhu

To my parents, to whom I owe everything.

Acknowledgements

My deepest gratitude goes first to Professor Q. H. Wu and Professor J. S. Smith, my supervisors, for their enthusiastic encouragement, kind support, and thorough guidance. They has helped me through all the stages of research and writing. Without their consistent and illuminating instruction, this research work could not have reached its present form.

I am deeply grateful to Dr. T. Y. Ji, Dr. M. S. Li, L. L. Zhang and Dr. Y. Z. Li for all the help and valuable discussions on the cooperative work. I also owe my sincere gratitude to all of my friends in the Electrical Engineering and Electronics Department, especially Mr. L. Yan and Miss. Z. W. Zhang, who gave me their support and time on my studies. Many thanks also go to all the members in the Department of Electrical Engineering and Electronics at the University of Liverpool, for providing the research facilities that made it possible for me to conduct this research. Last but not least, I am greatly indebted to my beloved parents, for their loving considerations and great confidence in me through these years.

Abstract

This thesis is concerned with the development of Mathematical morphology (MM)-based algorithms and their applications to signal processing in power systems, including typical power quality disturbances such as low frequency oscillations (LFO) and harmonics. Traditional morphological operators are extended to advanced ones in the thesis, including multi-resolution morphological gradient (MMG) algorithms, envelope extraction morphological filters (MF), LFO extraction MF and convolved morphological filters (CMF). These advanced morphological operators are applied to the detection and classification of power disturbances, detection of continuous and damped LFO, and the detection and removal of harmonics in power systems.

Inspired by the robustness of Morphological gradient (MG) on edge detection in image processing, an improved MMG algorithm, which uses trapezoid structuring elements (SE), is applied for the identification of typical power quality disturbances. Also, the closing morphological operator, which can detect changes in the envelopes of signals, is applied in combination with MMG for the classification of the detected power quality disturbances. A variety of power quality disturbances have been simulated to evaluate the reliability of this hybrid approach and the effect of noise has been taken into consideration during the simulation studies. When applied to power system signals, MMG is capable of extracting the features of typical power disturbances and detecting their location and duration. Moreover, with the characteristics extracted by MMG, signal envelopes obtained by the *closing* operator can be another criterion for the classification of these power quality disturbances.

A hybrid scheme based on MF and a group search optimiser (GSO) is pro-

posed for detecting continuous LFO in power systems. The proposed envelope extraction MF focuses on accurately extracting the upper and lower envelopes of the target signals using basic morphological operators, $dilation - closing$ and $erosion - opening$, respectively. GSO is then applied to the extracted envelopes in order to obtain the feature values of the LFO components and reconstruct them. In addition to this hybrid method, another pre-designed MF is generated to deal with damped LFO components, which are generally caused by sudden faults occurring in the transmission line or inter-area in large-scale power systems. In this LFO extraction MF, the morphological operators, $opening - closing$ and $closing - opening$, are applied. For analysing these approaches, a generator fault system model and a four-machine two-area power system model were simulated to generate signals containing different types of LFO components. Several simulation tests have been undertaken to assess the efficiency of these proposed methods. The simulation studies show the robustness of each proposed approach in detecting continuous and damped LFO components, respectively.

In order to strengthen the filtering and detection ability of the basic MF, a new filter, the convolved morphological filter (CMF), is introduced for detecting and eliminating power system harmonics. This approach, which is based on MM and convolution, first uses a morphological transform as a low-pass filter and convolves the output signal of the MF with a pre-designed impulse response function. Using only Dirac delta function in the CMF, a variety of tests, by applying other different impulse response functions, have been simulated and the results of the CMF with different impulse response functions have also been compared for an analysis on their performance. When applied to power systems, the outcomes of the simulation studies demonstrate that the CMF has the ability to detect and remove harmonics even in noisy environments. Furthermore, another optimisation algorithm, the particle swarm optimiser (PSO) is also utilised for optimising the SE in order to improve the performance of MF in the detection and reduction of power system harmonics.

Contents

List of Figures

List of Tables

List of Symbols and Abbreviations

Symbols

$\leq$	Less than or equal to
$\in$	Element of
$\notin$	Not an element of
$\subseteq$	Contained in or equals
$\forall$	Universal quantifier
$<$	Less than
$\vee$	Infimum
$\wedge$	Supremum
$\varnothing$	Empty set
$\bigcup$	Union set
$\bigcap$	Intersection set
$\overset{M}{\oplus}$	Minkowski addition
$\overset{M}{\ominus}$	Minkowsi subtraction
$\oplus$	Dilation
$\ominus$	Erosion
$\circ$	Opening
$\bullet$	Closing

$\check{A}$	Reflection of A
$(A)_x$	Translation of A by x
A^c	Complement of A
I	Universal set
$U(f)$	Umbra of function f
$\mathbb{Z}^d$	The d-dimensional product of discrete integers
ψ	A morphological filter

Abbreviations

CMF	Convolved Morphological Filter
CT	Current Transformers
DC	Direct Current
DFT	Discrete Fourier Transform
DIP	Delft Image Processor
EHV	Extra High Voltage
EMD	Empirical Mode Decomposition
FFT	Fast Fourier Transform
FIR	Finite Impulse Response
FT	Fourier Transform
GSO	Group Search Optimiser
HHT	Hilbert-Huang Transform
IDFT	Inverse Discrete Fourier Transform
IIR	Infinite Impulse Response
LFO	Low Frequency Oscillation
MAPE	Mean Average Percentage Error
MF	Morphological Filter
MG	Morphological Gradient
MM	Mathematical Morphology
MMG	Multi-resolution Morphological Gradient
MNF	Methods of Normal Forms
MT	Morphological Transform
NERC	North American Reliability Council
PSO	Particle Swarm Optimiser
SE	Structuring Element
SNR	Signal-to-Noise Ratio
WGN	White Gaussian Noise
WT	Wavelet Transform

Chapter 1

Introduction

This chapter introduces the history and basic concepts of Mathematical Morphology (MM) algorithms, explains the development and background of image/signal processing using MM, highlights the relevant applications to this research and summarises the objectives and contributions of this research work. The structure of the thesis and an auto-bibliography are given at the end of this chapter.

1.1 Background of Mathematical Morphology

1.1.1 Developing History

MM was initially developed in 1964 by the cooperative work of two French researchers, Matheron and Serra, who worked on problems in petrography and mineralogy at the Paris School of Mines in Fontainebleau [1]. Their original idea was to quantify mineral characteristics from thin cross sections, which led to this novel practical method as well as theoretical advancements in integral geometry and topology [2]. In 1975, a seminal book entitled *Random Sets and Integral Geometry* was published, which was considered to have laid down the foundations of MM. Almost at the same time, permeability for porous media related to their geometry on a more theoretical level was studied by Matheron [3]. In 1982, Serra published a book titled *Image analysis and mathematical*

morphology, which was the first specific publication on MM.

In the years following the advent of MM, research concentrated on binary images, regarded as sets and proposed large numbers of binary operators, such as dilation, erosion, opening, closing, hit-or-miss transform, skeletonisation, *etc* [4]. During this period, MM developed dramatically on the theoretical level. From the 1970s to the 1980s, MM was expanded to grayscale functions and images. Other than generalising the major concepts to functions, new morphological operators, such as morphological gradient, top-hat transform and the Watershed transform, were introduced and expanded their applications. In the 1980s, MM research centres were established in several countries and more attention was paid to investigate their approach. Since then, MM had begun to deal with large numbers of imaging problems and applications. In 1986, Serra extended MM to the mathematical framework of complete lattices, which was considered as the most important development of MM during that time. This progress enabled MM to be more flexible and to be applied to a much larger number of structures. During the same period, the theory for morphological filtering was formulated, according to the lattice framework [5]. Several real-time applications of morphological filtering, such as the Delft image processor (DIP), were also proposed. In the 1990s, the development of MM concentrated on expanding its applied areas, including medical imaging, texture and scene analysis, robot vision, visual inspection, *etc*. The combination of theoretical work on the concept of connection and the connected filters had made MM achieve extraordinary performance in segmentation [6, 7]. The slope transform was generated by using morphological operators combined with eigenfunctions and their relative transfer functions. Additionally, soft morphology, a comparatively new method of MM, was presented by Koskinen [8]. In [9, 10, 11], the latest trends in soft morphology containing the algorithms and implementations were also included. Besides these extensions of MM, fuzzy morphologies attempted to apply fuzzy set theory to MM [12, 13, 14]. Furthermore, MM were combined with other approaches to extend its potential in various applications [15, 16, 17, 18, 19]. Through these developments, MM has become a

robustness and significant technique for geometrical shape analysis.

Digital image analysis was the main research area of MM during the past decades. The growth in both techniques and applications has been improved greatly and they are always closely interconnected. Mature and comprehensive approaches have been generated, such as image segmentation and classification, image filtering, image measurements, texture analysis and synthesis, pattern recognition, *etc.* As for the applications of MM in image processing, it comprises materials science, life science, geoscience, optical character recognition and document processing, visual inspection and quality control, *etc.* Two milestone monographs written by Serra [1] and Soille [20] have presented an overview of the development of MM in image processing.

MM has been widely developed and applied in the field of image processing. However, its potential has not been fully explored for applications in signal processing. In this area, MM focuses on the signal waveforms in the time domain directly, while most conventional approaches emphasising on the response of frequency domain, such as the Fourier Transform (FT) and the Wavelet Transform (WT).

The essential foundation of morphological transform is to process signals by a function, known as the structuring element (SE) or the structuring function in general. A SE slides through the target signal as a moving window, interacts with the signal, and detects specific features in the neighbourhood of every point in the target signal. A morphological filter (MF) is constructed from different combinations of basic morphological operators, which can preserve or suppress the characteristic defined by the SE and obtain a signal with the required features. When processing a signal with complex shapes, MF is able to decompose a signal into certain segments with a unique purpose and the main shape features of the target signal are preserved [21, 22]. As a consequence, for a transient signal, which contains a series of sudden changes superimposed on the fundamental waveform, MM has the capability to identify, recognise and enhance the specific features. In addition, the mathematical calculations involved in MM include only addition, subtraction, maximum, and minimum

operations without any multiplication or division, which leads to faster calculation speeds compared to traditional integral transform-based techniques. With these advantages, a new generation of algorithms based on MM is developed and applied in the field of signal processing. Furthermore, with its breakthrough in signal processing, it has also been applied to deal with power quality issues and improve the stability of power systems in the recent years.

In contrast to linear signal processing methods, MM concentrates on the shape of a signal waveform in the time domain rather than the frequency domain. When applied to detect and extract certain waveform components, MM has the following advantages over the integral transform-based approaches:

1. It can be applied to both periodic and non-periodic transient signals.
2. The morphological operators include only simple calculations without using any multiplication or division operations, which reduces computational complexity and increases the computing speed.
3. The window length using MM in real-time signal processing is relatively small, as it does not require the information of the full signal components.
4. MM can accurately and efficiently detect and extract the signal components without any distortion.

1.1.2 Foundations

Having been developed for several decades, MM has become a powerful tool for signal and image processing, especially for geometrical shape analysis. Considering its mathematical background, MM is defined on a complete lattice. Before giving the definition of a complete lattice, the concept of a partially ordered set should be introduced, which is also called a poset.

A partially ordered set is a set in which a binary relation '$\leq$' is defined for certain pairs of elements. The binary relation '$\leq$' over a set S satisfies the following conditions for all elements $x, y, z \in S$:

1. *Reflexive:* $\forall x, x \leq x$.

2. *Antisymmetry:* If $x \leq y$ and $y \leq x$, then $x = y$.

3. *Transitivity:* If $x \leq y$ and $y \leq z$, then $x \leq z$.

Given two partially ordered sets A and B and arbitrary elements a and x, the following definitions can be developed:

1. *Translation:* The translation of A by x, denoted by $(A)_x$, is defined as $(A)_x = \{a + x | a \in A\}$.

2. *Reflection:* The reflection of A, denoted by $\check{A}$, is defined as $\check{A} = \{-a | a \in A\}$. Reflection is also called transposition.

3. *Complement:* The complement of A, denoted by A^c, is defined as $A^c = \{x | x \notin A\}$.

4. *Difference:* The difference between two sets A and B, denoted by $A-B$, is defined as $A-B = \{x | x \in A, x \notin B\} = A \bigcap B^c$. Based on this operation, the complement of set A can also be defined as $A^c = \{x | x \in I-A\}$, where I is the universal set.

The partially ordered set formalises the intuitive concept of an ordering relation, which plays a key role in MM [20]. Besides partial ordering, there also exists a total ordering relation. A totally ordered set has a strengthened relation of '$<$': for any two elements x and y, exactly one of $x < y, x = y, x > y$ is true. The property of transitivity on a totally ordered set becomes $x < y$ and $y < z$ implies $x < z$.

A poset, $(S, \leq)$, is a lattice if any two elements of it, x and y, have a greatest lower bound (*i.e.* infimum), $x \wedge y$, and a least upper bound (*i.e.* supremum), $x \vee y$. A lattice, J, is a complete lattice if each of its subsets has an infimum and a supremum in J. A complete lattice satisfies the following properties: for subsets X, Y and Z,

1. *Commutativity:* $X \vee Y = Y \vee X, X \wedge Y = Y \wedge X$.

2. *Associativity:* $(X \vee Y) \vee Z = X \vee (Y \vee Z), (X \wedge Y) \wedge Z = X \wedge (Y \wedge Z)$.

1.2 Applications in Image Processing

Image processing and analysis using computer started in the 1960s. Since then, the range of applications of image analysis techniques has generalised to almost all engineering and scientific fields: visual inspection, document imaging, geoscience and remote sensing, biology and medical imaging, identification and security control, image coding, *etc* [20]. The various application fields have resulted in numerous image analysis problems, which in turn promotes the development of image data analysis approaches. In this research area, MM has tackled a series of problems and demonstrated its usefulness for solving practical image analysis issues.

Image analysis tasks which can be dealt with by MM include three main aspects: image filtering, image segmentation and image measurements. In image filtering, an image filter is defined as a neighbourhood operator, which considers neighbourhood values when processing an image point [20, 23]. MM in image filtering has been applied for noise reduction, edge enhancement and extraction or suppression of selected image structures. Furthermore, most MF are designed using some knowledge about the shape and geometrical properties of image objects [24, 25, 26].

Image segmentation is the decomposition of an image into different regions, where each region has certain properties. Once the image is segmented, measurements can be performed separately and neighbouring relationships can be investigated. Hence, image segmentation is an important procedure in the quantitative interpretation of image data [27, 28]. MM in image segmentation has made some achievements in delineating the boundary of objects in gray-tone images and separating connected objects in binary images [29].

Image measurements focus on characterising the objects of an image by several numerical values. In this sense, MM in image measurements can be applied for computing numerical values of the whole image in order to characterise the texture, fragmentation, shape, orientation and size of the image structures [30]. Once these measurement values are obtained, the classification can be performed for further analysis. Besides these three major tasks, MM is

also applicable to some other tasks, such as the interpolation of contour data, minimal path detection, unwrapping of noisy phase maps, *etc.* To sum up, after several decades of development, MM has become a powerful image analysis tool and is applied to a variety of applications in image processing.

1.3 Applications in Signal Processing in Power Systems

Signal processing is a technology that contains the fundamental theory, applications, algorithms and implementations of processing information. The application fields of signal processing vary and numerous methods have been applied in signal processing [31]. The installation of sophisticated devices and equipment in power systems has caused various disturbances, which also leads to the increasing necessity of signal processing methods in power systems. Furthermore, the performance of the traditional linear approaches in signal processing is limited to some extent. Therefore, non-linear techniques attract more attention in this particular area, which has motivated MM to be applied. In power systems, MM has already been developed and utilised to a variety of aspects, such as removing DC offset, detection and compensation for current transformer (CT) saturation and extra-high-voltage (EHV) transmission line protection.

A decaying DC offset often occurs following a fault and contaminates the phasor measurement which is an essential component of protection relays. With the deterioration by the decaying DC offset, the process of phasor measurement performed using FT is affected and a series of decaying oscillations is generated. In removing the DC offset and the relative noise existing in power system signals, filters based on MM have been applied and it has been proved that these proposed methods were effective and high-speed-calculation approaches in dealing with this noise and the requirements for real-time analysis has also been met [32, 33, 34]. In electrical power systems, CT have been widely applied for measurement and protection purposes. However, the CT saturation prob-

lem results in distorted secondary currents with a corresponding measurement error and protection relay mal-operation may be induced. Therefore, the detection and compensation for CT saturation are of great importance in power systems. Several MM-based schemes have been developed to detect and reconstruct healthy secondary currents and related simulation cases demonstrated their robust performance in [35, 36, 37]. With the growing development of EHV transmission lines in power systems, the protection of them becomes more essential and important considering the reliability and stability of power systems. In [38, 39], approaches using MM were proposed to extract transient features from voltage and current signals along transmission lines during a post-fault period and the simulation results demonstrated that these algorithms provided accurate responses under a variety of fault conditions compared to conventional approaches.

Besides the power system issues mentioned above, other types of disturbances of power systems have also attracted attention since the stability of power systems has been one of the main concerns for the operation of utilities and manufacturing industries. This research concentrates on the application of MM to solve these problems.

Before introducing power quality disturbance, electrical power quality should be clearly defined. Firstly, there is no acknowledged definition of electrical power quality since different people have diverse views on it. Moreover, the perceptions of power quality at transmission level and that at distribution level are also different [40]. Generally, power quality indicates the features of supply voltage affecting the load performance. The most usual definition of power quality is the ability of a power system to operate loads without disturbing or damaging them and it is a description of the successful utilisation of the system voltages from the distribution system without any interference or interruption [41]. From a broader point of view, good power quality can be summarised as services with good quality; a reliable system with a steady supply voltage that stays within the prescribed range, steady alternating current frequency close to the related value, and smooth voltage curve waveforms; an excellent

system design with less construction errors, grounding errors, *etc.* While in a narrow sense, power quality concentrates on a waveform distortion assessment, seeking ways to reduce the negative effects from distorted waveforms. Hence, according to both senses, power quality standards, which help to resolve problems and prevent social and economical losses concerned with power quality disturbances, have been established. Furthermore, the characteristics of different power quality issues are also defined.

In general, anything that leads to the power system voltage or current deviating from its ideal sinusoidal waveform could be considered as a power quality disturbance [42, 43]. Referring to the IEEE 1159 standard [44], which is a well-established power quality standard, a given power quality disturbance is normally classified into two categories: steady-state disturbances and temporary disturbances. The power quality disturbances concerned in this research are described and classified in the following paragraphs.

Steady-state disturbances are of long duration and vary little with time, including waveform distortions resulted from harmonics, noise and power frequency variations. While, temporary disturbances usually appear in a steady-state and when the disturbance disappears, the power system returns to normal or to a new steady-state. These are further divided into several different types containing long duration voltage variation, lasting longer than one minute, short duration voltage variation, lasting longer than half a cycle of the power frequency but less than or equal to one minute, and transient, lasting shorter than 50 ms, *etc.*

- **Transient** A transient is an undesirable momentary deviation of the supply voltage or load current. Transients can be broadly categorised into two types - impulsive and oscillatory. In this thesis, the oscillatory transient is analysed.

  - *Oscillatory transient*: An oscillatory transient consists of a voltage or current whose instantaneous value changes polarity rapidly, *i.e.* it includes both positive or negative polarity values.

- **Short duration variation** Short duration variations are almost always caused by fault conditions, the energisation of large loads that require high starting current, or intermittent loose connection in power wiring. According to the fault location and the system condition, the fault can lead to either temporary voltage drops (sags) or voltage rises (swells), or a complete loss of voltage (interruptions).

  - *Voltage sag:* A voltage sag is a significant voltage reduction for a relatively short duration. It may be caused by system faults, increased load demand and transitional events such as starting large electrical motors. Numerous process disruptions can be caused by voltage sags.
  - *Voltage swell:* A voltage swell is a short term increase of the system voltage. Such an event is often caused by an abrupt reduction in load or appears on the unfaulted phases of a three-phase circuit, where a single-phase short circuit has occurred. A swell may stress any delicate equipment components resulting in premature failure.
  - *Interruption:* A momentary loss of voltage on a power system can be called a momentary interruption. Such a disturbance describes a drop of 90-100% of the rated system voltage. It can be the consequence of power system failures, equipment malfunctions, and control faults. Interruptions may affect electronic and lighting equipment, such as power and electronic controllers and computers, and may lead to misoperation or shutdown of this equipment.

In addition to these typical power quality disturbances introduced above, another two types of disturbances in power systems, which lead to waveform distortion have also been investigated in this research. Waveform distortion is a steady-state deviation from an ideal sine wave of power frequency principally characterised by the spectral content of the deviation.

- *Harmonics:* Harmonics are sinusoidal voltages or currents having frequencies that are integer multiples of the fundamental frequency (the

frequency at which the supply system is designed to operate). Harmonics distortion exists due to the non-linear characteristics of devices and loads on the power system.

- *Low frequency oscillations:* LFO is a signal which is usually below 20 Hz and creates a rhythmic pulse or sweep. In power systems, LFO vary in the range of 0.1 to 2.0 Hz and exist due to the imbalance between power demand and available power at a period of time. Due to different faults occurring in large-scale power systems, continuous and damped LFO can be generated.

According to these problems stated above, the advanced morphological operators presented in this project are mainly applied to deal with three types of disturbances in power systems: detection and classification of typical power quality disturbances, detection of LFO components in power systems and detection and removal of power system harmonics. In the following, background research for each particular objective stated above and relevant work reported in recent literature are introduced, and the corresponding methods proposed in this project to achieve these targets are also presented.

1.3.1 Power Quality Disturbances

Power systems suffer from disturbances of the change of rated voltage (or current). These disturbances are very common and may lead to malfunction of electrical devices, including power supplies, measuring and control equipment, interfacing with communication signals, and voltage stability due to a reduction of the bus voltage for a short duration[45]. In [46, 47, 48], several studies, according to the North American Electric Reliability Corporation (NERC), power disturbances were carried out to investigate the monitoring and control of disturbances. Furthermore, the data also showed that large blackouts were taking place with an increasing frequency in North American [49], which indicates that it is important to deal with power disturbances. Research considering the monitoring and comprehensive analyses of typical power quality

disturbances has been included in [50].

A variety of methods have been applied for monitoring power disturbances in power systems. The discrete Fourier transform (DFT) has been a popular tool in the monitoring of power disturbances. The DFT was successful in dealing with periodic signals. However, it was not efficient in tracking a transient signal due to the limitation of a fixed window width [51]. The Wavelet Transform (WT) was then introduced to overcome this limitation. Different from the DFT, the WT used different windows for different frequencies [52]. Therefore, the WT was more capable of identifying the details of localised transients than the DFT. Nevertheless, this technique increased the computation burden and therefore reduced its attractiveness [51].

As previously introduced previously, MM, based on set theory, was established by introducing fundamental operators applied to two sets [53]. In contrast to the DFT and WT, MM is concerned with the shape of a signal waveform in the time domain. Based on the morphological gradient (MG), which can detect sudden changes of waveforms, a multi-resolution morphological gradient (MMG) has been developed for the detection of power quality disturbances. A variety of typical power quality disturbances have been simulated to evaluate the performance of the MM-based technique in previous research using this method [51, 54, 55]. However, in these studies, the accuracy of the estimation could not be guaranteed due to interference by noise. Furthermore, the criteria in these algorithms were complicated and difficult to implement and some of them did not provide methods to classify the detected disturbances. In order to overcome these limitations, the previous MM-based method has been improved in this research, by changing the shape and length of the SE and it has been applied to signals with these common power quality disturbances to extract meaningful components from the target signals for identification and classification. Furthermore, a simple and novel approach using the *closing* morphological operator has been provided to classify the detected power quality disturbances.

1.3.2 Low Frequency Oscillations

In a power system, LFO is a phenomenon where oscillations occur for long periods of time, which can threaten the stability of the system. The dominant oscillation modes typically vary in the range of 0.1 to 2.0 Hz and create a rhythmic pulse or sweep [62]. Referring to the scope and magnitude of LFO, the modes of LFO can be classified into two categories: local modes having a range of 1.0 to 2.0 Hz and inter-area modes having a frequency range of 0.1 to 1.0 Hz.

With the deregulation of electric power industries, the interconnection of individual islands to bulk power systems, over long distances has become the major characteristic of smart transmission systems around the world [56, 57]. Generally, interconnected transmission systems have great advantages in decreasing reserve capacities, reducing the gap between load peaks and valleys, and enhancing the reliability of electric power systems [56]. However, conflicts between large transfer capacity and weak interconnections can lead to LFO, which degrades the stability of power systems and also affects the power quality [56, 58, 59]. Therefore, due to the importance of dynamic stability and long-distance-transmission capability, the effective and accurate detection of LFO components for further analysis is necessary in large-scale power systems. Furthermore, some of power system blackouts incidents related to LFO and lesson learned were summarised in [60, 61]. According to these studies, incidents due to LFO happened almost all around the world in recent years. Additionally, LFO components in the frequency range of 0.1 to 0.7 Hz were considered as the most serious ones and could lead to wide spread blackouts. In preventing the advent of severe blackouts, actions must be taken to detect and eliminate LFO in power system signals.

The essential cause of electrical power LFO is the imbalance between power demand and available power at a period of time. Mechanical oscillation of the rotor phase angle with respect to a rotating frame can lead to a continuous LFO phenomenon. Besides this, faults triggered by disturbances on the transmission line, components failure and faults in the transmission line can result

in the presence of damped LFO components [63]. The existence of LFO could lead to unstable security operationsand this has occurred more frequently in recent years. Nowadays, various approaches have been developed for the purpose of monitoring and controlling LFO components. As discussed in [64, 65, 66], these methods can be categorised into two main classifications: 1)modal analysis, 2)measurement-based analysis. Eigenanalysis, which applies a linearised time-invariant model, is one of the most effective tools in modal analysis to evaluate modal information [67, 68, 69]. However, the precision of dynamic models and the parameters of system components affected the validation of the analysis results. Due to the computational complexity the computation speed slowed down when full-state eigenvalue analysis was applied. As a consequence, the scope of the analysis was constrained to a certain region [70, 71]. Over recent years, methods of normal forms (MNF) has been applied to eigenanalysis providing a novel method for dealing with non-linear behaviours [72]. Notwithstanding, both linearisation-based eigenanalysis and MNF-based eigenanalysis suffered from complex computations which are difficult to implement in large- scale power systems [73].

To date, several analysis techniques based on measured signals have been developed to evaluate the oscillatory parameters of LFO components and the corresponding mode shapes. Previous comparisons, between some of the existing techniques reported in [74, 75, 76], indicated that measurement-based analysis such as FT, Hilbert-Huang transform (HHT) and the Prony analysis were easier to apply and had been widely employed. Among these, FT-based analysis tools have been used for offline studies of power system dynamics and are easier to implement [65, 77]. However, this technique relies on the assumption of linearity and it being strictly periodic or stationary in time. Non-linear and non-stationary data can be processed and analysed using approaches based on HHT [78, 79]. Empirical mode decomposition (EMD), which is the core of HHT procedure, breaks down a signal into a series of intrinsic mode functions both in amplitude and frequency [80]. However, the competence of this method to measure modal parameters and to distinguish temporal changes was limited

when applied to signals which contain multiple modal components [75]. Prony analysis has been applied online to obtain oscillation frequencies and damping ratios. However, to obtain the complete system characteristics in a large- scale system, single signal analysis alone is not sufficient [57, 81, 82]. [57, 81, 82]. Therefore, a multi-signal Prony algorithm was introduced in [83] and since this method could identify the inter-area modes and the local modes at the same time, the accuracy of the multi-signal based Prony algorithm was higher and the computational cost was lower compared to the traditional algorithms.

In recent years, WT, consisting of an alternative mathematical technique to process LFO, has been applied to the monitoring of power system oscillatory performance [59, 84, 85]. However, further research is required to develop the WT concept in order to properly estimate the features of typical LFO components. Although several improvements have been made on the previously introduced methods for a more precise estimation of LFO parameters, large quantities of computations are required leading to an increase in complexity and greater memory usage. Additionally, some of these approaches are difficult to implement in real situations. Furthermore, these methods do not provide a direct and apparent way to detect and monitor the existence of LFO for control consideration.

As LFO components in signals cause a slight change in their envelopes, this implies that the signal envelopes contain information on the LFO components. Moreover, MM-based methods are capable of detecting these tiny variations in signal waveforms. Therefore, the application of MM-based approaches in detecting LFO components is inspired by these characteristics. Firstly, a hybrid approach based on MF and group search optimiser (GSO) to detect continuous LFO components is developed in this thesis. The proposed MF focuses on accurately extracting the upper and lower envelopes of the target signal using basic morphological operators, $dilation - closing$ and $erosion - opening$, respectively. Hence, the MF is regarded as the envelope extraction MF. GSO introduced in [86] is then applied to the extracted envelopes in order to estimate the parameters of the LFO component and reconstruct it.

This combinational technique is robust for the online detection of continuous LFO components, mainly resulted from the imperfections of the generators caused by slight vibrations and impacts in the generators, for providing the parameters for further analysis. Similar to conventional methods in dealing with LFO, the MF with GSO algorithm can obtain the feature values of LFO and reconstruct them, however it cannot directly extract LFO with simple calculations and more computational time is required when applying GSO in more sophisticated circumstances. Hence, as for detecting damped LFO components, which are generally caused by sudden faults happened in transmission line or inter-area in large-scale power systems, another MF is designed from a new approach. In this LFO extraction MF, another two morphological operators, $opening - closing$ and $closing - opening$, are applied in order to directly extract the LFO.

In the simulation studies, a generator fault test system model and a four-machine two area test system were built to generate input signals containing continuous and damped LFO components respectively. The proposed method of MF with GSO and the LFO extraction MF are then applied to detect these two types of LFO components in the input signals, separately. Simulation results have shown that these proposed methods provide effective, steady and simple ways for detecting continuous and damped LFO components, respectively.

1.3.3 Power System Harmonics

In electrical power networks, power system harmonics result in power quality problems within a wide range of power electronics-related applications [87, 88]. Furthermore, with the development of semiconductor devices since the 1960s, power electronics technologies have been widely applied to various equipment, such as lighting, variable speed monitor drives, and uninterruptible power supply systems [89]. Due to their non-linear nature, most power electronics equipment cause non-sinusoidal currents, which lead to severe harmonic contamination, also known as harmonic pollution in distribution grids [90, 91].

Harmonic pollution has serious hazards on electrical equipment, such as reducing transmission capacity, increasing the loss of transmission cables, limiting overload capacity, efficiency, lifetime, and even damaging the equipment [92]. As a consequence, it is essential and timely to develop an effective method to detect and reduce harmonics in power systems.

Generally, digital low pass filters, which are designed based on either infinite impulse response (IIR) or finite impulse response (FIR), have been applied to the elimination of power system harmonics. However, a feedback loop is required for the IIR filter to calculate the output value and the performance of the filter can be easily degraded because of rounding errors in the computation [93]. Different from the IIR filter, the FIR filter does not have a feedback loop, but a high order is required for achieving high accuracy due to its poor roll-off feature [88]. Even though high accuracy can be guaranteed, the computation burden increases and the performance of the filter is easily affected by a noisy environment. Recently, several other techniques have been applied in estimating the parameters of power system harmonics for further analysis and control. The performance of the DFT-based algorithm in estimating the parameters of harmonics is not always stable and accurate due to undesirable conditions, for example the leakage effects of system frequency variation on the measurements [94]. The Kalman filter approach, which has been proved to be simple, linear and robust, requires knowledge of the statistics of the target signal in advance and the state matrix needs to be accurately defined [95, 96]. Besides these, several optimisation algorithms have also been proposed in the field and some achievements have been made [97, 98, 99]. While similarly, the efficiency and accuracy of the optimisation process in estimating parameters of harmonics are also degraded to some extent. According to this research, a simplex linear filtering method may not be sufficient in practical situations.

Based on MM, MF have been applied in heart beat detection and removing noise in vibration signals and have obtained good results. In mathematics, and in particular, functional analysis, convolution is a traditional mathematical operation on two functions, producing an integral function that is regarded

as the amount of overlap of one function as it is shifted over another function. It has been applied to probability, statistics, computer vision, image and signal processing, electrical engineering, and differential equations [100]. In [101], the idea to combine the convolution method, which was viewed as a linear filtering technique, with MF in order to take advantage of both approaches was proposed. In the whole process, the output signal filtered by MF was convolved with a proper pre-designed impulse response function. This was regarded as the convolved morphological filter (CMF). CMF used morphological operators and convolution with chosen impulse responses to obtain highly accurate characteristics of high, low and band-pass filtering techniques. However, in [101], the impulse response function only applied the Dirac Delta function in the convolution process and the performance of the CMF was not good enough because of the large amplitude increase after CMF filtering. It is also known that the impulse response function utilised in the convolution process has a great impact on the performance of the convolution. Additionally, different shapes and lengths of the SE in MF can also lead to different filtering results. Hence, inspired by the work of [101], the performance of CMF using other impulse response functions on detecting and removing harmonics are investigated and compared in this thesis. Moreover, besides estimating the performance of CMF, simulations on optimising SE in MF by applying a particle swarm optimiser (PSO) has also been undertaken in order to improve the performance of MF.

In order to identify power quality disturbances, LFO and power system harmonics, algorithms based on MM have been developed. The motivation and objectives are illustrated in the following section.

1.4 Motivation and Objectives

MM has been regarded as a robustness tool for image and signal processing. During several decades of development, MM has concentrated its major work on the image processing field. However, MM has its potential in dealing with complicated signal processing. Due to the developments of modern techniques

and equipment in power systems, the identification of the target signals become more complex. Conventional methods, especially linear techniques and classic MM, cannot meet the higher requirements, including higher accuracy, more computational complexity, faster speed, *etc*, and they also limit the development of signal processing. As a consequence, it is necessary to improve the morphological operators in order to deal with the complex signal processing in power systems.

Numerous traditional techniques, such as FT and WT, which are frequency-based transformations, have been applied for signal processing in power systems. However, the application of MM in signal processing in power systems is insufficient. MM has its potential in extracting small features from complex signals and it mainly focuses on the signal waveforms in the time domain directly. Hence, it is necessary to compare to compare the MM-based techniques with the traditional ones in order to find out the relationship between them, or even combining and reforming them into new methods. Furthermore, these extracted characteristics are important and can be applied for further analysis. Additionally, power quality issues have become one of the major concerns for the operation of utilities and manufacturing industries in power systems in the recent years. Therefore, it is appropriate to investigate the performance of morphological operators for signal processing in power systems, specifically for the detection of different disturbances since MM has extraordinary performance in extracting and detecting small features. Although conventional methods have been applied in this field for a long time, MM-based approaches still have the ability to achieve better performance.

Advanced morphological operators have been applied to the following three applications in this thesis: detection and classification of typical power quality disturbances, detection of LFO components, and the detection and removal of power system harmonics. Power quality disturbances can be typically described as any variation in electrical power services, such as voltage sags, momentary interruptions, voltage swells and oscillatory transients. These disturbances are very common and have led to some power quality issues. They mainly result in

the malfunction of electrical devices, power supply and measuring and control equipment, interfacing with communication signals, and voltage stability due to the reduction of the bus voltage for short durations. As a consequence, it is essential to deal with these issues to prevent the advent of more severe problems in power systems.

The power quality issue has become a main problem for electricity consumers. The increasing use of load equipment increases the number of disturbances in the power system. Power quality problems in power systems, including the three issues mentioned above, degrade the performance and efficiency of customers' loads and are of increasing concern to utilities and industry. Furthermore, because of the high possibility of the occurrence of wide spread blackouts due to these events, they may also result in inconvenience to life and high costs. Consequently, solving these problems is of high importance and the outcomes of the research can improve the performance and stability of large power systems which will also benefit daily life.

1.5 Contributions of this Research

The major contributions of this research include the fundamental study of mathematical morphology, development of advanced morphological operators according to the basic ones, and their applications to the detection of different types of disturbances in power systems, in particular for the detection and classification of typical power quality disturbances, detection of LFO, and the detection and removal of power system harmonics. The contributions concentrate on the following topics:

- The thesis starts by studying the history and mathematical background of MM and analysing the properties of the basic morphological operators. The applications of MM in both image processing and signal processing in power systems during recent years have also been studied.
- Advanced morphological operators are developed through the study of

a set of morphological operators applied to different applications of signal processing in power systems, specifically for the detection of different types of disturbances. For accomplishing these certain tasks, some hybrid approaches have been proposed by combining these advanced morphological operators with other signal processing methods.

- An improved MM-based approach is constructed for the detection and classification of typical power quality disturbances in power systems. The characteristics of different power quality disturbances can be extracted by a morphological operation, MMG, with pre-defined trapezoid SEs. With the combination of the extracted feature and the envelope produced by another morphological operator, these disturbances are further classified.

- A hybrid scheme is developed to effectively online detect continuous LFO components, which result from the imperfections of generators in power systems. Firstly, an envelope extraction MF is proposed, focusing on accurately extracting the upper and lower envelopes of the target signals using morphological operators. Secondly, GSO is then applied to the extracted envelopes that contain information on the LFO components in order to obtain the features of them and reconstruct them. The hybrid approach is simulated in consideration of severely noisy environments, and satisfactory outcomes have been achieved. Another MF is also designed to detect damped LFO components caused by faults in interconnected area in large-scale power systems. This LFO extraction MF is able to directly extract changes in signal waveforms resulting from damped LFO components and it is not affected by the interference of noise and the quantisation process.

- CMF, which is the combination of MF and the convolution process, is introduced and improved to successfully and efficiently detect and remove power system harmonics. The target signal is firstly passed through the proposed MF and the corresponding output is then convolved with a pre-defined impulse response function. Several different impulse response

functions are applied in the CMF for comparisons of their performance. In addition to the refinement in CMF, PSO was also applied for the optimisation of the SE to improve the filtering results of the MF. With the optimised SE, the enhanced MF is also able to detect and remove harmonic components without delay and distortion.

1.6 Contents of the Thesis

This thesis is structured as follows.

Chapter 2 This chapter introduces the mathematical background of M-M. Starting with the basic morphological operators, dilation and erosion, in a binary scenario, it then extends them for grey scale applications. Afterwards, the two basic operators are combined and evolved to a set of basic sequential operators, such as opening and closing. Other types of MM-based schemes are also included in this chapter, containing MMG, envelope extraction MF, LFO extraction MF and CMF, from which the advanced morphological operators proposed and applied in the following chapters are developed.

Chapter 3 In this chapter, a hybrid scheme based on MM is applied for the purpose of detection and classification of typical power quality disturbances. MMG is a non-linear morphological transform which presents the gradient information in the output. Another basic morphological operator is applied in combination with MMG for the classification of the types of the extracted disturbances. In the improved MMG algorithm, trapezoid SEs are selected and applied to achieve better performance in detecting the power quality disturbance occurring in a power system signal. Moreover, with the features extracted by MMG, the signal envelope, obtained by the basic morphological operator, *closing* operator, is regarded as another criteria for the classification of different power quality disturbances. The implementation of the method is firstly introduced

and the simulation results are explained later. A variety of power quality disturbances have been simulated to evaluate the performance of this collaborative method. Furthermore, noisy environments have been taken into consideration during simulations in order to verify the reliability of the proposed approach in practical situations.

Chapter 4 The use of envelope extraction MF combined with the GSO algorithm to online detect continuous LFO components that are caused by the imperfections of generators in power systems is proposed and introduced in this chapter. The envelope extraction MF is applied to extract the upper and lower envelopes of the target signal. Once the envelopes are extracted, the GSO technique is utilised to obtain the parameters of the LFO components, such as amplitude and frequency, and reconstructing the LFO components. Besides this, an LFO extraction MF is also generated from a new approach to directly detect and extract damped LFO components resulted from faults occurred in interconnected area of large-scale power systems. Note, this method cannot provide the parameters of the required LFO components. Two pre-built power system models are also generated to produce different types of LFO components for estimating the efficiency of the hybrid algorithm and the LFO extraction MF. The implementations of the MF with GSO and the LFO extraction MF are introduced in the first place and the corresponding simulation outcomes are then presented respectively. In the simulation studies, both the continuous and damped LFO components, are considered. Moreover, in the simulations for detecting damped LFO components, a quantisation influence analysis has been undertaken and it has shown that the performance of the proposed approach is not affected by the quantisation process, which means that this method can be easily applied in practical equipment. Furthermore, severely noisy environments were considered for both scenarios in the simulation studies.

Chapter 5 This chapter introduces a novel filter, CMF, for detecting and

eliminating power system harmonics. This approach firstly uses a morphological transform as a low-pass filter and the output of the MF is then convolved with a pre-designed impulse response function. Furthermore, CMF with different impulse response functions, including Dirac delta function, IIR function, FIR function and sinc function, are proposed and applied to evaluate and compare their performance. Additionally, the comparisons between the performances of CMF and MF are also undertaken and the outcomes of the simulation studies present the advantages of CMF in terms of accuracy and computational complexity to some extent. Additionally, CMF using FIR as the impulse response has also been used to extract not only the fundamental frequency component, but also other harmonic components, which can be applied for harmonic analysis. Similarly, noisy environments are also considered for simulating the performance of the proposed method in practical conditions. In addition to the simulations on CMF using different impulse response functions, PSO is applied for optimisation of SE to improve the performance of MF and better results have been achieved by using the optimised MF.

Chapter 6 In the final chapter, the thesis is concluded and suggestions for future work are presented.

1.7 Auto-bibliography

The publications produced from this research work are listed in this section as follows:

1. **J. Zhu**, T. Y. Ji, M. S. Li, Q. H. Wu and J. S. Smith, Detection and Classification of Power Disturbances Using Mathematical Morphology with Trapezoid Structuring Elements and Signal Envelopes, in Innovative Smart Grid Technologies Conference Europe, 2014 IEEE PES, Istanbul, 12-15 October 2014, pp. 1-6.

Chapter 2

Mathematical Morphology Algorithms and Their Applications

This chapter firstly illustrates the definitions and implementations of basic morphological operators and then introduces the advanced morphological operators which are used for the applications presented in the following chapters. A series of morphological operators, including dilation, erosion, opening and closing, are introduced starting with binary morphology based on set theory. Grey-scale morphology, regarded as the extension of binary morphology, is then proposed according to the set representations of functions.

2.1 Basic Morphological Operators

2.1.1 Definitions for Binary Operations

The essential function of mathematical morphology (MM) is to extract relevant structures of a set, which is normally the target image/signal. The extraction is usually processed by the interaction between the set and another set, which is known as the structuring element (SE). The shape and length of the SE are designed referring to the priori knowledge about the shape and other

properties of the target signal. Dilation and erosion are two basic morphological operators and form a pair of dual transforms. They are derived from Minkowski set theory: Minkowski addition and subtraction [102].

Minkowski Addition and Subtraction

Minkowski addition is a binary operation of two sets, A and B, in Euclidean space, named after Hermann Minkowski. It is denoted by $\overset{M}{\oplus}$ and is defined as the result of adding every element of A to every element of B:

$$A \overset{M}{\oplus} B = \{a + b | a \in A, b \in B\} = \bigcup_{b \in B} (A)_b. \tag{2.1.1}$$

$(A)_b$ is the translation A by the element in B, which is b, and $\bigcup (A)_b$ is the union set of the translation. It is assumed that $A \overset{M}{\oplus} \{0\} = A$ and $A \overset{M}{\oplus} \varnothing = \varnothing$. The dual operation of Minkowski addition is called Minkowski subtraction, denoted by $\overset{M}{\ominus}$, and given as:

$$A \overset{M}{\ominus} B = \bigcap_{b \in B} (A)_b. \tag{2.1.2}$$

$\bigcap (A)_b$ is the union set of the translation. The following relation is true for Minkowski subtraction:

$$A \overset{M}{\ominus} B = \{x | (\check{B})_x \subseteq A\} = (A^c \overset{M}{\oplus} B)^c \tag{2.1.3}$$

Proof:

$$\begin{aligned} \because z &\in \left(\bigcap_{b \in B} (A)_b \right) \\ \Rightarrow z &\in (A)_b \\ \Rightarrow z &\in \{a + b | a \in A, b \in B\} \\ \Rightarrow z &\in \{x | x - b \in A, b \in B\} \end{aligned}$$

$$\begin{aligned} \text{and} \quad \because \quad & \{x | (\check{B})_x \subseteq A\} = \{x | x - b \in A, b \in B\} \\ \therefore \quad & A \overset{M}{\ominus} B = \{x | (\check{B})_x \subseteq A\}. \end{aligned}$$

$$\begin{aligned}
\because A^c \overset{M}{\oplus} B &= \bigcup_{b\in B}(I-A)_b = I - \bigcap_{b\in B}(A)_b \\
&= \left(\bigcap_{b\in B}(A)_b\right)^c = \left(A \overset{M}{\ominus} B\right)^c \\
\therefore A \overset{M}{\ominus} B &= (A^c \overset{M}{\oplus} B)^c.
\end{aligned}$$

The proofs that Minkowski addition satisfies the properties of commutativity and associativity are presented below. Similar methods can be applied to prove that Minkowski subtraction also satisfies these properties.

1. *Commutativity:* $A \overset{M}{\oplus} B = B \overset{M}{\oplus} A$.

   Proof:

$$\begin{aligned}
A \overset{M}{\oplus} B &= \{x|x = a+b, a\in A, b\in B\} \\
&= \{x|x = b+a, b\in B, a\in A\} \\
&= B \overset{M}{\oplus} A.
\end{aligned}$$

2. *Associativity:* $(A \overset{M}{\oplus} B) \overset{M}{\oplus} C = A \overset{M}{\oplus} (B \overset{M}{\oplus} C)$.

   Proof:

$$\begin{aligned}
(A \overset{M}{\oplus} B) \overset{M}{\oplus} C &= \{a+(b+c)|a\in A, b+c\in B \overset{M}{\oplus} C\} \\
&= \{a+b+c|a\in A, b\in B, c\in C\} \\
&= \{(a+b)+c|a+b\in A \overset{M}{\oplus} B, c\in C\} \\
&= (A \overset{M}{\oplus} B) \overset{M}{\oplus} C.
\end{aligned}$$

Binary Dilation and Erosion

According to Minkowski addition, the definition of dilation is obtained. By replacing the operator $\overset{M}{\oplus}$ by $\oplus$ in (2.1.1) and utilising a reflected SE, $\check{B}$, the definition of dilation is obtained as:

$$A \oplus B = \bigcup_{b\in\check{B}}(A)_b = \bigcup_{b\in B}(A)_{-b} = \bigcup_{b\in B}\{x|x = a-b, a\in A\}. \tag{2.1.4}$$

Similarly, the definition of erosion is derived from Minkowski subtraction and also a reflected SE $\check{B}$ is applied. The definition of erosion is given as:

$$A \ominus B = \bigcap_{b \in \check{B}} (A)_b = \bigcap_{b \in B} (A)_{-b} = \bigcap_{b \in B} \{x | x = a - b, a \in A\}. \tag{2.1.5}$$

In a binary image, it has only two possible values for each pixel. Hence, a binary image can be described conveniently using the notion of a set. A binary image is usually regarded as a set I, while an object in it is considered as a subset $X \subseteq I$. Letting sets A and B represent two binary images according to the above definitions, the operations of dilation and erosion for binary image processing are obtained.

The two images A and B act differently in image processing. A is the image being processed, which can be considered as the target image, while B is regarded as an SE that slides as a probe across image A and interacts with each pixel of A. Generally, the size of B should be much smaller than that of A. In order to make the processes of dilation and erosion clearer, an example is illustrated in Fig. 2.1 and Fig. 2.2. Fig. 2.1 presents the binary image A to be processed and the SE B, where the origin of B is set at (0,0). Fig. 2.2 shows how the dilation and erosion function are processed between A and B. The red pixels indicate the dilated part after dilation and the blue pixels demonstrate the eroded part after erosion.

Furthermore, Fig. 2.2 also depicts an important property of dilation and erosion, duality, which means that applying dilation to A is equivalent to the complement of applying erosion to its complement A^c. The duality of dilation and erosion are given as:

$$A \oplus B = (A^c \ominus B)^c \tag{2.1.6}$$

$$A \ominus B = (A^c \oplus B)^c. \tag{2.1.7}$$

Proof:

$$\begin{aligned} A^c \ominus B &= \bigcap_{b \in \check{B}} (I - A)_b = \bigcap_{b \in B} (I - A)_{-b} \\ &= I - \bigcup_{b \in B} (A)_{-b} \end{aligned}$$

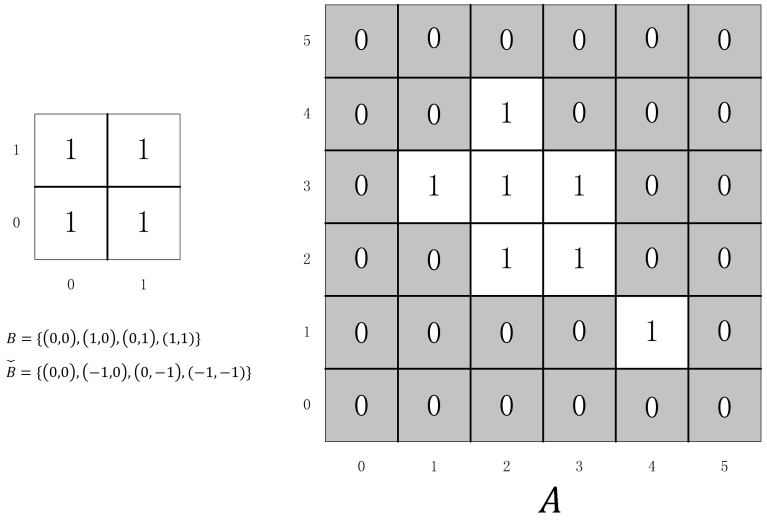

Figure 2.1: Original binary image and SE B

$$\begin{aligned} &= I - A \oplus B = (A \oplus B)^c \\ \Rightarrow A \oplus B &= (A^c \ominus B)^c. \end{aligned}$$

Similarly, Eqn. (2.1.7) can be proved. The property of duality indicates that the procedures of dilation and erosion are not reversible and there are no inverse transforms for these operators [22]. Applying dilation and erosion alternately actually generates a pair of new operations, which will be presented in the following sections.

Distributivity is another property of dilation and erosion and this is given as:

$$A \ominus B \ominus C = A \ominus (B \oplus C). \tag{2.1.8}$$

Proof:

$$\begin{aligned} A \ominus B \ominus C &= (A^c \oplus B)^c \ominus C \\ &= [(A^c \oplus B) \oplus C]^c \\ A \ominus (B \oplus C) &= [A^c \oplus (B \oplus C)]^c \\ \because (A^c \oplus B) \oplus C &= A^c \oplus (B \oplus C)(Associativity) \\ \therefore A \ominus B \ominus C &= A \ominus (B \oplus C). \end{aligned}$$

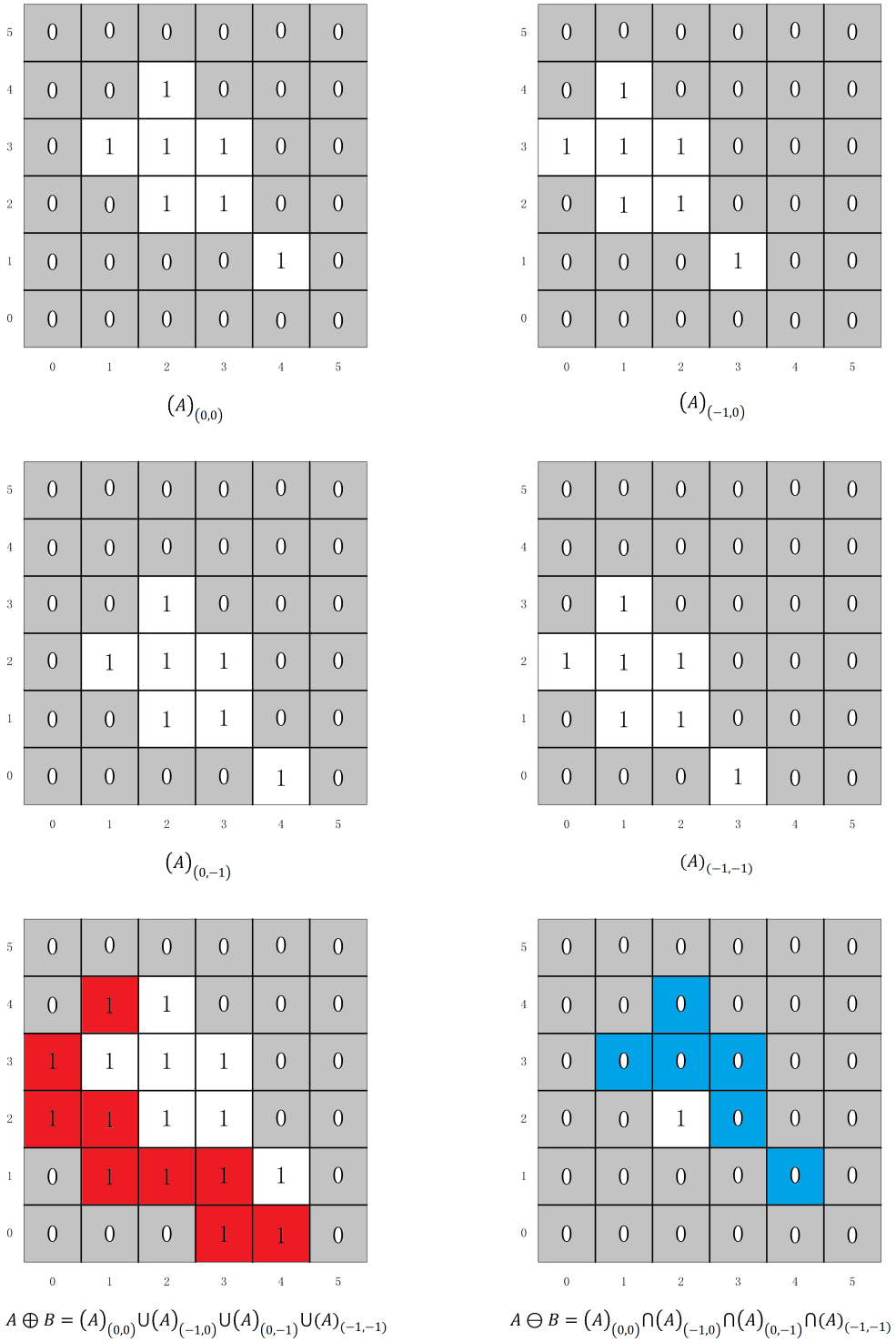

Figure 2.2: Binary dilation and erosion of the binary image

Binary Opening and Closing

As mentioned previously, all the other morphological transforms are generated by composing the two basic operators, dilation and erosion. Morphological transforms decompose complicated shapes into meaningful representations and isolate them from needless components. Matheron derived the notion of opening and closing according to the study of the framework of an axiomatisation of the concept of size [103]. Assuming a set A and an SE B. The opening of A by B, denoted $A \circ B$, is defined as:

$$A \circ B = (A \ominus B) \oplus B, \tag{2.1.9}$$

which can be concluded that the opening of A by B is simply the erosion of A by B, following by a dilation of the previous result by B. The function of opening is to break a connected feature into several unconnected portions and suppress small peaks and islands. In image processing, opening can be applied to smooth the contour, break narrow isthmuses and remove small islands or sharp peaks.

The closing of A by B, represented as $A \bullet B$, is given as:

$$A \bullet B = (A \oplus B) \ominus B, \tag{2.1.10}$$

which can be regarded as the dilation of A by B, following by a erosion of the former result by B. The closing operator is a morphological dual to opening. It also tends to remove sharp section and contours by fusing narrow breaks and long thin gulfs and also filling small holes and gaps. Smiliar to dilation and erosion, the opening and closing operators also have the property of duality presented as:

$$A \circ B = (A^c \bullet B)^c, \tag{2.1.11}$$

$$A \bullet B = (A^c \circ B)^c. \tag{2.1.12}$$

Proof:

$$(A \circ B)^c \quad = \quad (A \ominus B \oplus B)^c = (A \ominus B)^c \ominus B$$

$$
\begin{aligned}
&= A^c \oplus B \ominus B \\
&= A^c \bullet B \\
\Rightarrow A \circ B &= (A^c \bullet B)^c.
\end{aligned}
$$

2.1.2 Set Representations of Functions

Extending morphological operators to functions, the functions are expressed by their umbra [104]. The definition of umbra function is given as:

$$U(f) = \{(x, a) | a \leq f(x)\}. \tag{2.1.13}$$

According to the definition, a d-dimensional function $f(x)$ is represented by a $(d+1)$-dimensional set. It is apparent that the umbra is the set of points below the surface denoted by $f(x)$. Once the umbra is obtained, binary morphological operators can be applied to signals for signal processing. Generally, the umbra set extends to $a = -\infty$, and the function f can be restored from its umbra since:

$$f(x) = \max\{\mathrm{a} | (\mathrm{x}, \mathrm{a}) \in \mathrm{U(f)}\}, \forall \mathrm{x}. \tag{2.1.14}$$

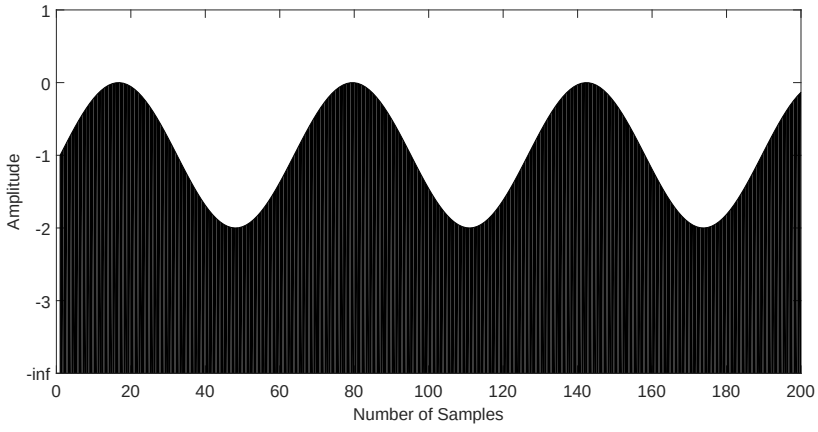

Figure 2.3: Umbra $U(f)$ of a sinusoidal function f

In Fig. 2.3, an example of the umbra of a sinusoidal function is shown, where the umbra of $f(x)$ is the shaded area. It is easy to find out that $f \leq g \Leftrightarrow$

$U(f) \subseteq U(g)$. The following presents some definitions of grey-scale operations based on sets and they are defined as [105]:

1. *Grey-scale union:* The union of two functions f and g, denoted by $f \vee g$, is given as:
$$(f \vee g)(x) = f(x) \vee g(x). \tag{2.1.15}$$
There is a one-to-one accordance between the union of functions and the set union defined as:
$$U(f \vee g) = U(f) \cup g(x). \tag{2.1.16}$$

2. *Grey-scale intersection:* The intersection of two functions f and g, denoted by $f \wedge g$, is defined as:
$$(f \wedge g)(x) = f(x) \wedge g(x). \tag{2.1.17}$$
Similarly, the one-to-one correspondence between the intersection of the function and the set is given as:
$$U(f \wedge g) = U(f) \cap U(g). \tag{2.1.18}$$

3. *Grey-scale transpose:* The transpose $\check{f}$ of a function f is defined as:
$$\check{f}(x) = f(-x). \tag{2.1.19}$$

4. *Grey-scale complement:* The complement f^c of a function f is represented as:
$$f^c(x) = -f(x). \tag{2.1.20}$$

For processing an 8-bit grey-scale digital image, where each pixel contains $2^8 = 256$ possible values to carry the full (and only) information about its intensity, the image can be expressed as a set whose components are in $\mathbb{Z}^3$. In this situation, two components of each element of the set represent the coordinates of a pixel and the third component represents its discrete intensity value. While for a signal, the set is defined in $\mathbb{Z}^2$ with each element relating to

a sample of the digitised signal. Similarly, the first component of each element denotes the coordinate and the second correspond to its value. Other attributes of the sets can also be included in higher dimensional space, for example colour information of an image [22].

2.1.3 Definitions for Grey-scale Operations

In order to expand the application of MM in signal processing where most signals are not binary, morphological operators should be extended to a grey-scale level. Grey-scale digital signals can be expressed as sets whose components are in $\mathbb{Z}^2$, the discrete Euclidean space. By expanding the basic binary operators to grey-scale signals or images, grey-scale dilation, erosion, opening and closing are obtained.

Grey-scale dilation and erosion

As introduced previously, binary dilation and erosion are performed by union and intersection, while in the grey-scale condition, they are performed by algebraic addition and subtraction. Let f represents a signal and g denotes SE, and the length of g be relatively shorter than that of f. The grey-scale dilation and erosion are defined as:

$$f \oplus g(x) = \max_s\{f(x+s) + g(s) | (x+s) \in \mathcal{D}_f, s \in \mathcal{D}_g\}, \quad (2.1.21)$$

$$f \ominus g(x) = \min_s\{f(x+s) - g(s) | (x+s) \in \mathcal{D}_f, s \in \mathcal{D}_g\}, \quad (2.1.22)$$

where $\mathcal{D}_f$ and $\mathcal{D}_g$ are the definition domains of f and g, respectively.

For example, assume that the SE g has a length of three samples with its origin in the middle. In this situation, the definition domain of g is represented by $\mathcal{D}_g = \{-1, 0, 1\}$. Therefore, the dilation and erosion of f by g are calculated by

$$f \oplus g(x) = \max\{f(x-1) + g(-1), f(x) + g(0), f(x+1) + g(1)\},$$

and

$$f \ominus g(x) = \min\{f(x-1) - g(-1), f(x) - g(0), f(x+1) - g(1)\},$$

respectively. Similar to binary dilation and erosion, the function of grey-scale dilation is to swell or expand the target signal, while that of grey-scale erosion is to shrink the target signal.

The SE is a small set applied to probe the signal. A simple scenario is that the SE has the form of $g(s) \equiv 0, s \in \mathcal{D}_g$, which is called a 'flat SE'. As a consequence, definitions of dilation and erosion become:

$$f \oplus g(x) = \max_s\{f(x+s) | (x+s) \in \mathcal{D}_f, s \in \mathcal{D}_g\}, \quad (2.1.23)$$

$$f \ominus g(x) = \min_s\{f(x+s) | (x+s) \in \mathcal{D}_f, s \in \mathcal{D}_g\}. \quad (2.1.24)$$

In this case, the SE g is applied to point out which sample is involved when processing the target signal. For a binary signal, the SE must be flat. An example of the dilation and erosion of a one-dimensional signal is demonstrated in Fig. 2.4. Both operations use a flat-line SE with the length of three: $g(-1) = g(0) = g(1) = 0$.

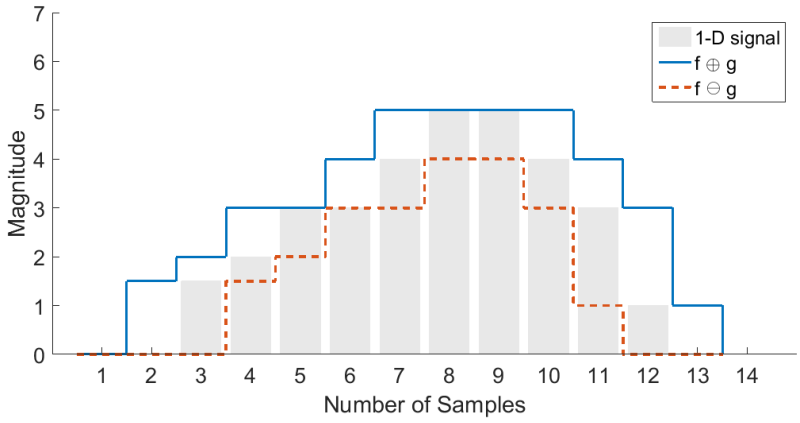

Figure 2.4: Grey-scale dilation and erosion of a one-dimensional signal

Fig. 2.4 also illustrates another characteristic of dilation and erosion, i.e. that they are increasing transforms. *Increasing* property is given as follows. For two signals f_1 and f_2, and an arbitrary SE, g, we have:

$$f_1 \leq f_2 \Rightarrow \begin{cases} f_1 \oplus g \leq f_2 \oplus g \\ f_1 \ominus g \leq f_2 \ominus g \end{cases} \tag{2.1.25}$$

According to the example in Fig. 2.4, the ordering relation between dilation and erosion can be represented by the erosion of a signal by SE being less than or equal to its dilation by the same SE: $f \ominus g \leq f \oplus g$. If the SE processes a sample of the signal within a window that includes the sample, the following sequencing is obtained:

$$f \ominus g \leq f \leq f \oplus g. \tag{2.1.26}$$

Grey-scale opening and closing

Similar to the binary operators, different combinations of the grey-scale dilation and erosion can produce the operations of grey-scale opening and closing. The definition of opening is expressed as:

$$f \circ g = (f \ominus g) \oplus g, \tag{2.1.27}$$

where f is the signal to be processed, g is the SE, and $\circ$ denotes the opening operator. The function of opening is to recover most structures lost due to erosion through dilation, except for those completely erased by erosion. According to their duality, the defintion of closing is defined as:

$$f \bullet g = (f \oplus g) \ominus g. \tag{2.1.28}$$

Generally, the function of closing is to erode the excessively dilated parts. Both opening and closing can be applied to smooth the signal contour and they are normally combined with each other to be utilised in signal processing. The performance of opening and closing on the same one-dimensional signal applied in the previous section by the same flat-line SE is presented in Fig. 2.5. From the result of closing, it is obvious that the bulge in the middle is removed. As for the outcome of opening, the eroded part has been recovered and due to the function of dilation in the operation, the swelling part still exist. Therefore, it can be concluded that opening is more suitable for filling hollows and closing has its advantage in removing bulges in signal processing.

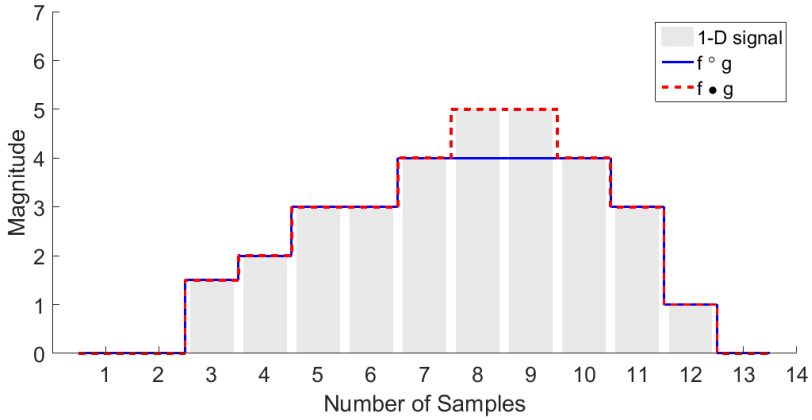

Figure 2.5: Grey-scale opening and closing of a one-dimensional signal

2.2 Advanced Morphological Operators

The advanced morphological operators are derived from the basic ones and different combinations of basic operators with various selections of SE can generate diverse advanced operators for a variety of purposes. In the following sections, the advanced morphological operators applied in this thesis will be introduced.

2.2.1 Multi-Resolution Morphological Gradient (MMG)

Before describing MMG, the morphological gradient (MG) is introduced firstly. MG is the difference between the dilation and the erosion of a given image or signal. Let the given signal be f and the SE be g. The definition of MG denoted as ρ_G is given as:

$$\rho_G = f \oplus g - f \ominus g. \tag{2.2.1}$$

There are two types of half-gradient [106, 107]. One is named internal gradient, expressed as I_G. It is described as the difference between the original signal or image and the outcome after erosion and it is defined as:

$$I_G = f - (f \ominus g). \tag{2.2.2}$$

On the other hand, the other is called the external gradient, denoted as E_G, which is defined as the difference between the result after dilation and the original signal or image:

$$E_G = (f \oplus g) - f. \tag{2.2.3}$$

The internal gradient enhances internal boundaries of the target signal or image while the external one extracts external boundaries. Furthermore, referring to these definitions, it is apparent to conclude that:

$$\rho_G = I_G + E_G. \tag{2.2.4}$$

This is also the reason why they are named "half gradients". According to previous research, MG has benefit on extracting sudden changes when processing a signal, for example, current transformers (CT) saturation in power systems [108]. An example of the performance of MG on the previous one-dimensional digital signal with the same flat SE is illustrated in Fig. 2.6. It is apparent that when the amplitude of the signal starts to change the result of MG changes simultaneously shown as the bumps in the figure.

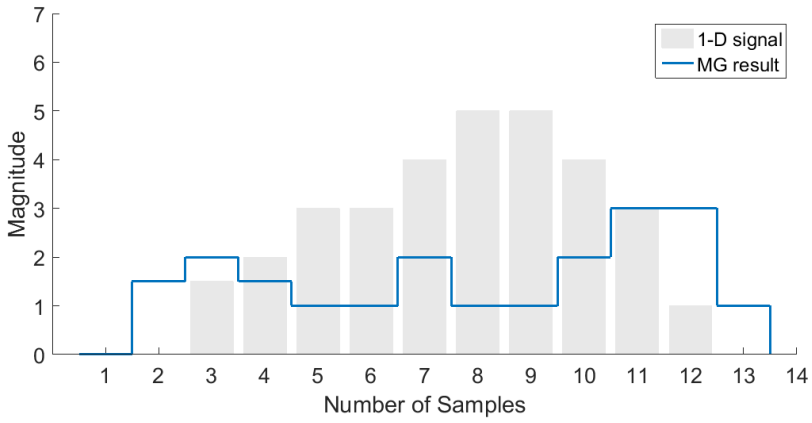

Figure 2.6: Morphlogical gradient of a one-dimensional signal

The concept of multi-resolution analysis was introduced to MM in order to achieve the goal of emphasising sudden changes together with suppressing noise at the same time. In [39, 109], researchers proposed MMG to extract a travelling wavefront. They indicated that MMG could be used to suppress

the steady-state components and enhance the transient ones. Due to these advantages of MMG, it was applied to extract the features of power quality disturbances in signals. For the purpose of extracting increasing and decreasing edges of transient signals, MMG is designed to propose two scalable flat line SE, G^+ and G^-, with different origins given as:

$$G^+ = \{g_1, g2, \cdots, g_{l-1}, \underline{g_l}\}, \tag{2.2.5}$$

$$G^- = \{\underline{g_1}, g2, \cdots, g_{l-1}, g_l\}, \tag{2.2.6}$$

where G^+ is the SE applied to detecting the rising edges and G^- on the contrary, is to extract the falling edges. The length of the SE is calculated by $l = 2^{1-a} l_g$, where a is the level of MMG to be processed, l_g denotes the primary length of SE at level one. The underlined samples in G^+ and G^- represent their origin. According to the definition of MG in (2.2.1) and the previous scalable SEs, the dyadic MMG ρ_G^a with level a is defined as:

$$\rho_{G^+}^a = (\rho^{a-1} \oplus G^+)(x) - (\rho^{a-1} \ominus G^+)(x), \tag{2.2.7}$$

$$\rho_{G^-}^a = (\rho^{a-1} \ominus G^-)(x) - (\rho^{a-1} \oplus G^-)(x), \tag{2.2.8}$$

$$\rho_G^a = \rho_{G^+}^a + \rho_{G^-}^a. \tag{2.2.9}$$

When $a = 1$, $\rho^0 = f$ is the input signal. Since $(\rho^{a-1} \oplus G)(x) \subset (\rho^{a-1} \ominus G)(x) : D_G \neq \varnothing$, then $\rho_{G^+}^a > 0$ and $\rho_{G^-}^a < 0$, which correspond to the increasing and decreasing edges of the target signal [109]. Additionally, more details correspond to the changes could be revealed if a higher level is processed. The relative application and setting of the improved MMG with specific SE will be further presented in Chapter 3.

2.2.2 Morphological Filters

A morphological filters (MF), which is a non-linear signal transform, can be applied to alter the geometrical characteristics of signals or image objects locally. In MM, a transformation or operator ψ is called a filter and must satisfy two necessary and sufficient conditions: ψ is increasing and idempotent. The property of increasing implies that the ordering relation on signals is

maintained after the filtering process if the same SE is applied. The idempotent property can be expressed as: $\psi^2 = \psi$, which means that applying the MF twice to a signal or image is equivalent to applying it only once [110]. The two basic operators introduced previously, opening and closing, are two popular MFs and both of them satisfy the properties of increasing and idempotent. Based on these MFs, several popular MFs have been developed, for instance:

$$\psi = f \circ g \bullet g, \tag{2.2.10}$$

$$\psi = f \bullet g \circ g, \tag{2.2.11}$$

$$\psi = [f \circ g \bullet g + f \bullet g \circ g]/2. \tag{2.2.12}$$

These are the most commonly used filters derived from opening and closing. The first is called the *opening−closing* and the second is the *closing−opening*. The third one is the combination of the former two MFs and this combination can result in impairing the statistical deviation problems existing in $opening - closing$ and $closing - opening$ filters. This implies that new filters can be designed from their sequential combinations in order to achieve different purposes. MFs have been widely applied to reduce noise in both signal and image processing. In the following section, three different MF applied in this thesis are introduced.

Envelope Extraction Morphological Filter

An envelope extraction MF, as the name implies, is an MF for extracting the envelope of a signal. For extraction of the upper envelope of a signal, the upper envelope extraction MF is defined as:

$$f_{ue} = (S \oplus G) \bullet G, \tag{2.2.13}$$

which is the dilation of S by G, following by a closing of the previous result by the same G. As for the definition of lower envelope extraction MF, it is given as:

$$f_{le} = (S \ominus G) \circ G, \tag{2.2.14}$$

where S and G denote the input signal and the SE, respectively and the MF is simply the erosion of S by G, following by a opening by the same G. An example of the performance the envelope extraction method is illustrated in Fig. 2.7. In the original signal, a fundamental frequency component of 50 Hz

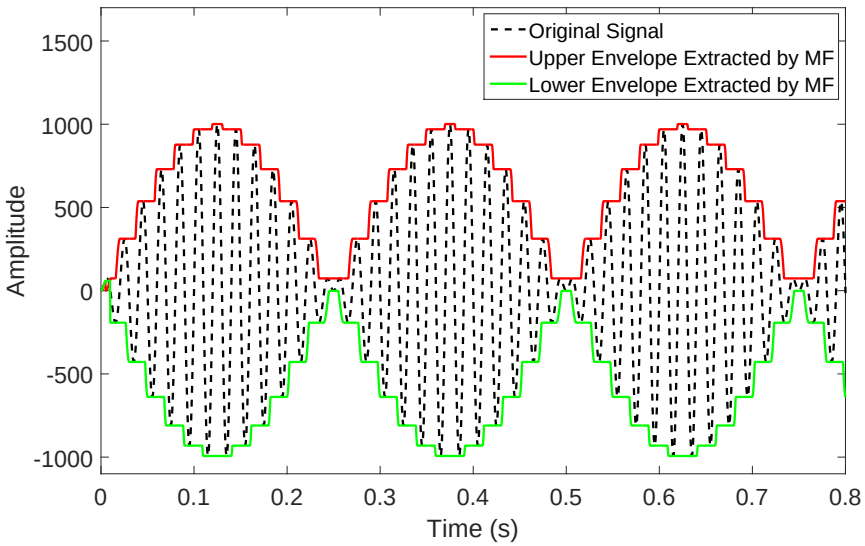

Figure 2.7: An example of extraction of upper and lower envelopes of a signal using envelope extraction MF

and a 2 Hz frequency component are included and a flat-line SE is selected for the extraction. Furthermore, it is apparent that both the upper and lower envelopes are extracted successfully by the MF. Due to these properties, the envelope extraction MF will be applied for extraction of continuous LFO components in power systems and the detail will be further illustrated in Chapter 4.

LFO Extraction Morphological Filter

Also in the same chapter, another MF compromising *opening* − *closing* and *closing* − *opening* operators is also proposed and applied to directly extract damped LFO components. The expression of *opening* − *closing*, *closing* − *opening* and the LFO extraction MF are given respectively as:

$$f_{\text{opcl}} = S \circ G \bullet G, \tag{2.2.15}$$

$$f_{\text{clop}} = S \bullet G \circ G, \tag{2.2.16}$$

$$f_{\text{dlfo}} = \left(f_{\text{opcl}} + f_{\text{clop}}\right)/2, \tag{2.2.17}$$

where the output of f_{dlfo} is the required damped LFO components. The specific selection of SE will also be further revealed in Chapter 4.

Convolved Morphological Filter

Convolved Morphological Operators Generally, linear methods are widely applied for analysis and design in time and frequency domains. However, images are easily blurred when applying linear filtering according to several studies [22]. On the contrary, MF can maintain the image without blurring the detailed features in image processing. Due to this feature, this section introduces and illustrates a novel method which combine MF with convolution in order to enhance the performance of the morphological filtering technique.

Formal definitions of convolved morphological operators were introduced in [101] and they are presented as follows. Firstly, let the input signal $i(t)$ be expressed in the form shown below:

$$\begin{aligned} i(t) = {} & A_1 \cos\left(2\pi f_1 t + \phi_1\right) + \cdots \\ & + A_k \cos\left(2\pi f_k t + \phi_k\right) + e(t), \end{aligned} \tag{2.2.18}$$

where $0 < f_1 < f_2 < \cdots < f_k < \frac{f_s}{2}$ and $e(t)$ is white Gaussian noise. The objective of the designed filter is to extract the desired frequencies in a narrow band and remove the other signal components, such as harmonics, at the same time. The algorithm depicted here is designed to convolve the output of the pre-designed MF with a proper selected impulse response function $h(t)$ in order to obtain a filter that can preserve the waveform of the fundamental frequency component in the time domain with the desired frequency response. Assume that $f_{\text{mo}}(t)$, $h(t)$ and $f_{\text{cmo}}(t)$ denote the output of the morphological operator, the impulse response of linear filter, and the output of CMO, respectively. $f_{\text{cmo}}(t)$ is defined as:

$$f_{\text{cmo}}(t) = h(t) * f_{\text{mo}}(t) = \sum_{\tau} h(\tau) \cdot f_{\text{mo}}(t - \tau), \tag{2.2.19}$$

where $\tau \in D_h$, $t-\tau \in D_{\text{mo}}$, D_h is the range of h in the time domain, D_{mo} is the range of MO in the time domain and $*$ denotes convolution. The equivalent equation in the frequency domain is presented as:

$$F_{\text{cmo}}(f) = H(f) \cdot F_{\text{mo}}(f). \tag{2.2.20}$$

Consequently, the convolved morphological operators, convolved erosion $f_{\text{cer}}(t)$, dilation $f_{\text{cdi}}(t)$, opening $f_{\text{cop}}(t)$, closing $f_{\text{ccl}}(t)$, opening-closing $f_{\text{copcl}}(t)$ and closing-opening $f_{\text{cclop}}(t)$ are respectively defined as:

$$\begin{aligned} f_{\text{cer}}(t) &= \sum_{\tau} h(\tau) \cdot f_{\text{er}}(t-\tau) \\ &= \sum_{\tau} h(\tau) \cdot \min_{u} \left\{ f(t+u-\tau) - g(u) \right\}, \end{aligned} \tag{2.2.21}$$

$$\begin{aligned} f_{\text{cdi}}(t) &= \sum_{\tau} h(\tau) \cdot f_{\text{di}}(t-\tau) \\ &= \sum_{\tau} h(\tau) \cdot \max_{u} \left\{ f(t-u-\tau) + g(u) \right\}, \end{aligned} \tag{2.2.22}$$

$$\begin{aligned} f_{\text{cop}}(t) &= \sum_{\tau} h(\tau) \cdot f_{\text{op}}(t-\tau) \\ &= \sum_{\tau} h(\tau) \cdot \max_{v} \{ \min_{u} \{ f(t+u-v-\tau) \\ &\quad -g(u) + g(v) \} \}, \end{aligned} \tag{2.2.23}$$

$$\begin{aligned} f_{\text{ccl}}(t) &= \sum_{\tau} h(\tau) \cdot f_{\text{cl}}(t-\tau) \\ &= \sum_{\tau} h(\tau) \cdot \min_{v} \{ \max_{u} \{ f(t-u+v-\tau) \\ &\quad +g(u) - g(v) \} \}, \end{aligned} \tag{2.2.24}$$

$$f_{\text{copcl}}(t) = \sum_{\tau} h(\tau) \cdot f_{\text{opcl}}(t-\tau)$$

$$= \sum_{\tau} h(\tau) \cdot \max_{w}\{\min_{v}\{\min_{u}\{\max_{s}\{ f(t-s+u+v-w-\tau) +g(t)-g(u)-g(v)+g(w)\}\}\}\}, \quad (2.2.25)$$

$$f_{\text{cclop}}(t) = \sum_{\tau} h(\tau) \cdot f_{\text{clop}}(t-\tau) = \sum_{\tau} h(\tau) \cdot \min_{w}\{\max_{v}\{\max_{u}\{\min_{s}\{ f(t+s-u-v+w-\tau) -g(t)+g(u)+g(v)-g(w)\}\}\}\}, \quad (2.2.26)$$

where $t, u, v, \omega \in D_g$ and $\alpha \in D_f$.

Convolved Morphological Filters As explained previously, a morphological operator is called an MF if it is increasing, idempotent, and extensive or anti-extensive. Therefore, convolved erosion and dilation can only be regarded as operators not filters as they are not idempotent. The general MF applied in the CMF is expressed as:

$$r(t) = \frac{[f_{\text{opcl}}(i(t)) + f_{\text{clop}}(i(t))]}{2}, \quad (2.2.27)$$

where $i(t)$ is the original signal and $r(t)$ represents the output signal after applying the MF. However, different from most conventional filters, the bandwidth of the MF is determined by the shape of the SE. The SE will greatly affect the performance of the MF, as well as the CMF. Therefore, besides determining a suitable impulse response functions, the selection of proper SE is another critical issue. By composing a structuring element $g(t)$, which has a shape of half of a sinusoid with its peak at its centre, the shapes smaller than $g(t)$ will be removed from the original signal. Suppose that there is a signal which has a sampling frequency of f_s. In order to remove the frequency higher than f, the size of $g(t)$ should be calculated as: $\frac{f_s/2}{f}$. Furthermore, in order to obtain better results after morphological filtering, the MF is applied twice.

In the second process of MF, the length of the SE is increased to $\frac{f_s/2}{f'}$, where $f' < f$. Thus, the complete operation for the low-pass MF is shown as:

$$f_{\text{low}}(t) = \frac{[f_{\text{opcl}}(r(t)) + f_{\text{clop}}(r(t))]}{2}, \tag{2.2.28}$$

where $f_{\text{low}}(t)$ is regarded as the low-pass MF. Once the signal is filtered by the MF, the next procedure is to apply the convolution to the signal with pre-selected $h(t)$, and the convolution is expressed as:

$$f_{\text{cmf}}(t) = \sum_{\tau} h(\tau) \cdot f_{\text{low}}(t - \tau), \tag{2.2.29}$$

where $f_{\text{cmf}}(t)$ generates the output signal of CMF.

To sum up, the general procedure for filtering signals using CMF is:

1. Determine suitable SE for MF (both shape and size);
2. Apply proper morphological operators to preserve expected shapes in time domain. Generally, $(f_{\text{opcl}}(t) + f_{\text{clop}}(t))/2$ is selected as the operator applied in the MF;
3. Choose proper impulse response function, $h(t)$, for convolution;
4. After morphological filtering, convolve the results with the pre-designed $h(t)$.

In [101], only the Dirac delta function is selected as the impulse response function in the convolution process. Additionally, there are a variety of options in determining the proper impulse response function for CMF. Different impulse response functions can lead to different results of convolution process, as well as the CMF. As a consequence, it is of curiosity and importance to compare the performance of CMF with different impulse response functions and the determination of different impulse response functions will be given in Chapter 5. Furthermore, because of the importance of selecting appropriate SE, an improved MF with optimised SE is proposed and the detail is also included in the Chapter 5.

2.2.3 Conclusions

This chapters studies the mathematical background of MM and introduces the development of the basic morphological operators, including brief proofs of some significant characteristics of the operators. Basic morphological operators, containing dilation, erosion, opening and closing, can be defined in both binary and grey-scale situations. The grey-scale morphological operators are considered in this thesis and several examples have also been provided to make a clearer understanding of these operators.

A set of advanced morphological operators based on the basic ones are then presented, including MG, MMG, envelope extraction MF, LFO extraction MF and CMF. MG are adept in detecting sudden changes in signals, which can be applied for detecting disturbances of transient signals. MMG, as its name suggests, is a higher version of MG and has better performance when a noisy environment is considered. The envelope extraction MF makes an achievement in successfully extracting both the upper and lower envelopes of the target signal and provides group search optimiser (GSO) algorithm with enough envelope information for calculating parameters of the continuous LFO component and reconstructing it. The LFO extraction MF, can be applied for direct extraction of the damped LFO components. CMF, combination of MF and convolution process, extracts the desired frequency component with narrow bandwidth and has benefit in eliminating other frequency components. The advanced morphological operators proposed and applied will be further illustrated in the following chapters, respectively.

Chapter 3

Dectection and Classification of Power Quality Disturbances

Power quality disturbances have always been of great importance to both electricity consumers and electrical utilities. Some disturbances might only briefly interfere with the most highly sensitive equipment. While others, as a result of extensive damage to the electric delivery systems, could lead to total loss of power for days. Therefore, it is necessary to minimise the influences of power quality disturbances by carefully detecting and classifying them for further analysis.

Multi-resolution decomposition scheme is a robust and significant technique for signal processing. Inspired by the application of MMG in [51], this chapter proposes a refined MMG algorithm based on MG to detect typical power quality disturbances. Additionally, as an improvement of the MMG approach, trapezoid SEs are applied. Utilising the proposed method to detect different types of typical power quality disturbances, the simulation results are satisfactory even in consideration of noisy environments. Furthermore, a *closing* operator is also used for the classification of the detected disturbances and the simulation outcomes of the proposed method are also approving.

3.1 Multi-Resolution Morphological Gradient (MMG)

As introduced formerly, the MMG algorithm is derived from MG which is based on basic morphological operators. Morphological operators are a set of transformations which are effective in processing signals or extracting desired features. Let S and G denote the input set and SE, respectively. Two basic operators of MM, *dilation* and *erosion* can be defined as follows respectively:

$$\delta_G(S) = S \oplus G = \bigcup_{g \in G} (S + g), \tag{3.1.1}$$

$$\varepsilon_G(S) = S \ominus G = \bigcap_{g \in G} (S - g). \tag{3.1.2}$$

MG is defined as the subtraction of *erosion* from *dilation*. The MG is denoted as:

$$\rho_G = \delta_G(S) - \varepsilon_G(S). \tag{3.1.3}$$

As mentioned in the previous chapter, MG can detect sudden changes of waveforms. In this thesis, two scalable trapezoid SEs, G_1 and G_2, are applied to extract the rising edges and the falling edges of the input signal respectively. They are defined as:

$$G_1 = \{g_1, 0, \cdots, 0, g_2\}, \tag{3.1.4}$$

$$G_2 = \{g_1, 0, \cdots, 0, 0\}, \tag{3.1.5}$$

where g_1 is set to be the peak value in the original signal, and g_2 is set to be a threshold, which can be the maximum value of the disturbance signal existed in the sinusoidal signal or higher than that. By introducing these two SEs, the computational complexity of the MMG is further reduced. According to [51], the length of SE is calculated by $l = 2^{1-a} l_G$, where a is the level of SE and l_G is the primary length of the SE of G. According to the definitions of MG and SE, the dyadic MMG can be defined as:

$$\rho^a_{G_1} = \delta_{G_1}(\rho^{a-1}) - \varepsilon_{G_1}(\rho^{a-1}), \tag{3.1.6}$$

$$\rho^a_{G_2} = \delta_{G_2}(\rho^{a-1}) - \varepsilon_{G_2}(\rho^{a-1}), \tag{3.1.7}$$

$$\rho^a = \rho^a_{G_1} + \rho^a_{G_2}. \tag{3.1.8}$$

The technique of quadratic MMG (level $a = 2$) is processed to extract the features of typical power quality disturbances in the signal. The extracted results can be used to detect and locate the disturbances. The Difference between other approaches applying MMG is that the method proposed in this chapter applies trapezoid SEs and does not need to initially use an MF to remove the noise in the input signal. In other words, this improved version of MMG algorithm is noisy resistant to some extent.

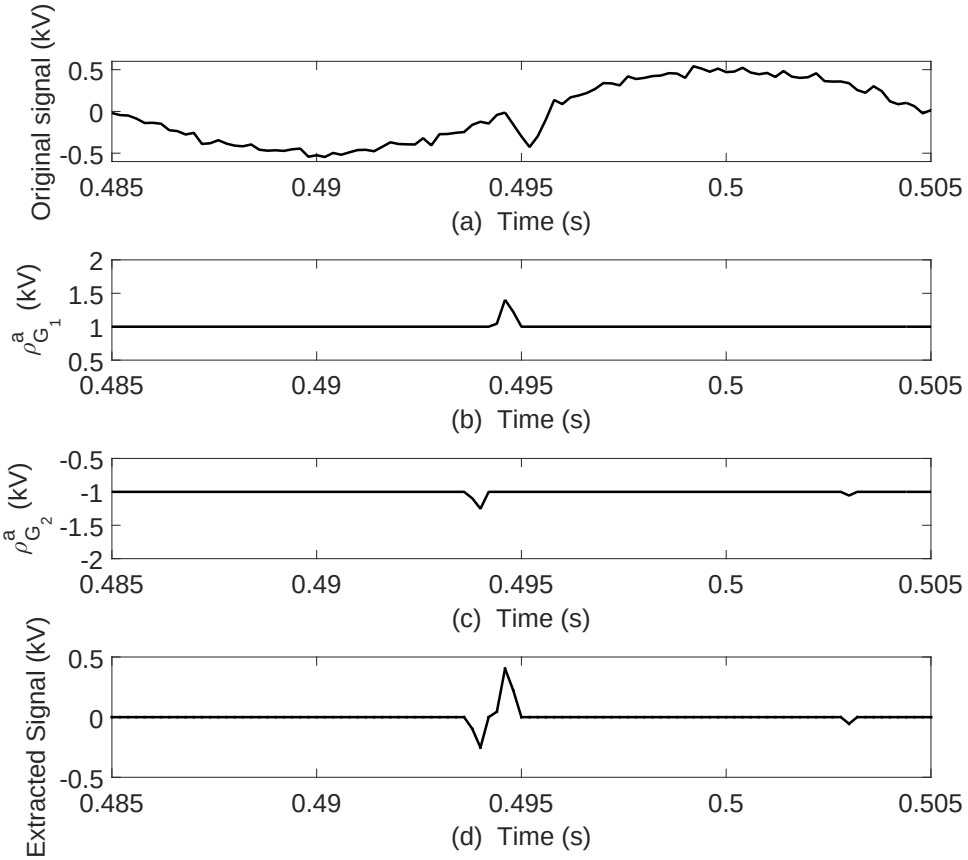

Figure 3.1: Identification process using MMG: (a) original signal; (b) result of $\rho^a_{G_1}$; (c) result of $\rho^a_{G_2}$; (d) extraction result of MMG

Figure 3.1 illustrates the process of how MMG works on the target signal. The rising and falling edges are both detected and extracted by using MMG.

Additionally, in the selection of SEs, G_1 is able to remove the sharp parts of the sinusoidal signal, and to maintain the disturbance in the signal. G_2 is able to detect the falling and rising edge of the signal. Therefore, the final extraction contains all the information related to the disturbance. Moreover, by adjusting the threshold value g_2 in the SE G_1, the performance of MMG can be further improved.

3.2 Detection of Power Quality Disturbances

In this section, MMG is applied to investigate different types of typical power quality disturbances, including voltage sag, momentary interruption, voltage swell and damped oscillatory transient. Additionally, the original sinusoidal signal with fundamental frequency of 50 Hz is polluted by a signal-to-noise ratio (SNR) value of 30 dB white Gaussian noise (WGN). The sampling frequency used is 5 kHz for all cases in the simulation studies. Note that all the simulation studies are carried out on a Dell PC with 3.4 GHz Intel Core i7-2600 CPU and 8.00 GB RAM using MATLAB 2015a.

3.2.1 Voltage Sag

A voltage sag is a significant voltage decrease for a relatively short duration. It may be caused by faults, increased load demand and transitional events such as starting large electrical motors.

Fig. 3.2 shows a typical voltage sag with depth of 0.3 kV and duration of 0.001 second occurring approximately in the middle between the positive peak to the negative peak on the second cycle of the sinusoidal input signal and the detection of the voltage sag by the MMG algorithm, respectively. This figure depicts that the location time of the advent of the voltage sag is detected successfully in a noisy environment.

In Fig. 3.3, the disturbance with the same depth and duration happens in the middle between the negative peak to the positive peak and it is apparent that this sag is also detected shown as a small impulse on the waveform of the

extracted signal. In order to evaluate the performance of this method, several other signals have been tested by changing the amplitude and position of the voltage sag and similar results have been obtained.

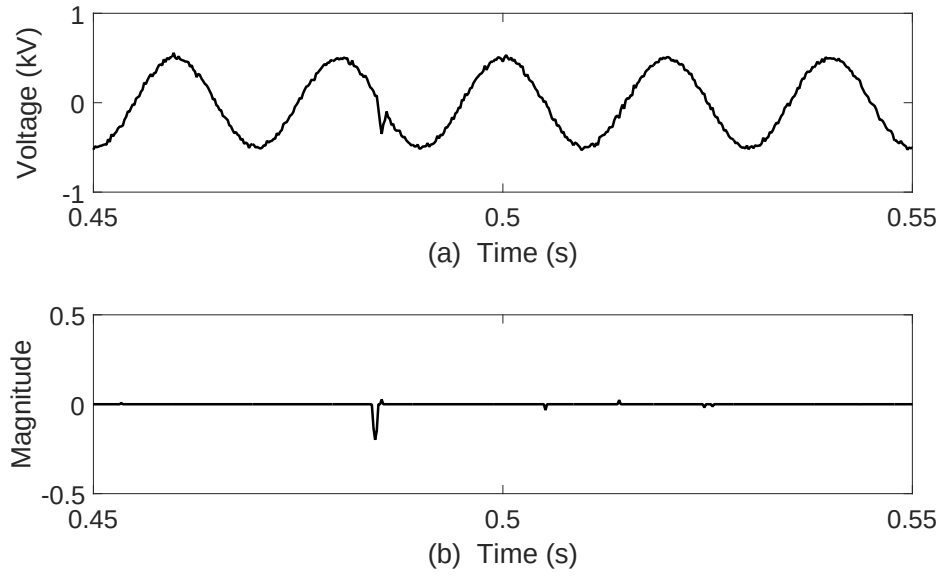

Figure 3.2: Analysis results for the case of voltage sag: (a) fundamental signal with a voltage sag; (b) result of MMG for detection of the voltage sag.

3.2.2 Momentary Interruption

A momentary loss of voltage on a power system can be regarded as a momentary interruption. This disturbance describes a descent of 90-100% of the rated system voltage lasting from 10 milliseconds to 1 minute [51].

The waveform in Fig. 3.4 (a) gives an example of typical momentary interruption. Obviously, the start and end of the disturbance are detected by using the MMG as can be observed from the extracted feature in Fig. 3.4 (b).

Considering the worst case for the detection of the momentary interruption, it is shown in Fig. 3.5 (a), where the amplitude of the input signal drops to zero during the interruption which occurs in the third cycle when the signal is approximately in the middle between the negative peak and the positive peak

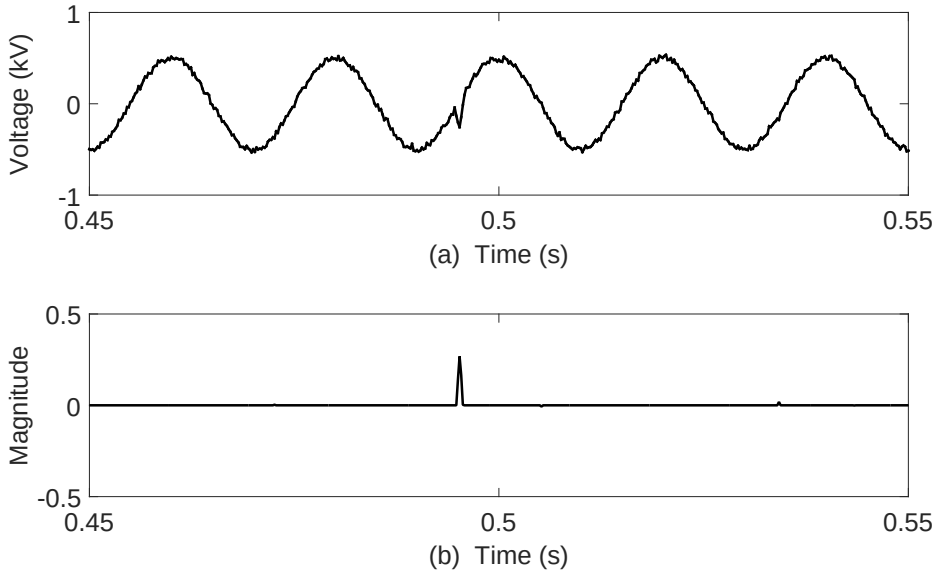

Figure 3.3: Analysis results for the case of voltage sag: (a) fundamental signal with a voltage sag; (b) result of MMG for detection of the voltage sag.

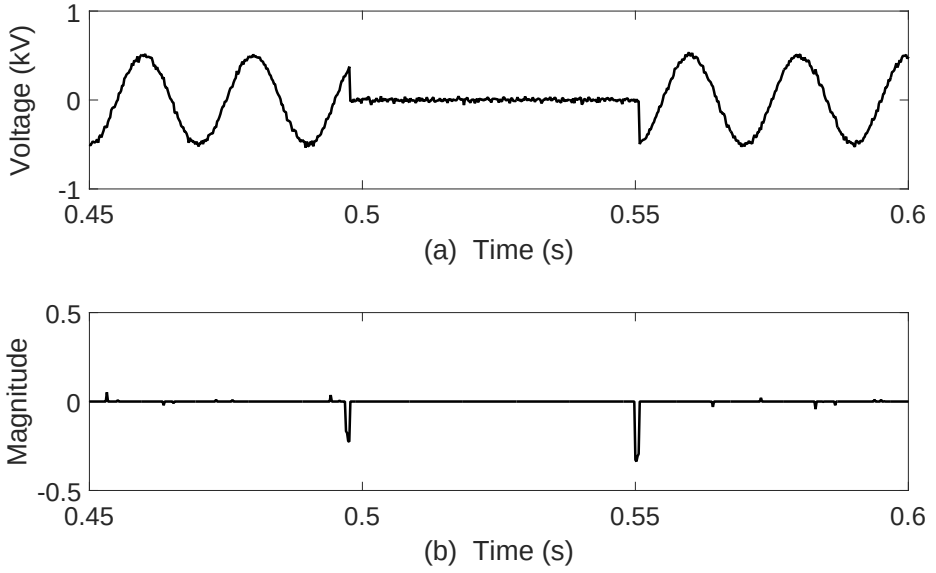

Figure 3.4: Analysis results for the case of momentary interruption: (a) fundamental signal with a momentary interruption; (b) result of MMG for detection of the momentary interruption.

and ends in the middle of the fifth cycle (lasts approximately 0.05 second). Usually, the appearance and vanishing of the momentary interruption in this situation is difficult to be identified since the gradient change is extremely tiny in this harsh scenario. However, Fig. 3.5(b) shows that the start and the end of the interruption are clearly detected by using MMG. Moreover, the performance of the proposed method is not influenced by 30 dB WGN and the noise is almost removed from the extracted feature signal. Variation of the duration and occurring position of the momentary interruption have also been simulated and MMG detects the disturbances effectively and successfully in most scenarios.

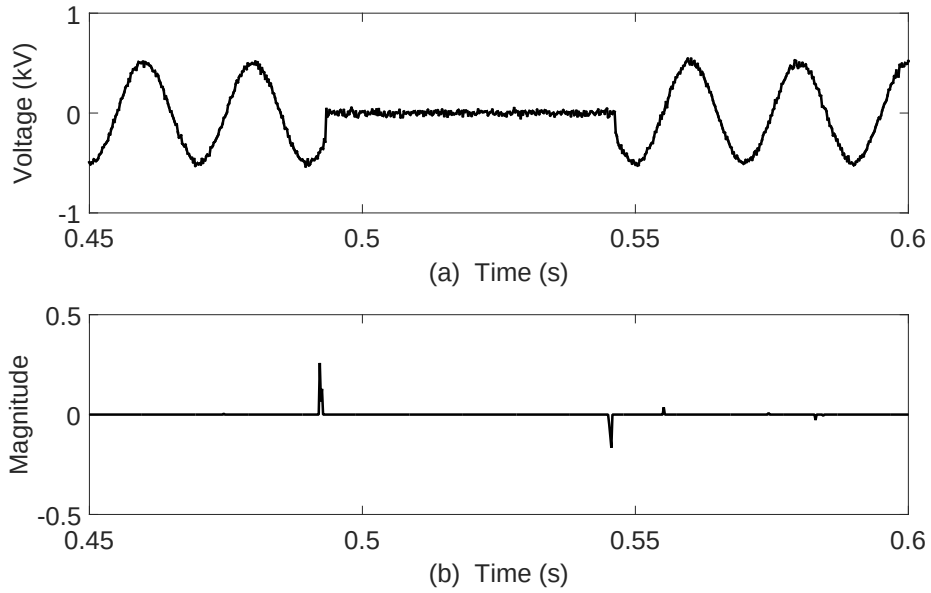

Figure 3.5: Analysis results for the case of momentary interruption: (a) fundamental signal with a momentary interruption; (b) result of MMG for detection of the momentary interruption.

3.2.3 Voltage Swell

A voltage swell is a short-term ascent of system voltage. This disturbance is generally resulted from an abrupt reduction in load or appears on the unfaulted phases of a three-phase circuit, where a single-phase short circuit has

occurred. Voltage swell may stress the electrical components and result in premature failure in power systems.

A representative voltage swell, which occurs at 0.48 second and ends at 0.51 second, is presented in Fig. 3.6 (a). The relative extracted feature is illustrated in Fig. 3.6 (b). Apparently, the starting and ending points are detected successfully while there are some tiny jagged notches which can be neglected. These slight notches are caused by the interference of the WGN.

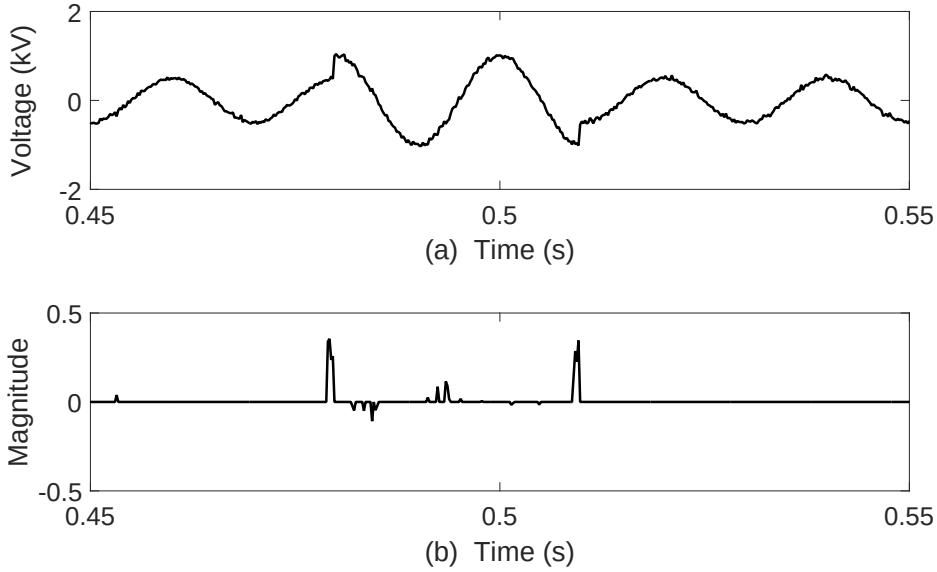

Figure 3.6: Analysis results for the case of voltage swell: (a) fundamental signal with a voltage swell; (b) result of MMG for detection of the voltage swell period.

Similarly, under the consideration of the worst scenario, in Fig. 3.7(a), a voltage swell with twice the amplitude of the fundamental signal starts on the third cycle when the signal is in the approximate middle of positive and negative peak and it lasts about 1.5 cycles (0.03 second). Fig. 3.7(b) reveals that the start and end positions of the swell period are clearly indicated by the impulses with higher amplitudes. Moreover, due to the WGN and selection of threshold value g_2, there are a handful of tiny impulses in the extracted signal during the swell period. Several changes have been made on the duration

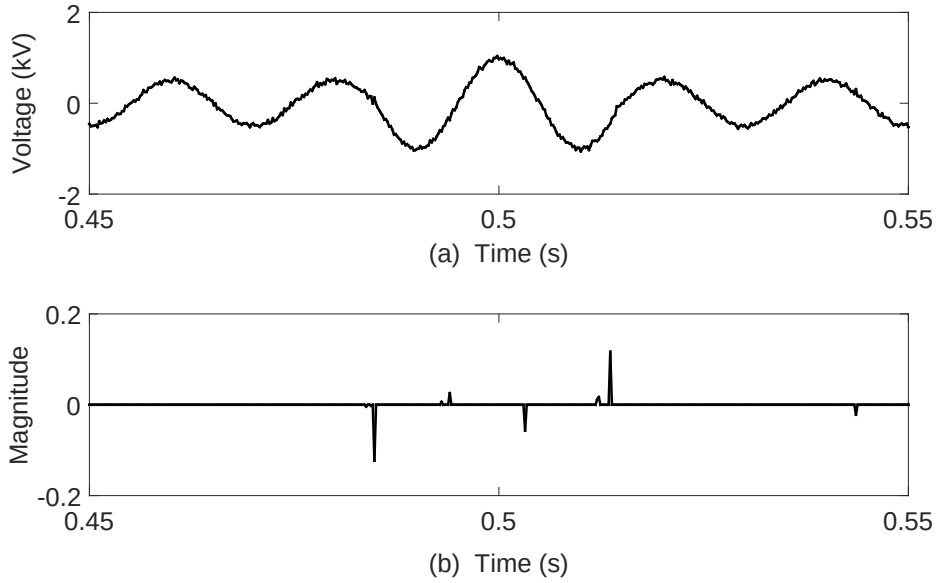

Figure 3.7: Analysis results for the case of voltage swell: (a) fundamental signal with a voltage swell; (b) result of MMG for detection of the voltage swell period.

and occurring position of the voltage swell and similar outcomes have been achieved.

3.2.4 Oscillatory Transient

A transient is an undesirable momentary deviation of the supply voltage or load current. Oscillatory transients are generally categorised into two categories: impulsive and oscillatory. In this case, damped oscillatory transients have been considered and applied.

Fig. 3.8 describes a damped oscillatory transient occurring from the third cycle to the fifth cycle of the signal (lasts approximately 0.03 second) and the extracted signal using MMG, respectively. From these plots, the start position of the transient is clearly detected in noisy environments. However, when the intensity of the transient component decreases, the end point of the transient can not be distinctly detected since the amplitude of the WGN is similar to that of the decreased oscillatory transient. Moreover, the location of the peak

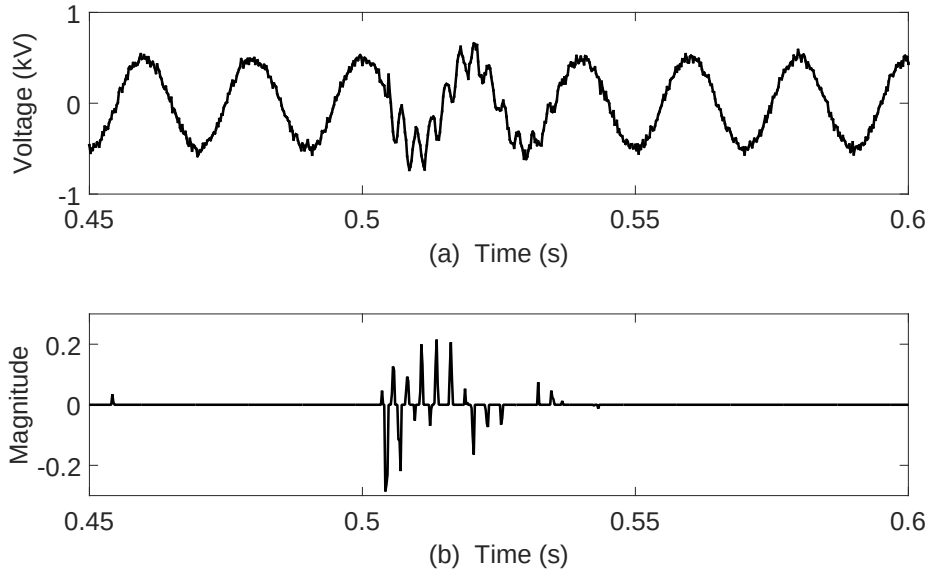

Figure 3.8: Analysis results for the case of damped oscillatory transients (30 dB WGN): (a) fundamental signal with a damped oscillatory transient; (b) result of MMG for detection of the damped oscillatory transients.

of the extracted feature is found to correspond with the time scale when the damped oscillatory transient occurs.

Another example when the amplitude of oscillatory transient decreases and the value of SNR increases to 35 dB is depicted in Fig. 3.9. It is apparent that the amplitude of the extracted feature is also reduced but the detection of the disturbance is successful. A large number of simulation tests have been carried out by changing the frequency, onset and duration of transients and similar results have been obtained.

3.2.5 Analysis

The performance of MMG can be improved by selecting the best threshold value g_2 in the trapezoid SE G_1 for each power disturbance case. By undertaking a large number of simulation analyses and considering the worst scenario for each type of power quality disturbances, the best threshold values for each scenario under 30 dB WGN were chosen and the results are shown in Table 3.1.

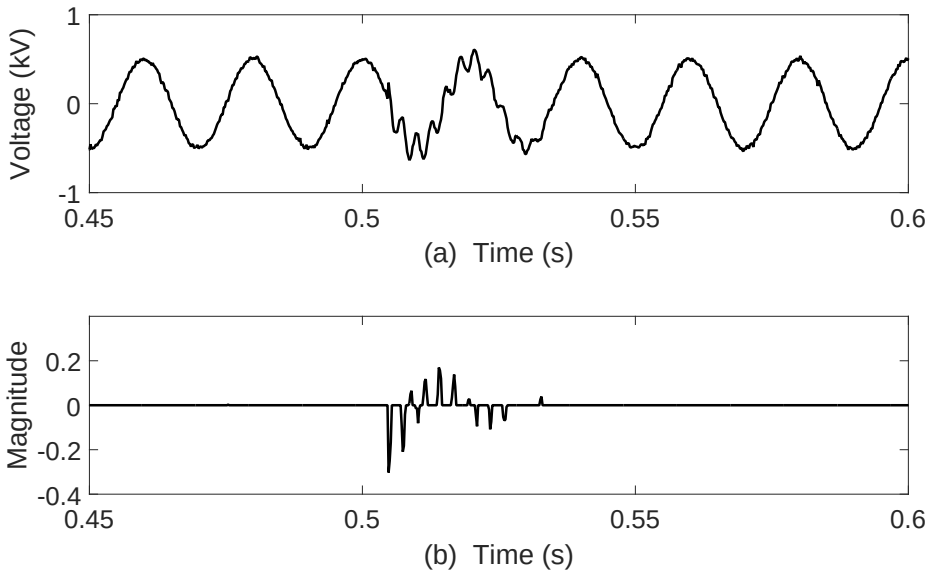

Figure 3.9: Analysis results for the case of damped oscillatory transients (35 dB WGN): (a) fundamental signal with a damped oscillatory transient; (b) result of MMG for detection of the damped oscillatory transients.

Table 3.1: Selection of best threshold vaules for different power quality disturbances under 30 dB WGN

Power Quality Disturbances	SNR (dB)	Best Threshold Value g_2
Voltage Sag	30	0.42
Momentary Interruption	30	0.43
Voltage Swell	30	0.40
Periodic Notch	30	0.41
Oscillatory Transients	30	0.41

However, when the SNR of WGN decreases, which means an increase in noise in signals, the best threshold values for each case need to increase correspondingly in order to maintain the performance of the MMG algorithm. Therefore, it indicates that noise has a great impact on the performance of MMG.

The simulation results on the accuracy of detecting power quality disturbances using MMG with the selection of best threshold value for each case are illustrates in Table 3.2. The precise times without any error has been achieved

Table 3.2: Simulation results on accuracy of detection of power quality disturbances using MMG

Disturbances	Voltage Sag		M. Interruption		Voltage Swell		O. Transient	
	begin	end	begin	end	begin	end	begin	end
Actual position (s)	0.4946	0.4956	0.4928	0.5460	0.4848	0.5136	0.5042	0.5342
Result (s)	0.4948	0.4958	0.4926	0.5456	0.4848	0.5136	0.5042	0.5346
|Error| (s)	0.002	0.002	0.002	0.004	0	0	0	0.004

for the voltage swell disturbance. For detection damped oscillatory transient, there is no error in the starting location, but a slight error of 0.004 second for the end point. For voltage sag and momentary interruption disturbances, an average error of 0.0025 second arises for detecting the start and end points. The overall results reveal that this proposed method only has an average error of 0.00175 second for detection of these disturbances in noisy environments which means that a detection accuracy of more than 90% has been achieved. However, when the disturbance occurs close to the zero-crossing point between positive peak and negative peak, the proposed method sometimes may not be able to extract the feature of the disturbance or the extracted characteristic is too small to be identified. In these circumstance, MMG is ineffective and this will also result in the failure of power quality disturbances classification.

3.3 Classification of Power Quality Disturbances

After detecting the existence of these disturbances and extracting their features, the classification of these detected disturbances is necessary for further analysis. Although MMG is able to determine the location of power quality disturbances in the signal, it is difficult for computers to estimate and recognise the type of the disturbance. Therefore, another simple MM operator, *closing*, is applied combining with MMG to classify the disturbances by obtaining the signal envelope as another criterion. To be clearer, the "signal envelope" represents the undulated change in amplitude of the target signal.

The *closing* operator is defined as:

$$f_{\text{envenlope}} = ((S \oplus G) \ominus G), \tag{3.3.1}$$

where S is the target signal and G is a flat SE with zero degree.

All elements in the SE are one and the length of the SE is the same as the number of samples in one cycle of the fundamental frequency component (100 samples and 0.02 second in this scenario). Therefore, the *closing* operator can remove the signal component that has a period less than 0.02 second. Since the period of the objective signal is less than 0.02 second, f_{envelope} only contains the peak values of the signal which is regarded as the envelope and the change in signal amplitude can be obtained. In this improved method, MMG with trapezoid SEs, extracting features, and *closing* operator, producing signal envelopes, are combined to estimate the types of power quality disturbances in the signals.

3.3.1 Voltage Sag

According to Fig. 3.10, the amplitude of the signal envelope remains constant during the voltage sag since this disturbance does not lead to amplitude change. MMG detects the occurrence of the voltage sag, where the value changes from zero which produces an impulse in the extracted signal. Consequently, the type of the disturbance can be recognised from the extracted feature and the constant signal envelope.

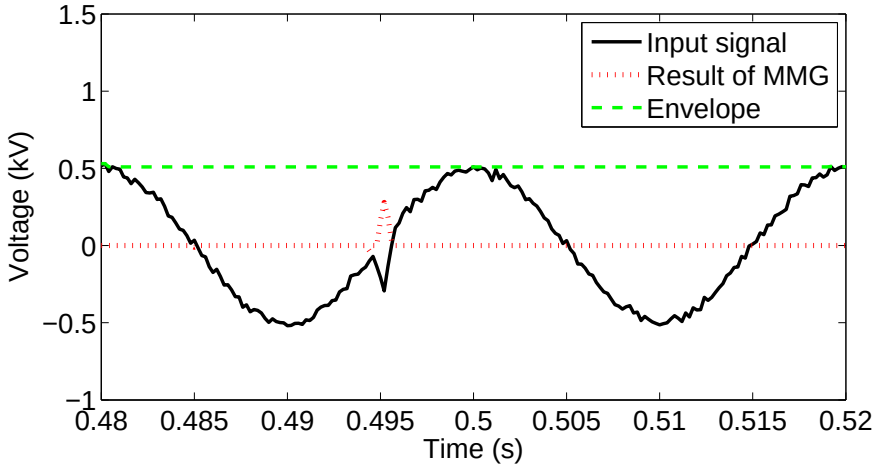

Figure 3.10: The simulation result for a voltage sag.

3.3.2 Momentary Interruption

The simulation result for a momentary interruption is shown in Fig. 3.11. The amplitude of the envelope reduces to almost zero when the momentary interruption is about to start and it recovers to its initial amplitude right after the interruption ends. Meanwhile, the start and the end of the interruption have also been estimated by MMG. Hence, for classifying momentary interruption, the value of the extracted feature changes at both the start and end locations and the amplitude of the signal envelope reduces to zero during this period.

3.3.3 Voltage Swell

Fig. 3.12 presents the simulation result of voltage swell. The typical characteristic of voltage swell is that the amplitude of the voltage increases temporarily for a duration. Similarly, the magnitude of the signal envelope increases for a same period when voltage swell occurs. Furthermore, the start and end points of the swell, which are presented as two impulses in the extracted signal, are detected by MMG. With these two features, voltage swell is clearly identified.

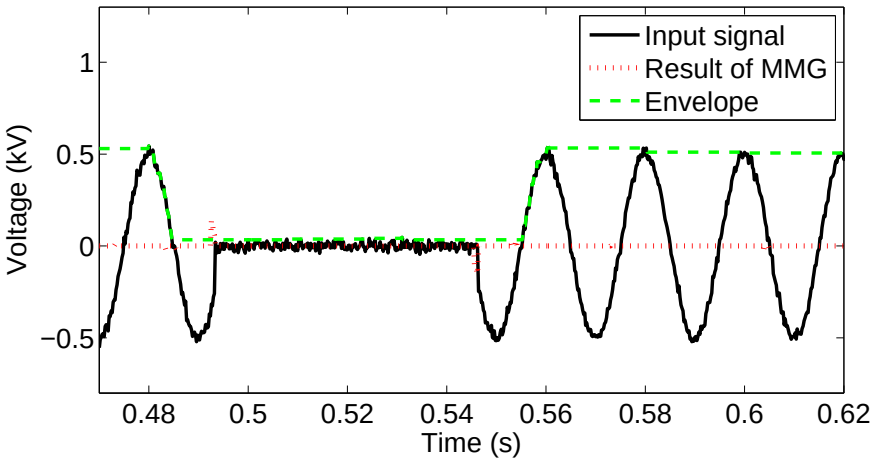

Figure 3.11: The simulation result for a momentary interruption.

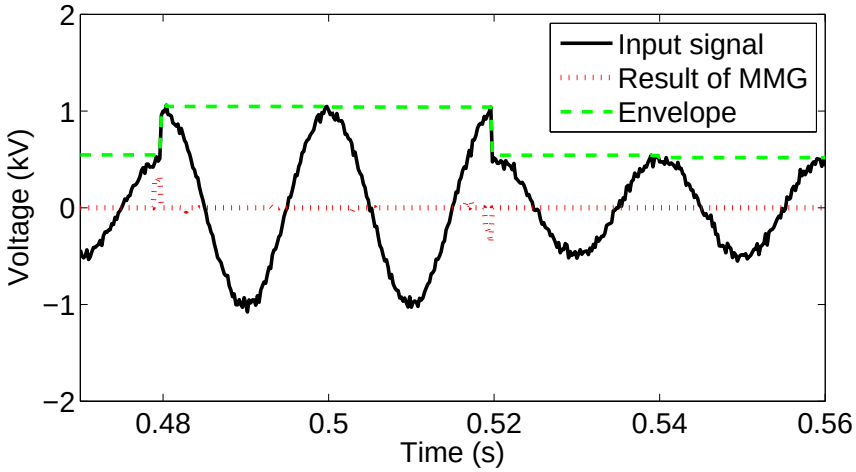

Figure 3.12: The simulation result for a voltage swell.

3.3.4 Oscillatory Transient

In Fig. 3.13, the simulation result of damped oscillatory transient is presented. The damped oscillatory transient is easy to identify as the result of MMG changes synchronously with the transient. Meanwhile, the amplitude of the signal envelope increases during the period of the disturbance as well. With the synchronous fluctuation extracted signal and ascending signal envelope, the damped oscillatory transient is successfully recognised.

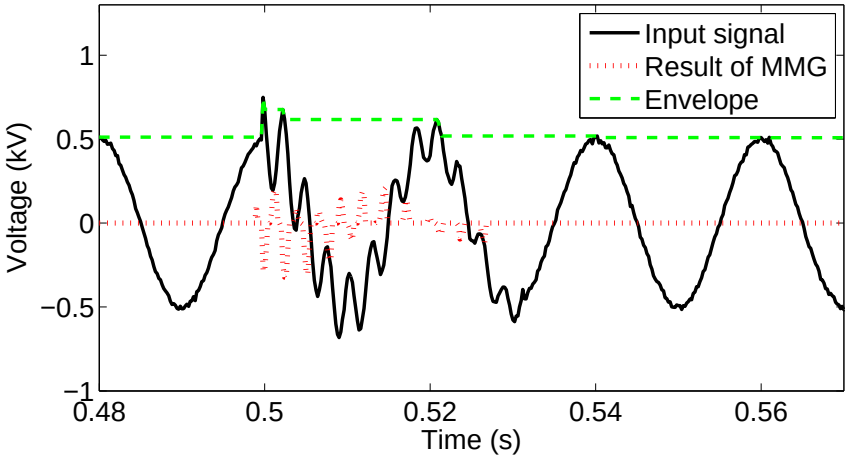

Figure 3.13: The simulation result for damped oscillatory transients.

Based on the features analysed above, the power quality disturbances can be classified according to the principles shown in Table 3.3. The feature ex-

Table 3.3: Classification methods of power quality disturbances

Disturbances	MMG	Envelope
Voltage Sag	value changed	constant
Momentary Interruption	value changed at start and end	zero
Voltage Swell	value changed at start and end	increased
Oscillatory Transient	value changed frequently from start to end	increased

tracted using MMG and the signal envelope of the input signal obtained by

the *closing* operator can be applied jointly for power disturbance classification. Furthermore, as mentioned in the previous section, MMG might be ineffective when the disturbance occurs around the zero-crossing points. Therefore, without the accurate power disturbance feature extraction, the classification fails. If the classification or the detection of a disturbance fails (extracted feature does not match with the descriptions in the table), this disturbance would be considered not to be accorded with the descriptions of typical power quality phenomena described in IEEE 1159 standard [44].

3.4 Conclusions

In this chapter, a recently developed MT, MMG algorithm, has been improved by using trapezoid SEs. MMG is applied to detect the location of several typical power quality disturbances. The extracted features can be used combining with a morphological operator, *closing*, generating signal envelopes to classify the types of the detected disturbances.

The simulation studies of the extraction on different typical power quality disturbances, containing voltage sag, momentary interruption, voltage swell and damped oscillatory transient, have demonstrated that the proposed approach is able to detect different types of power quality disturbances effectively and successfully in most cases. Moreover, the adoption of the morphological operator, *closing*, has been applied to obtain a signal envelope of the input signal and this amplitude information can be combined with the extracted signal for accurately classifying the types of the detected disturbances. Although in some severe situations, MMG fails to extract the features of these disturbances, the performance of the refined MMG in detection of power quality disturbances in noisy environments is still considerable to a large extent compared to other techniques. Furthermore, the proposed method is simple and easy to implemented. Through large amount of simulations, in an SNR of 30 dB environment, the proposed approach can reach above 90% accuracy in the identification of typical power quality disturbances.

Chapter 4

Detection of Low Frequency Oscillations

There exist Low frequency oscillations (LFO) in power systems with long distance and large capacity power stations, and severe power quality issues can be caused by weak interconnection, degrading the stability of power systems. With increasing amount of large-scale power systems, some of power system blackouts incidents related to LFO have occurred frequently in the past few years. Hence, in order to improve the dynamic stability, effective and accurate detection of LFO becomes more necessary in large-scale power systems.

This chapter firstly introduces a hybrid method, using an envelope extraction morphological filter (MF) and group search optimiser (GSO) technique, for detecting continuous LFO in power systems. This proposed approach focuses on accurately extracting envelopes of the target signal by applying the MF based on two basic morphological operators, $dilation - closing$ and $erosion - opening$ and estimating the parameters of the extracted envelopes by using GSO. This algorithm is capable of on-line detecting continuous LFO components in severely noisy environments, which are mainly resulted from the imperfections of the generators caused by slight vibrations and impacts in the generators, and it can also provide the parameters for further analysis on LFO. However, the hybrid method using the GSO has not be applied

for detecting damped LFO since the computational time consumption increases dramatically when applying GSO to calculate the parameters of the damp ones. As a consequence, inspired by the idea of handling LFO directly from a new angle, another pre-designed MF is utilised to directly deal with damped LFO components, which are generally caused by sudden faults occurring in transmission lines or interconnected area in large-scale power systems. In this LFO extraction MF, another two morphological operators, *opening* − *closing* and *closing* − *opening*, are applied to directly extract the damped LFO components. In order to analyse these approaches, a generator fault system model and a four-machine two-area power system model are simulated to generate signals containing continuous and damped LFO components separately. Several simulation tests have been undertaken to assess the efficiency of these proposed methods. The simulation studies demonstrate that both proposed techniques are robust on detecting the presence of continuous and damped LFO respectively in large complex power grids.

4.1 Envelope Extraction Morphological Filter with GSO for Detecting Continuous LFO

In this section, envelope extraction MF is introduced firstly and the GSO algorithm is then described.

4.1.1 Envelope Extraction Morphological Filter

Let S and G denote the input set and structuring element (SE), respectively. The two basic operators of MM, *dilation* and *erosion* can be defined as follows:

$$\delta_G(S) = S \oplus G = \bigcup_{g \in G} (S + g), \tag{4.1.1}$$

$$\varepsilon_G(S) = S \ominus G = \bigcap_{g \in G} (S - g). \tag{4.1.2}$$

By combining *dilation* and *erosion*, another two popular operators *opening* and *closing* are generated as:

- *Opening*

$$S \circ G = (S \ominus G) \oplus G, \tag{4.1.3}$$

- *Closing*

$$S \bullet G = (S \oplus G) \ominus G. \tag{4.1.4}$$

In order to extract the upper and lower envelopes of the target signal, these operators, called $dilation - closing$ and $erosion - opening$, are combined and given as:

$$f_{\text{ue}} = (S \oplus G) \bullet G, \tag{4.1.5}$$

$$f_{\text{le}} = (S \ominus G) \circ G, \tag{4.1.6}$$

where f_{ue} presents the function for extracting upper envelopes and f_{le} represents that for extracting lower envelopes.

In this process, S is formed as a matrix containing the input signal information and G is a pre-defined matrix. The process is operated by the interaction between S and G. G moves through S and the calculation at each sample point is processed. The main function of the method is to extract relevant structures of the input set. As previously explained, both types of LFO normally result in the slight shape change of the envelope of the target signal. As a consequence, the proposed MF, which can remove all the detail waveforms whose width are shorter than the length of the SE, can be applied to extract the change in the envelope of the target signal. Once the envelopes that contain the information of continuous LFO are obtained, the following GSO can be utilised to estimate the parameters and reconstruct the LFO component.

In this application, the SE is selected as a flat line with its origin at the centre. Furthermore, in order to extract the envelope, the waveform of the fundamental frequency component should be removed from the input signal. Since the LFO changes much slower than the fundamental frequency component, the length of the SE is designed to be half a fundamental cycle of the input signal. For instance, for an input signal with a fundamental frequency of 50 Hz, the window length of the SE should be 10 ms and this is applied to

all the cases presented in the simulation studies. In this manner, the fundamental frequency component and the noise are all eliminated from the input signal, and the output of the MF is the envelope containing the parameters for reconstruction of the LFO signal. Therefore the proposed MF can be regarded as an envelope extraction MF.

An example is presented in Fig. 4.1. It is obvious that the upper and lower envelopes are extracted successfully by using the envelope extraction MF.

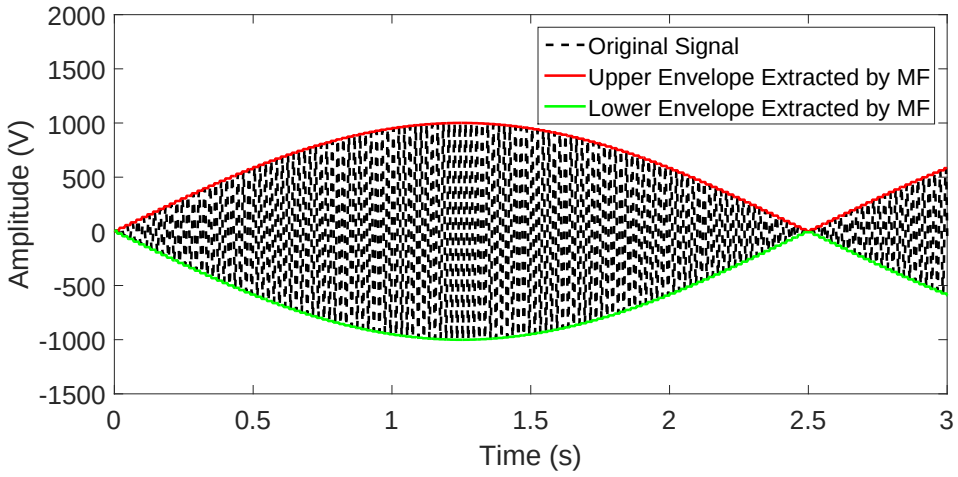

Figure 4.1: An example of extraction of envelopes using the envelope extraction MF.

According to Eqn. (4.1.5) and Eqn. (4.1.6), the overall envelope is expressed as:

$$o(t) = f_{\text{ue}} + f_{\text{le}}, \tag{4.1.7}$$

where $o(t)$ is the output of the envelope extraction MF.

4.1.2 Group Search Optimiser

The extracted envelope is then applied through GSO. GSO is an optimisation algorithm developed based on population[86]. Inspired by animal behaviour, especially animal searching behaviour, GSO was proposed. The population of the GSO algorithm is called a *group* and each individual in the

population is regarded as a *member*. According to the Producer-Scrounger (PS) model, a group contains three different members:

- Producer is the leader of the group, who searches food and shares information with the residual of the group. In each iteration, the producer is selected from the best member of the group according to the fitness values of the objective function.
- Scroungers follow the producer and examine resources uncovered by other scroungers. Except the producer, 80% of the remaining members in the group are randomly selected as the scroungers.
- The residual members are regarded as rangers and they walk randomly in the searching space.

The PS model was simplified by assuming that there is only one producer at each searching bout (iteration) and the remaining members are scroungers and dispersed members. Moreover, the simplest joining policy, which considers all scroungers will join the resource found by the producer, is also applied. For optimising problems, unknown optima can be regarded as open patches randomly distributed in the search space. As a consequence, members search for these patches by moving over the search space and the producer and the scroungers can switch to each other since they do not differ in their relevant phenotypic characteristics [86].

4.1.3 Producer

In an n-dimensional searching space, the i^{th} member at the k^{th} iteration, has a current position $\boldsymbol{x}_i^k \in \mathbb{R}^n$, a head angle $\varphi_i^k = (\varphi_{i1}^k, \cdots, \varphi_{i(n-1)})^k \in \mathbb{R}^{n-1}$, and a head direction $D_i^k(\varphi_i^k) = (d_{i1}^k, \cdots, d_{in})^k \in \mathbb{R}^n$, which can be calculated from φ_i^k via a Polar to Cartesian coordinates transformation:

$$d_{i_1}^k \quad = \quad \prod_{q=1}^{n-1} \cos(\varphi_{i_q}^k),$$

$$\begin{aligned} d_{i_j}^k &= \sin(\varphi_{i_{(j-1)}}^k) \cdot \prod_{q=j}^{n-1} \cos(\varphi_{i_q}^k), \qquad (j = 2, \cdots, n-1) \\ d_{i_n}^k &= \sin(\varphi_{i_{(n-1)}}^k). \end{aligned} \tag{4.1.8}$$

Meanwhile, each member has a fitness value $F(\boldsymbol{x}_i^k)$.

The scanning field of a producer in the n-dimensional space can be characterised by a maximum scout angle $_{\max} \in \mathbb{R}^{n-1}$ and a maximum pursuit distance $l_{\max} \in \mathbb{R}^1$. In GSO, at the k^{th} iteration, the producer has the best fitness value $F(\boldsymbol{x}_p^k)$. The searching behaviour of the producer $\boldsymbol{x}_p^k$ is obtained through the procedure that it selects three positions from the scanning field. The first position is at zero degree and its distance from the current position is randomly chosen as:

$$\boldsymbol{x}_z = \boldsymbol{x}_p^k + r_l l\max \boldsymbol{D}_p^k(\boldsymbol{\varphi}^k). \tag{4.1.9}$$

The second position is randomly picked in the right hand side hypercube of the producer, presented as:

$$\boldsymbol{x}_r = \boldsymbol{x}_p^k + r_1 l_{\max} \boldsymbol{D}_p^k(\boldsymbol{\varphi}^k + \boldsymbol{r}_2 \theta_{\max}/2). \tag{4.1.10}$$

While the third position is randomly chosen from its left hand side hypercube, shown as:

$$\boldsymbol{x}_l = \boldsymbol{x}_p^k + r_1 l_{\max} \boldsymbol{D}_p^k(\boldsymbol{\varphi}^k - \boldsymbol{r}_2 \theta_{\max}/2), \tag{4.1.11}$$

where $\theta_{\max} \in \mathbb{R}^1, l_{\max} \in \mathbb{R}^1$ are the maximum pursuit angle and the maximum pursuit distance, respectively. $\boldsymbol{x}_p^k$ is the producer $\boldsymbol{x}_p$ at the kth iteration. $r_1 \in \mathbb{R}^1$ is a normally distributed random number with mean of zero and the standard derivation 1 and $\boldsymbol{r}_2 \in \mathbb{R}^{n-1}$ is a uniformly distributed random sequence in the range (0,1).

If a better area has not been discovered by the producer after a iterations, it will turn its head back to zero degree, set as:

$$\boldsymbol{\varphi}^{k+a} = \boldsymbol{\varphi}^k, \tag{4.1.12}$$

where $a \in \mathbb{R}^1$ is a constant.

4.1.4 Scroungers and Rangers

Each scrounger moves towards the producer and searches the area around the producer. The behaviour of the i^{th} scrounger can be expressed as:

$$\boldsymbol{x}_i^{k+1} = \boldsymbol{x}_i^k + r_3(\boldsymbol{x}_p^k - \boldsymbol{x}_i^k), \tag{4.1.13}$$

where r_3 is uniform random sequences in the range of (0,1).

If the i^{th} member is selected as a ranger at the k^{th} iteration, the ranger generates a random head angle φ_i^{k+1}, presented as:

$$\boldsymbol{\varphi}_i^{k+1} = \boldsymbol{\varphi}_i^k + \boldsymbol{r}_2\alpha_{\max}, \tag{4.1.14}$$

where $\alpha_{\max}$ is the maximal tuning angle. The ranger also selects a random distance:

$$l_i = b \cdot r_1 l_{\max}, \tag{4.1.15}$$

where b is a coefficient that addresses the proportion between the speed and dimensionality of the ranger. Hence, the ranger moves to the new position as follows:

$$\boldsymbol{x}_i^{k+1} = \boldsymbol{x}_i^k + l_i \boldsymbol{D}_i^k(\boldsymbol{\varphi}_i^{k+1}). \tag{4.1.16}$$

In this research, GSO uses the extracted envelopes as the source signal and aims to estimate the parameters of the LFO. Thus, the objective function of the i^{th} member, $F(x_i)$, is defined as:

$$F(x_i) = \sum_{l=1}^{N_s} |o_i - \bar{o}_i|, \tag{4.1.17}$$

where N_s is the number of samples in a window of the extracted envelope signal, o_i is the i^{th} sample of the extracted envelopes by using the MF, and $\bar{o}_i$ is the reconstructed envelope generated by applying the GSO. $\bar{o}_i$ is expressed as:

$$\bar{o}_i = x_{i1}\sin(x_{i2}t_l + x_{i3}), \tag{4.1.18}$$

where t_l is the time at the l^{th} sample. The pseudo code of GSO is shown in Table 4.1.

Table 4.1: Pseudocode for the GSO algorithm

Set $Iter := 0$; Population size:=$PopSize$;
Maximum number of function evaluations:=$MaxIter$.
Uniformly and randomly initialise each member, $\boldsymbol{x}_i$, in the group;
Calculate the fitness values of initial members: $F(\boldsymbol{x}_i)$;
Find the index of the best member, denote as *index*

While $Iter \leq MaxIter$ **do**
  for $i = 1$ to $PopSize$ **do**
    If $i = index$ **then**
      Performing producing using (4.1.8)-(4.1.12)
    else
      If $random > 0.3$ **then**
        Performing scrounger using (4.1.13)-(4.1.15)
      else
        Performing ranger using (4.1.16)
      end if
    end if
  end for
$Iter$=$Iter$+$PopSize$
Calculating the fitness of new group member and updating *index*

As mentioned previously, the envelopes contain the information of the parameters of the LFO. Hence, following the procedure of GSO, this approach applies the GSO to estimate the fittest parameters of the LFO. Once these features are obtained, the LFO component in the input signal can be reconstructed successfully. The flowchart containing the detail procedures of the proposed method is presented in Fig. 4.2.

The proposed method focuses on effectively and accurately online detecting LFO components in power system signals. Besides this, feature values of the LFO components can also be obtained. Furthermore, if enough time is permitted, more accurate reconstruction of LFO can be achieved by increasing the number of iteration in GSO in most cases. Although, other approaches also use known power system data to calculate power system parameters for analysing LFO components and the LFO components are reconstructed referring to the calculated parameters [59, 83, 111], more time is required for processing these methods and large quantity of source data is also necessary. Additionally, in this project, the hybrid scheme has only been applied for detecting continuous

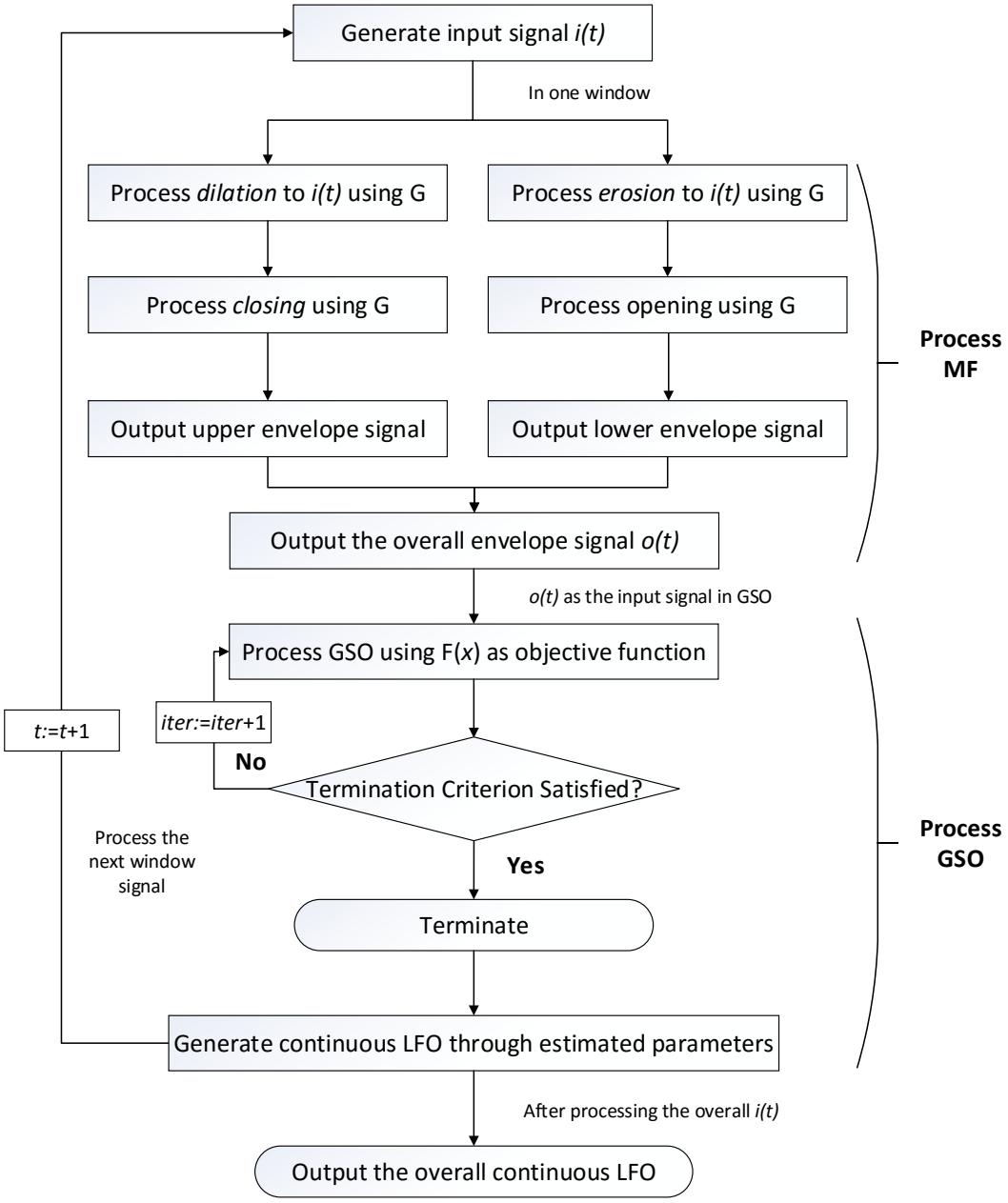

Figure 4.2: Flowchart of the hybrid algorithm using MF and GSO.

LFO components and the concept of this combinational algorithm is similar to the conventional ones since they estimate the feature values of LFO and reconstruct them. Moreover, in detecting damped LFO scenarios, it becomes much more complicated for dealing with damped LFO, which leads to increasing in both computation complexity and time for processing GSO. Therefore, it becomes complex and insignificant for the hybrid scheme of MF and GSO to detect damped LFO, which is also one of its limitations, and it also inspires the idea of using another MF to directly detect damped LFO from a new point of view.

4.2 LFO Extraction Morphological Filter for Detecting Damped LFO

As mentioned previously, it is inefficient for the hybrid scheme based on MF and GSO to detect damped LFO components. Hence, another MF is proposed and the MF designed for extracting damped LFO components utilises $opening - closing$ and $closing - opening$ morphological operators. According to the definitions of *opening* and *closing*, the $opening - closing$ and $closing - opening$ operators are given as:

$$f_{\text{opcl}} = S \circ G \bullet G, \tag{4.2.1}$$

$$f_{\text{clop}} = S \bullet G \circ G. \tag{4.2.2}$$

These two filters can be combined to implement a new MF, which is also the proposed MF, shown as:

$$f_{\text{dlfo}} = \left(f_{\text{opcl}} + f_{\text{clop}}\right)/2, \tag{4.2.3}$$

where f_{dlfo} produced the output signal, $o(t)$. Similarly, for detecting damped LFO components, the SE is also selected as a flat one with its origin at the centre and the length of the SE is still designed to be half a fundamental cycle of the input signal. In this manner, the fundamental frequency component is eliminated from the input signal, and the output signal of the MF is the desired damped LFO component.

4.3 Simulation Studies

In this section, signals containing different types of LFO components generated by two diverse models are applied to demonstrate the performance of the hybrid method with envelope extraction MF and GSO and the LFO extraction MF respectively. All the modelling and simulating are carried out on a Dell PC with 3.4 GHz Intel Core i7-2600 CPU and 8.00 GB RAM using MATLAB 2015a. The signals applied in simulation studies are generated according to the models described below and these synthetic signals can be regarded as real measured signals. In simulation studies, the sampling frequency is 3.2 kHz, which is common sampling frequency value used in equipment in practical situations.

4.3.1 Simulation Models

As introduced in the first section, LFO can be caused by different problems in power systems, which leads to LFO with varying features. Consequently, two models were developed in the simulation studies, a generator fault model to generate signals containing continuous LFO components and a two-area test system model to produce signals with damped ones.

Generator Fault Test System Model

The diagram of the generator fault test system model is presented in Fig. 4.3. IF represents the source of low frequency signals. A load is connected at a bus bar fed by a 50 Hz, 1 kV inductive source. A 6th harmonic (300 Hz, 1 A) current is injected at the bus bar. Due to the imperfections of the generators caused by slight vibrations and impacts in the generators, the continuous LFO component with time-varying frequency and amplitude will appear which are respectively shown as the f_{v} Hz, A_{v} V sources (IF1). Consequently, the continuous LFO signal can be generated by the system. By maintaining the fundamental inductive source and changing the amplitudes and frequencies of the other sources, a couple of different LFO components can be generated.

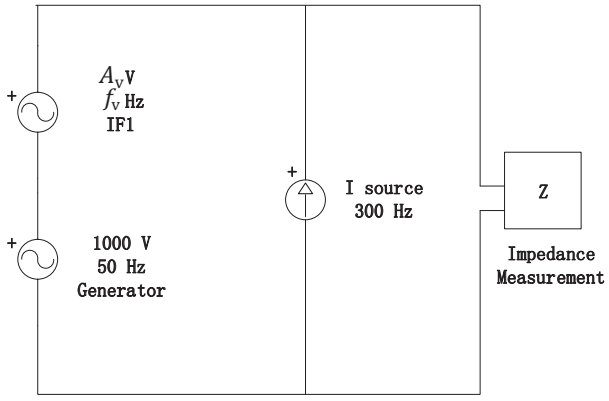

Figure 4.3: Diagram of generator fault test system.

Moreover, by adding more inductive sources, signals containing multiple LFO components can also be generated.

Two Area Test System Model

The schematic diagram of Kundur's four-machine two area test system used in the simulation is shown in Fig. 4.4.

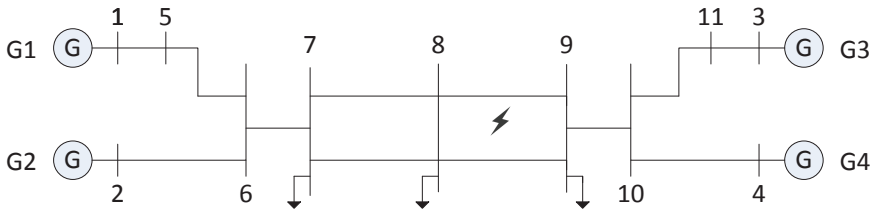

Figure 4.4: Single line diagram of Kundur's four-machine two area test system.

This system is specifically designed in [112, 113] to study LFO in large interconnected power systems. It very closely mimics the behaviour of typical power systems in actual operation which enhances the reliability of the generated signals. The test system consists of two fully symmetrical areas linked together by two 230 kV lines of 220 km length. Each area is equipped with two

20 kV/900 MVA identical rotor generators. As shown in Fig. 4.4, generators G1 and G2 (forming area 1) are oscillating with respect to generators G3 and G4 (forming area 2). The lightning symbol in the middle section indicates that there is a fault arising in the transmission line. This incident results in interconnected-area damped LFO occurring in the power system. The fault type is single-phase ground fault and the fault remains on the transmission line from the first second.

4.3.2 Results For Detecting Continuous LFO

In this scenario, the input signal generated from the generator fault model consists of a basic power frequency of 50 Hz and a continuous LFO signal with time-varying frequency and amplitude f_{v}, which is expressed as:

$$i(t) = A_{\mathrm{v}} \sin(2\pi \cdot f_{\mathrm{v}} \cdot t) \cdot 1000 \sin(2\pi \cdot 50 \cdot t), \tag{4.3.1}$$

where A_{v} varies around 10 V, f_{v} changes between 0 to 2 Hz, the duration of each steady LFO is approximately one second and the input signal from 0 to 200 seconds has been simulated. According to [114, 115, 116], the LFO component is not simply "added" to the fundamental component and the influence of LFO changes the envelope of the input signal. The variations of the frequency and amplitude of the continuous LFO component in $i(t)$ are illustrated in Fig. 4.6.

As previously mentioned, the SE applied in the simulations is a flat line SE with its origin at the centre. The length of the SE is set to be 10 ms which is the half a cycle of the fundamental frequency component of $i(t)$.

After applying the proposed MF with the pre-set SE, the extracted envelopes are processed by using GSO. For example, assuming that the frequency of the continuous LFO is 0.2 Hz, the period of the LFO is 5 seconds. Normally, in order to accurately estimate the parameters of the LFO, two periods of the target signal data are required. Hence, the window length for processing the GSO is set to 10 seconds, which is also the length of the objective function. Since the frequency of the LFO changes between 0 and 2 Hz, a fixed window length of 10 seconds is applied, where this length can be sufficient for estimat-

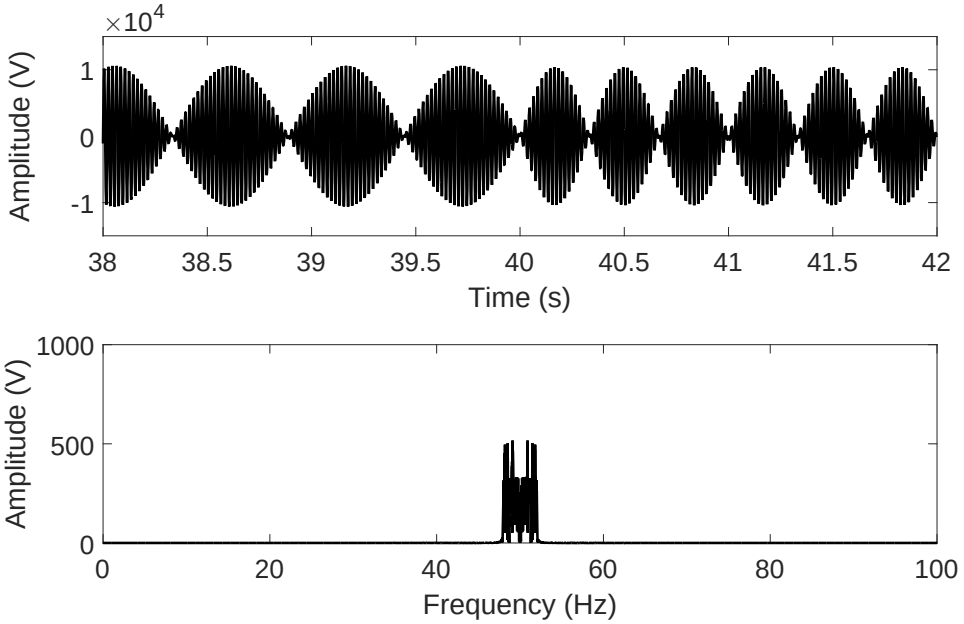

Figure 4.5: The waveform and spectrum of the input signal $i(t)$ with LFO of time-varying frequency and amplitude.

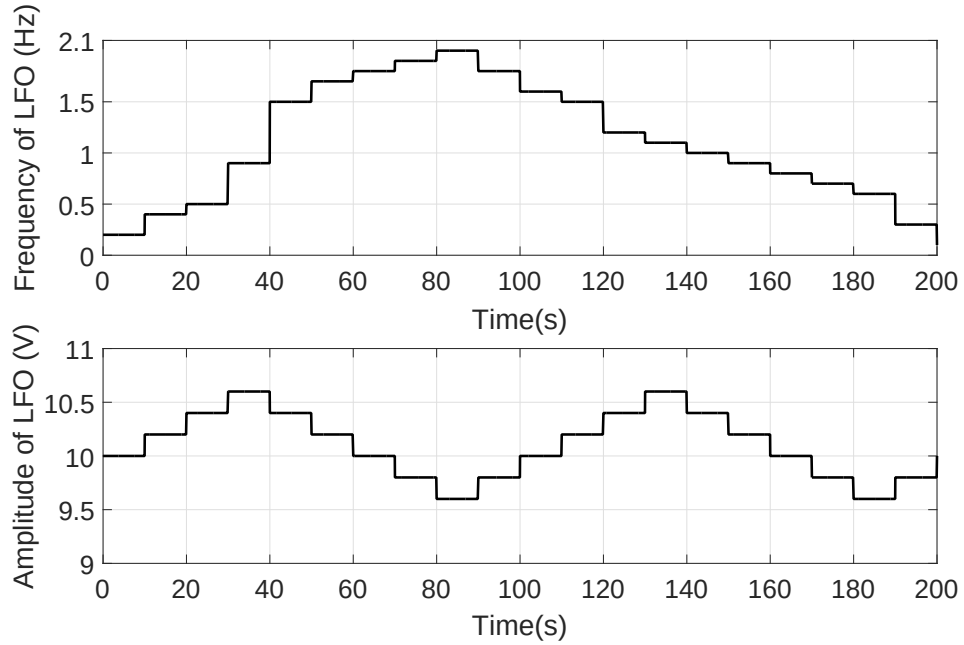

Figure 4.6: The variation of the frequency and amplitude of the LFO.

ing the parameters of LFO with frequency from 0 to 2 Hz using GSO. Under practical circumstances, the window length of GSO is set according to the lowest frequency of the LFO existing in the system. Furthermore, the number of iteration applied in GSO is 2000 in all simulations.

The estimated LFO and the breakdown of the process of this hybrid method using MF and GSO are illustrated in Fig. 4.7. It is obvious that MF firstly

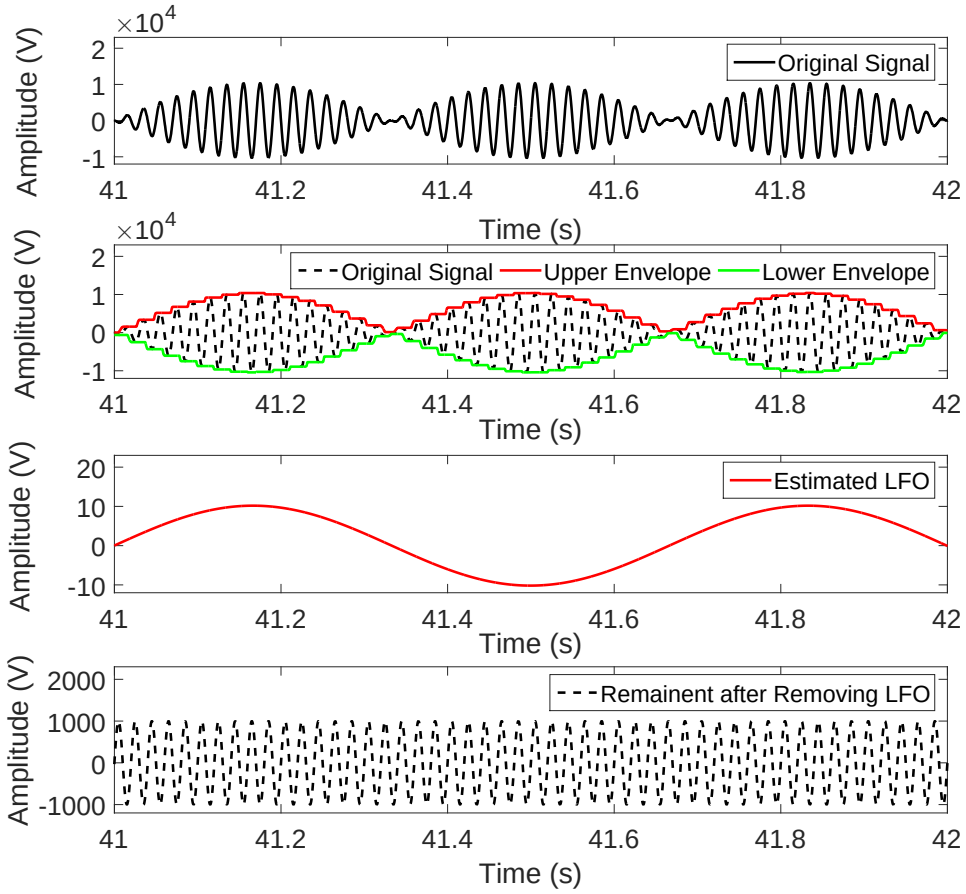

Figure 4.7: Breakdown of individual components in the input signal with LFO of 0.2 Hz using MFGSO.

extracts the upper and lower envelopes from the original sampled signal and the third graph indicates that the estimated LFO component during that period is reconstructed by GSO.

Furthermore, in order to improve the reliability of the results using MF with

GSO, the average results based on 50 simulations have been obtained. Additionally, the frequency and amplitude of the LFO change with time. Hence, according to the average simulation results on detecting the LFO during each period, Fig. 4.8 and Fig. 4.9 summarising the corresponding average curves of the variations of the frequency and amplitude of the estimated LFO are demonstrated respectively and the changes of the frequency and amplitude of the original LFO are also presented as the comparison.

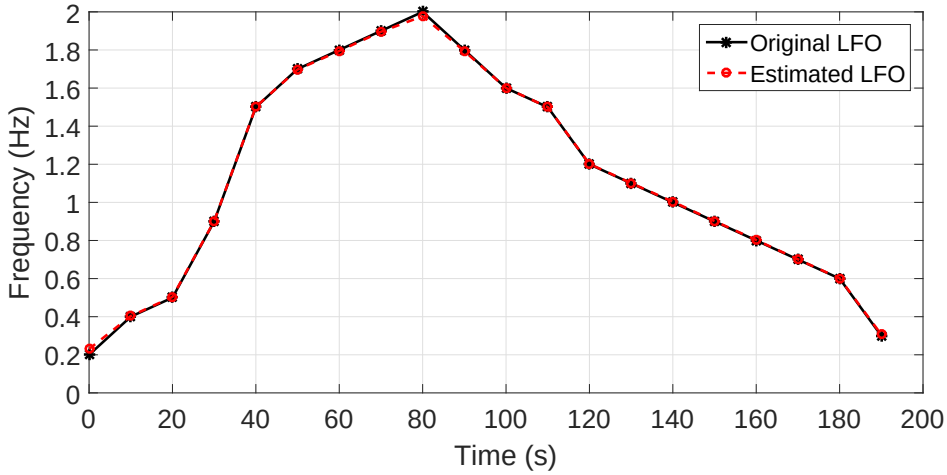

Figure 4.8: The comparison between the variation of the frequency of the original LFO and that of the estimated LFO using MFGSO based on 50 times experiments.

From Fig. 4.8, the frequency change of the reconstructed LFO approximately the same to that of the original LFO, which indicates that the frequency information of the LFO existing in the input signal is obtained successfully. Referring to Fig. 4.9, although the exact value of the amplitude during each period of the estimated LFO is slightly smaller than that of the original LFO, the overall variation trends of them are similar. These results apparently demonstrate that the proposed method using MF and GSO is capable of online detection of LFO due to its accurate estimation of the parameters of the LFO and real-time tracking ability.

In practical situations, noises are existing in large scale power systems.

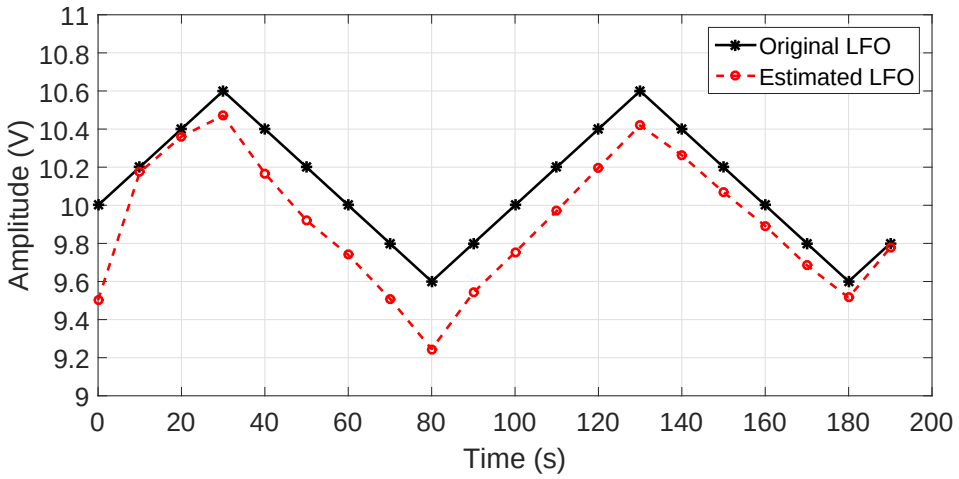

Figure 4.9: The comparison between the variation of the amplitude of the original LFO and that of the estimated LFO using MFGSO based on 50 times experiments.

Therefore, it is necessary to justify the performance of the propose algorithm in noisy environments. Consider the system is polluted by a white Gaussian noise (WGN) with signal-to-noise ratio (SNR) of 30 dB and apply the same input signal in Eqn. (4.3.1). In order to pollute the input signal with WGN, a noise vector is generated randomly, by giving a specified SNR level, such as 30 dB. Then the power of the input signal and the power of the noise vector are calculated. According to these parameters, the amplitude scaling factor for the noise vector is obtained. With these characteristics, the input signal corrupted with WGN of a desired SNR level can be generated.

Considering the noisy environments, average curves of the corresponding frequency and amplitude variation of the estimated LFO are illustrated in Fig. 4.10 and Fig. 4.11, respectively. Similarly, the changes of the frequency and amplitude of the original LFO are compared. Comparing Fig. 4.8 and Fig. 4.10, similar results are obtained with or without the influence of WGN, which indicates that the estimation of the frequency of the LFO using the proposed algorithm is not affected by noise. While according to Fig. 4.9 and Fig. 4.11, the amplitude estimation of the LFO is influenced to some extent since the

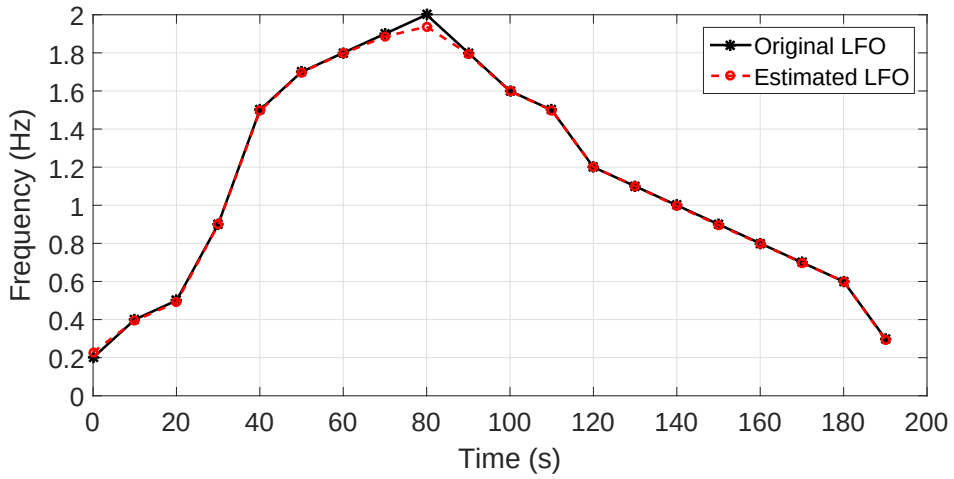

Figure 4.10: The comparison between the variation of the frequency of the original LFO and that of the estimated LFO using MFGSO considering 30 dB WGN based on 50 times experiments.

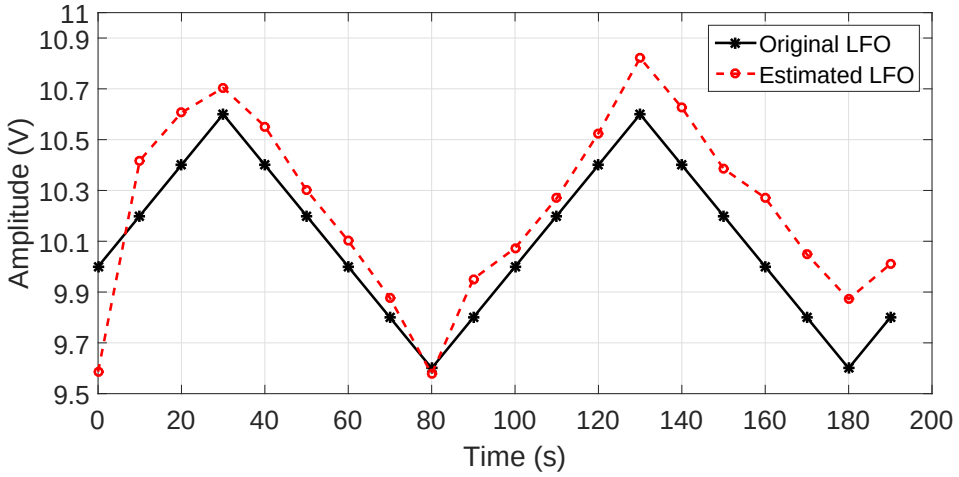

Figure 4.11: The comparison between the variation of the amplitude of the original LFO and that of the estimated LFO using MFGSO considering 30 dB WGN based on 50 times experiments.

noise will result in the increase and decrease of the amplitude of the signal. Besides this, the trend of the variation in amplitude of the reconstructed LFO is similar to the that of the original LFO.

The relative outcomes on the mean values, standard deviations and errors of the frequency and amplitude of the estimated LFO during each time period from 0 to 200 seconds are given in Tab. 4.2. In Tab. 4.2, μ_ω represents the average frequency value of the estimated LFO during each period by using the proposed method and δ_ω and e_ω stands for the corresponding standard deviation and error of the estimated frequency, respectively. Similarly, μ_A, δ_A and e_A presents the amplitude of the estimated LFO during each period, standard deviation and error of the estimated amplitude, respectively. According to the simulation results based on 50 times experiments, it can be conclude that estimated frequency of the reconstructed LFO is approximately matched to the original one since an average error of 0.0050 have been achieved. Moreover, the average standard deviation of the results based on 50 times simulations is 0.0204 which indicates the stability of the proposed algorithm. The estimated amplitude has obtained similar outcomes, where the average error is 0.1289 with the average standard deviation of 0.0462. Although the average error of the estimated amplitude is larger than that of the estimated frequency, these outcomes are still considerable.

In order to discover the ability of the proposed method in a more severe environment, the input signal is polluted with 20 dB WGN, and the corresponding simulation results are concluded in Fig .4.12 and Fig.4.13. The variation curve of the estimated frequency of the LFO is similar to that of the original one according to Fig. 4.12, while the estimated amplitude is not matched with the original one. The concrete data is included in Tab. 4.3. Referring to Tab. 4.3, similar estimated frequency values have been obtained when increasing the SNR value of the WGN and an average error of 0.0201 has been achieved, which implies that the estimation on frequency of the LFO is not affected by the influence of noise when applying the proposed approach. In addition, the average standard deviation of 0.0070 has also proved the sta-

Table 4.2: Original values, Estimated average values (μ), standard deviations (δ) and errors (e) of the frequency and amplitude of the estimated LFO under 30 dB WGN based on 50 times experiments

Time (s)	0	10	20	30	40	50	60	70	80	90
Original Frequency (Hz)	0.20	0.40	0.50	0.90	1.50	1.70	1.80	1.90	2.00	1.80
μ_ω (Hz)	0.228	0.394	0.491	0.898	1.495	1.698	1.796	1.890	1.938	1.794
δ_ω	0.0341	0.0068	0.0044	0.0053	0.0057	0.0044	0.0079	0.0137	0.2660	0.0138
e_ω	0.0281	-0.0058	-0.0095	-0.0017	-0.0050	-0.0020	-0.0032	-0.0145	-0.0624	-0.0058
Original Amplitude (V)	10.00	10.20	10.40	10.60	10.40	10.20	10.00	9.80	9.60	9.80
μ_A (V)	9.586	10.418	10.606	10.704	10.552	10.301	10.102	9.877	9.579	9.952
δ_A	0.4674	0.0607	0.0476	0.0217	0.0214	0.0033	0.0057	0.0029	0.1174	0.0158
e_A	-0.4137	0.2177	0.2062	0.1040	0.1521	0.1010	0.1019	0.0769	-0.0222	0.1515
Time (s)	100	110	120	130	140	150	160	170	180	190
Original Frequency (Hz)	1.60	1.50	1.20	1.10	1.00	0.90	0.80	0.70	0.60	0.30
μ_ω (Hz)	1.599	1.498	1.201	1.100	0.996	0.896	0.798	0.698	0.601	0.295
δ_ω	0.0039	0.0047	0.0042	0.0017	0.0015	0.0054	0.0036	0.0038	0.0074	0.0096
e_ω	-0.0015	-0.0019	0.0007	0.0003	-0.0040	-0.0038	-0.0021	-0.0018	0.0005	-0.0051
Original Amplitude (V)	10.00	10.20	10.40	10.60	10.40	10.20	10.00	9.80	9.60	9.80
μ_A (V)	10.073	10.270	10.525	10.822	10.626	10.386	10.271	10.049	9.872	10.010
δ_A	0.0103	0.0149	0.0056	0.0053	0.0076	0.0228	0.0084	0.0052	0.0316	0.0221
e_A	0.0729	0.0695	0.1254	0.2217	0.2264	0.1856	0.2705	0.2486	0.2716	0.2101

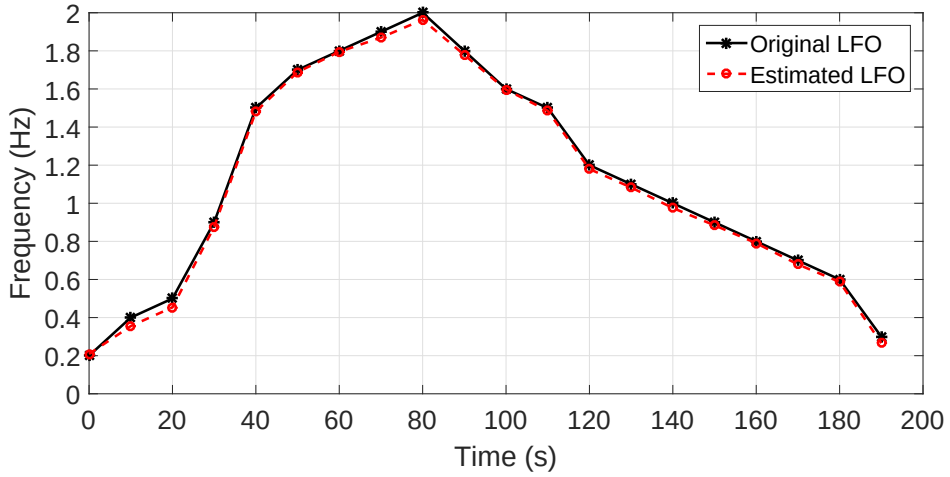

Figure 4.12: The comparison between the variation of the frequency of the original LFO and that of the estimated LFO using MFGSO considering 20 dB WGN based on 50 times experiments.

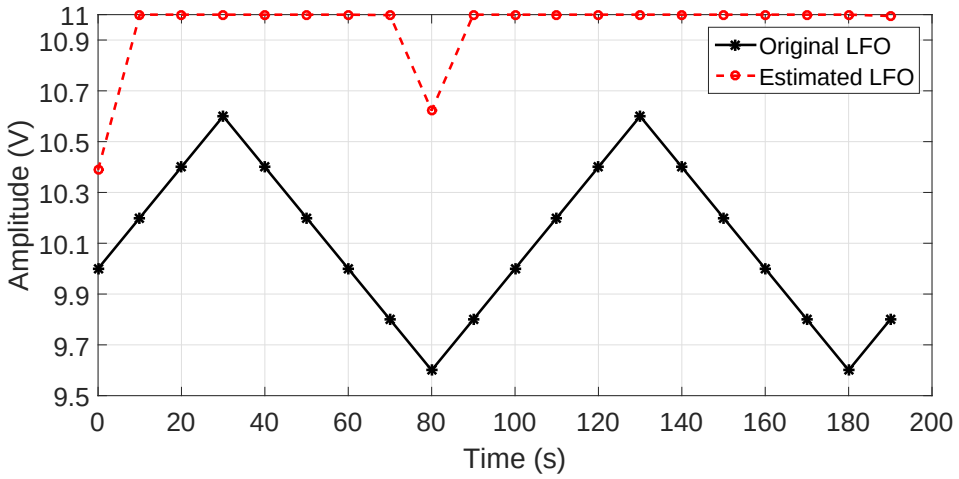

Figure 4.13: The comparison between the variation of the amplitude of the original LFO and that of the estimated LFO using MFGSO considering 20 dB WGN based on 50 times experiments.

Table 4.3: Original values, estimated average values (μ), standard deviations (δ) and errors (e) of the frequency and amplitude of the estimated LFO under 20 dB WGN based on 50 times experiments

Time (s)	0	10	20	30	40	50	60	70	80	90
Original Frequency (Hz)	0.20	0.40	0.50	0.90	1.50	1.70	1.80	1.90	2.00	1.80
μ_ω (Hz)	0.209	0.355	0.454	0.876	1.482	1.689	1.795	1.870	1.963	1.779
δ_ω	0.0223	0.0020	0.0031	0.0033	0.0044	0.0077	0.0062	0.0131	0.0266	0.0092
e_ω	0.0090	-0.0446	-0.0463	-0.0237	-0.0184	-0.0115	-0.0050	-0.0303	-0.0369	-0.0214
Original Amplitude (V)	10.00	10.20	10.40	10.60	10.40	10.20	10.00	9.80	9.60	9.80
μ_A (V)	10.389	10.999	10.998	10.999	10.999	10.998	10.623	10.999	10.998	10.999
δ_A	0.3860	0.0001	0.0001	0.0001	0.0001	0.0001	0.0002	0.0088	0.0998	0.0002
e_A	0.3886	0.8000	0.5999	0.3999	0.5998	0.7999	0.9999	1.1979	1.0227	1.1999
Time (s)	100	110	120	130	140	150	160	170	180	190
Original Frequency (Hz)	1.60	1.50	1.20	1.10	1.00	0.90	0.80	0.70	0.60	0.30
μ_ω (Hz)	1.597	1.485	1.180	1.083	0.975	0.884	0.791	0.679	0.587	0.266
δ_ω	0.0077	0.0047	0.0038	0.0021	0.0047	0.0009	0.0026	0.0039	0.0053	0.0068
e_ω	-0.0034	-0.0147	-0.0204	-0.0171	-0.0248	-0.0158	-0.0094	-0.0209	0.0129	-0.0340
Original Amplitude (V)	10.00	10.20	10.40	10.60	10.40	10.20	10.00	9.80	9.60	9.80
μ_A (V)	10.999	10.999	10.999	10.999	10.999	10.999	10.999	10.999	10.999	10.995
δ_A	0.0003	0.0001	0.0001	0.0001	0.0001	0.0001	0.0001	0.0003	0.0002	0.0152
e_A	0.9998	0.7999	0.5999	0.3999	0.5999	0.7999	0.9999	1.1999	1.3999	1.1946

bility of the hybrid algorithm. However, for the estimation of the amplitude of the LFO, the average error increases to 0.8501 with the standard deviation of 0.0256, since the noise has large impact on the amplitude estimation. The waveforms of the envelopes extracted by using the MF is largely affected by the noise. In the process of estimating the amplitude of the LFO, the influenced envelopes lead to the increase of the estimation error, especially at the zero crossing points. Furthermore, since the LFO is multiplied to the fundamental frequency component in the input signal, the effect of the noise affects the amplitude estimation to a large extent. Nevertheless, the error in evaluating the amplitude of the LFO has been controlled to less than 10% in severely noisy circumstance by applying the MF with GSO.

According to these results, this hybrid method is able to online detect continuous LFO successfully and efficiently even in noisy environments. The same SE was used for all simulation studies and the results demonstrate that the envelope extraction MF can be applied to successfully and accurately detect and extract any LFO components existing in the signal. Furthermore, since the calculations in the MF include only additions and subtractions without any multiplication or division, the proposed approach also has an advantage in decreasing the computation complexity. Moreover, for processing each sampling point, only six addition operators and zero multiplication operator are applied in MF. For the reconstruction of the LFO from the extracted envelopes using GSO, only 10 seconds of the input data are required to estimate the parameters of the LFO, which is considerable and reasonable. Additionally, since the input signal consists of 50 Hz fundamental frequency component and continuous LFO with time-varying frequency and amplitude lasting from 0 to 200 seconds, the results based on 50 times experiments obviously indicate the capability of the proposed method for online detection on LFO even considering the interference of severely noisy environments, which further implies that the algorithm using MF and GSO has high noise-resistance to a large extent. As mentioned previously, the application of this hybrid method has been limited to the detection of continuous LFO since more computational time is required

to process GSO for damped LFO detection. Hence, it has inspired the idea to deal with damped LFO from a new angle and the corresponding results are presented in the following section.

4.3.3 Results For Detecting Damped LFO

In this scenario, the input signal is generated using the two-area four machine model and the LFO extraction MF is applied. The amplitude of the fundamental frequency signal of 50 Hz is 10 kV and the oscillation occurs approximately at 1 second and remains on the transmission line for more than 20 seconds.

The waveform and spectrum of the generated input signal are shown in Fig. 4.14. As can be seen from Fig. 4.14, the damped LFO component also

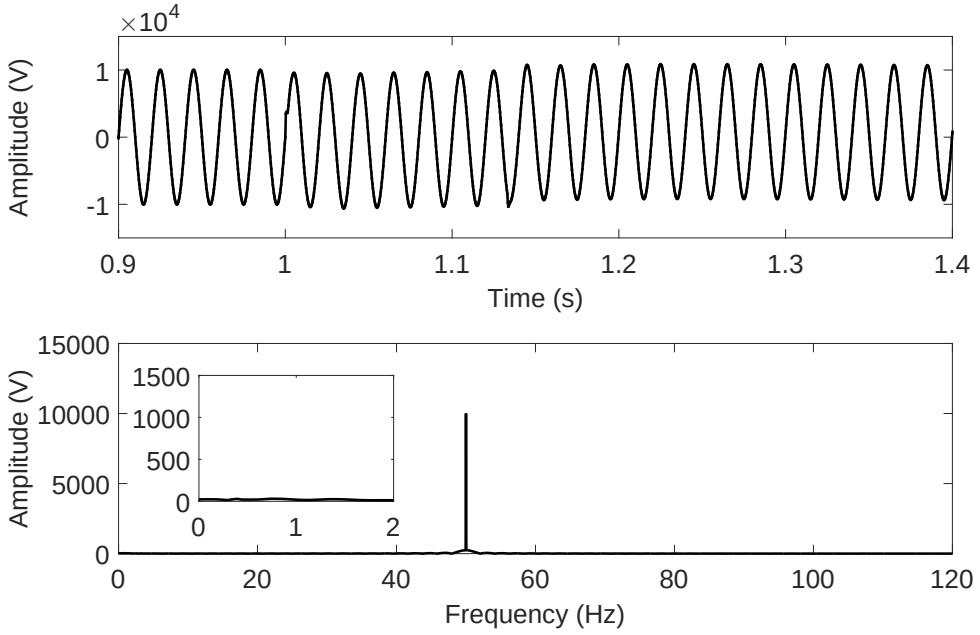

Figure 4.14: The waveform and spectrum of the input signal $i(t)$ with damped LFO.

causes slight changes in the waveform of the original signal. Moreover, the LFO component is damped and accompanied by an extremely high frequency signal. However, since the LFO signal is damped (non-periodic) and the frequency is

extremely low, it cannot be analysed by an FFT. Therefore, the the amplitude is extremely close to zero indicating that the value is extraordinary small as shown in the zoomed graph of Fig. 4.14.

Applying the same SE which is a flat-line SE with the length of 10 ms and its origin at the centre, the corresponding waveform and spectrum of the output signal, after using the LFO extraction MF, are presented in Fig. 4.15. According to Fig. 4.15, besides removing the fundamental frequency compo-

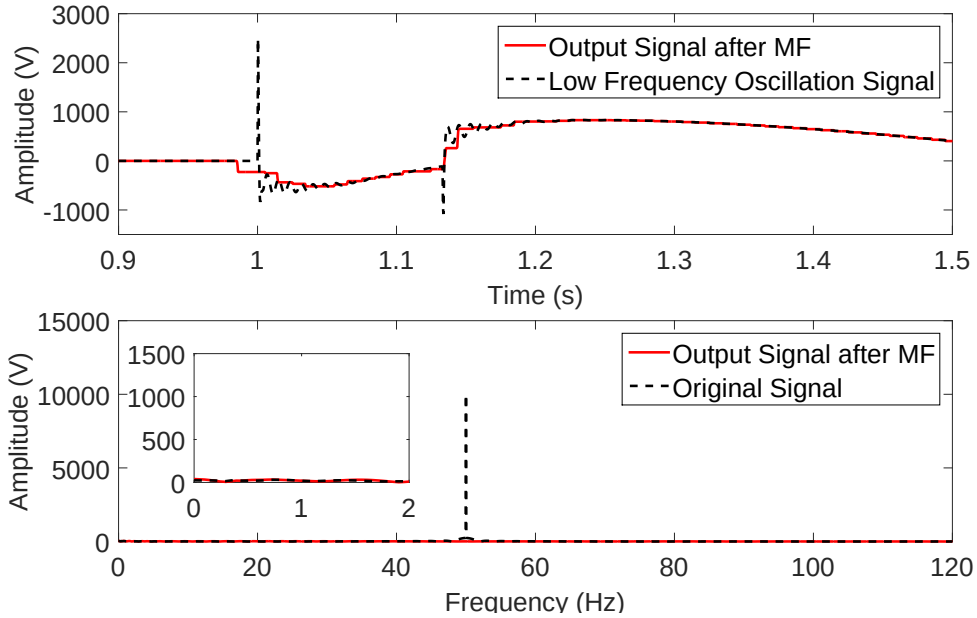

Figure 4.15: The waveform and spectrum of the output signal of MF when LFO is damped.

nent as required, the high frequency component accompanied with the damped LFO is also removed using this MF, which implies that the MF has extraordinary performance in tracing damped LFO components. Secondly, since FFT cannot be applied to analyse low frequency non-periodic components in signals, the LFO extraction MF is able to deal with non-periodic signals successfully which expands its range of applications. Thirdly, the MF detects the start of the damped LFO with little time delay which demonstrates its potential in real-time analysis. Large quantity of simulations have been undertaken by

changing the data in the model to produce signals with different damped LFO components and similar results have been obtained. Moreover, it averagely takes 1.5816 second to process signals with damped LFO components using the proposed MF.

For further simulations of the LFO extraction MF in practical circumstances, a noisy environment is considered. SNR level of 40 dB, 30 dB and 20 dB noisy environments are simulated, respectively. In order to pollute the input signal with WGN, a noise vector is generated randomly, by giving a specified SNR level, such as 30 dB. Then the power of the input signal and the power of the noise vector are calculated. According to these parameters, the amplitude scaling factor for the noise vector is obtained. With these characteristics, the input signal corrupted with WGN of a desired SNR level can be generated. Similar results are obtained as shown in Figs. 4.16, 4.17 and 4.18.

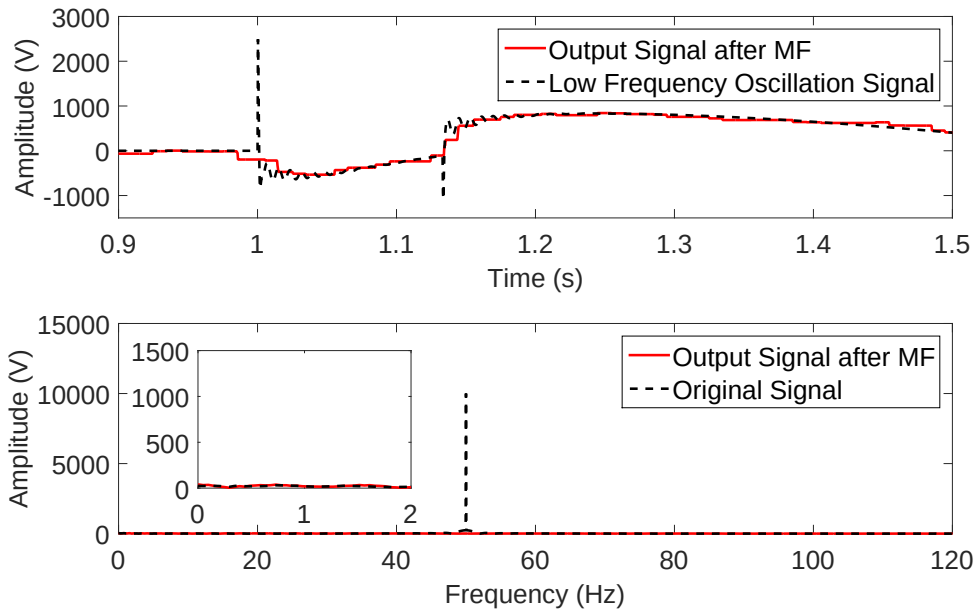

Figure 4.16: The waveform and spectrum of the output signal of MF when LFO is damped with 40 dB WGN.

When the SNR level is 40 dB, the waveform of the output signal after MF is smooth. However, when the SNR level is 30 or 20 dB, the waveform of

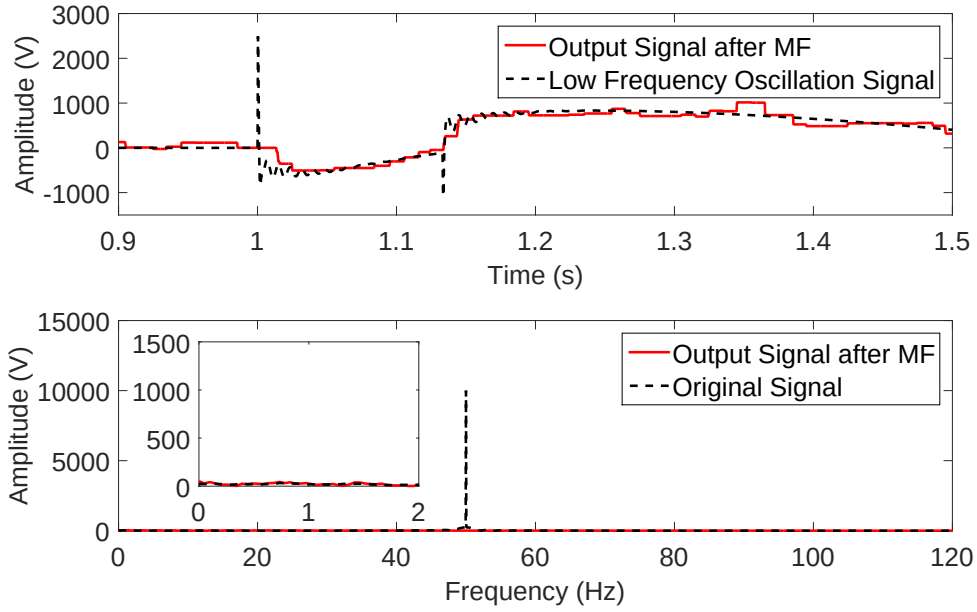

Figure 4.17: The waveform and spectrum of the output signal of MF when LFO is damped with 30 dB WGN.

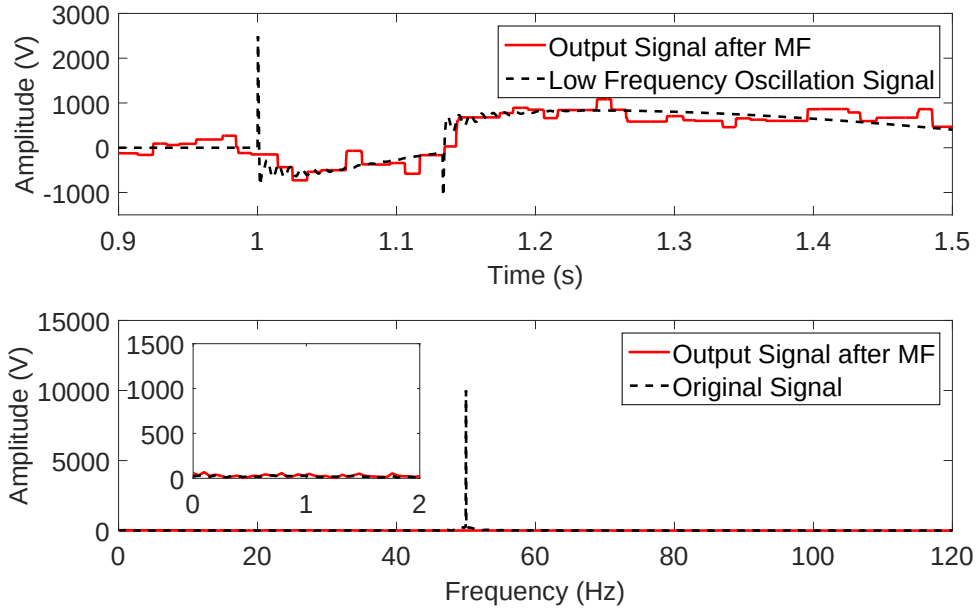

Figure 4.18: The waveform and spectrum of the output signal of MF when LFO is damped with 20 dB WGN.

the output signal after MF contains raised and sunk squares because of the pollution of WGN. Nevertheless, the overall trend of these square fluctuations are the same with the original LFO component and the results are considerable to some extent under the noisy circumstances.

The error distributions for SNR levels from 20 to 40 dB through Monte Carlo simulation [117] based on 500 separate experiments are shown in Fig. 4.19. Through this figure, it is obvious that the lower the SNR level is, the

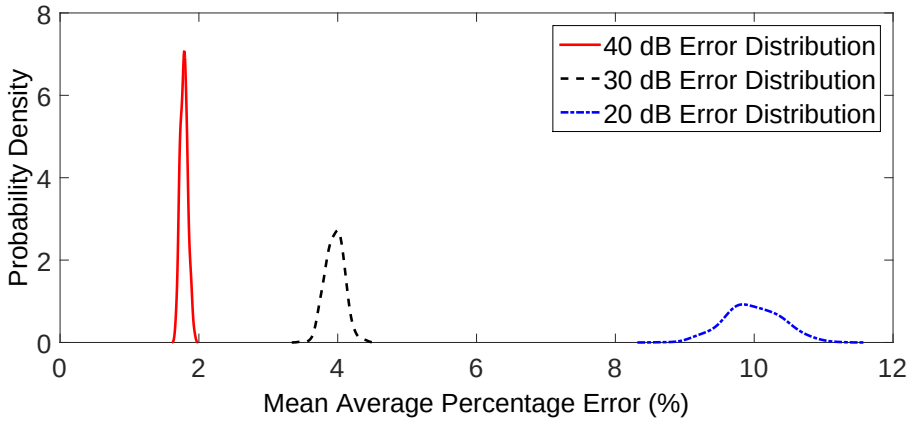

Figure 4.19: The error distribution under different SNR levels.

larger the mean average percentage error (MAPE) is, which increases from 2% to 10%. This phenomenon indicates that the proposed method are more effective in the environment of SNR levels larger than 20 dB and the SNR level is normally larger than 30 dB in most systems [118]. Other than the noisy environment, when there is any second harmonic component existing in the input signal, the proposed method is not totally effective. Additionally, compared to conventional methods, this method directly acts on the waveform of the target signal, which means that the proposed MF cannot provide feature values of the LFO components. As a consequence, much more studies are required for more complicated situations when applying the LFO extraction MF to detect damped LFO.

Quantisation Influence Analysis

Quantisation, is the process of mapping a large set of input values into a (countable) smaller set, such as rounding values to some unit of precision, and it is an essential procedure before practical signal processing [119]. Therefore, an analysis about the influence of the quantisation process on the proposed method is undertaken in this simulation study. After producing the synthetic input signal by using the model, the input signal is processed by quantisation between 8-bit and 16-bit from the simulation applied in MATLAB. The quantised input signals are then filtered by the proposed LFO extraction MF to extract damped LFO components. A quantisation error is calculated according to the difference between the result after using the MF to the quantised input signal and the actual LFO component. The quantisation error equation is given as:

$$Q_{error} = \sqrt{\sum_{i}^{N_s}(x_i - \bar{X}_i)^2} \tag{4.3.2}$$

where N_s is the number of samples, x is the output signal after MF using the N quantised input signal and X is the original LFO component. By comparing the quantisation errors of the output signals after MF with and without the quantisation procedure, the effect of quantisation on the proposed MM method can be measured. The input signal shown in Fig. 4.14 is processed with N-bit quantisation between 8-bit and 16-bit and the corresponding results are presented in Table 4.4.

Table 4.4: Quantisation errors of N-bit quantisation from 8-bit to 16-bit and the error of the result without quantisation

N-bit	8	10	12	14	16	Error Without Q
Q_{error}	3.9905	3.9463	3.9462	3.9462	3.9461	3.9455

Table 4.4 shows the quantisation errors of N-bit quantisation from 8-bit to 16-bit and the error of the outcome without quantisation. It is apparent the quantisation errors of output signals after MF with quantisation decreases when the number of bit increases. Moreover, from 10-bit to 16-bit quantisation, the

quantisation errors are approximately the same with only an average different of 0.0001 which can be neglected.

Fig. 4.20 demonstrates the output signal after using MF when the input signal is processed by an 8-bit quantisation. By comparing the waveforms in

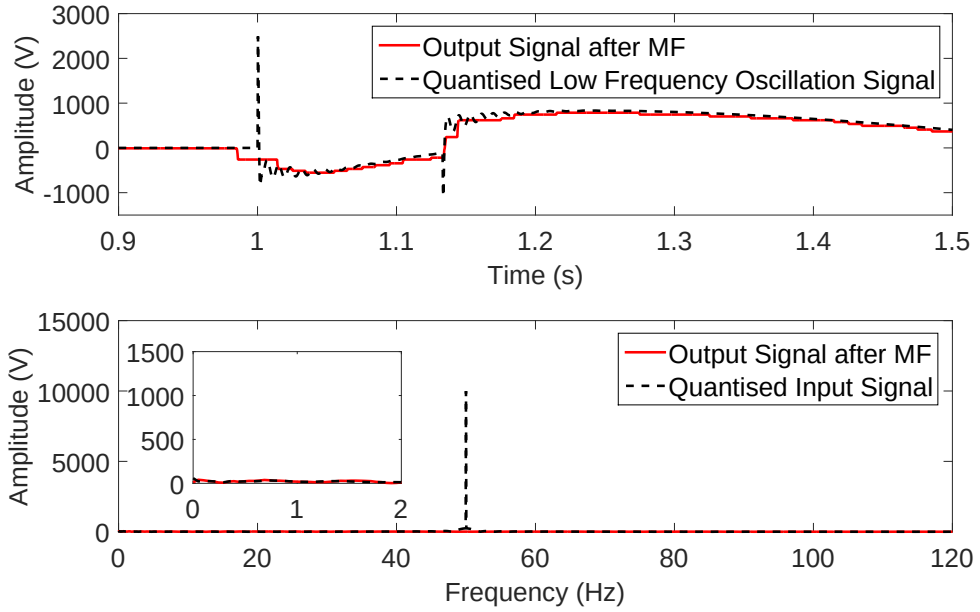

Figure 4.20: The waveform and spectrum of the output signal of MF when the input signal is processed by an 8-bit quantisation.

Fig. 4.20 and Fig. 4.15, it depicts that the two output signals with or without quantisation are extremely similar. When processing quantisation from 10-bit to 16-bit, similar results have been obtained. According to these phenomena, the quantisation process has little influence on the proposed technique.

In order to verify the impact of quantisation process on the LFO extraction MF in the presence of noise, the input signal is polluted by WGN with SNR level of 30 dB. The output signal after MF when input signal is processed by an 8-bit quantisation in a noisy environment with SNR level of 30 dB is illustrated in Fig. 4.21. Comparing the waveforms in Fig. 4.21 and Fig. 4.17, they are slightly different but the overall trend of the fluctuations are the same.

Table 4.5 presents the quantisation errors of N-bit quantisation from 8-bit

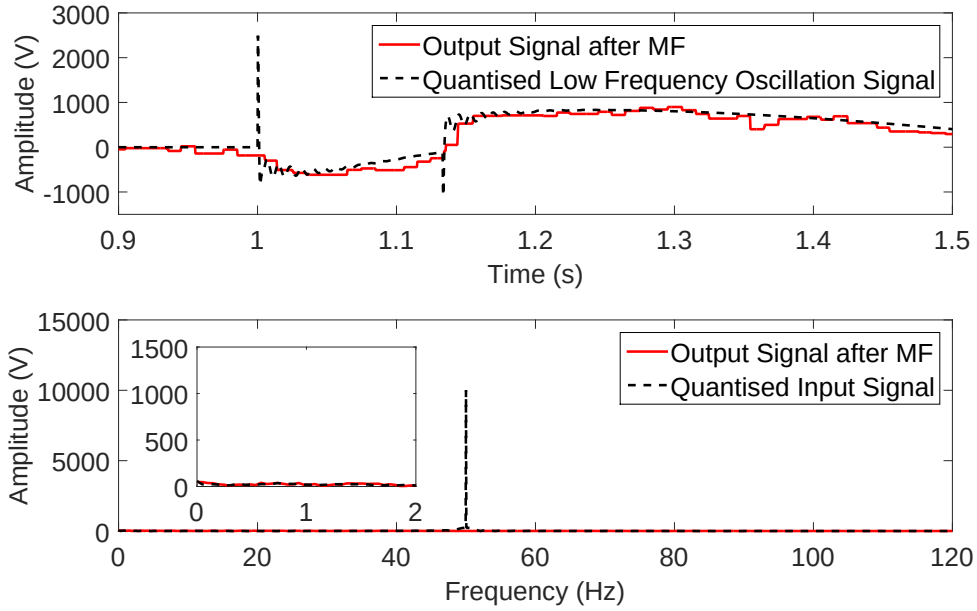

Figure 4.21: The waveform and spectrum of the output signal of MF when the input signal with 30 dB WGN is processed by an 8-bit quantisation.

to 16-bit and the error of the result without quantisation in noisy environments. Although the values of Q_{error} with quantisation process are slightly larger than the error without quantisation process, these numbers are similar with an average difference of 0.2.

Table 4.5: Quantisation errors of N-bit quantisation from 8-bit to 16-bit and the error of the result without quantisation in the noisy environment with SNR level of 30 dB

N-bit	8	10	12	14	16	Error Without Q
Q_{error}	4.8956	4.8033	4.7207	4.6805	4.6399	4.5241

The error distributions of N-bit quantisation from 8-bit to 16-bit in a noisy environment with a SNR level of 30 dB through Monte Carlo simulation based on 500 separate experiments have been provided as shown in Fig. 4.22. The MAPE of N-bit quantisation process in a noisy environment with a SNR level of 30 dB are similarly around 4%, which again implies that the quantisation

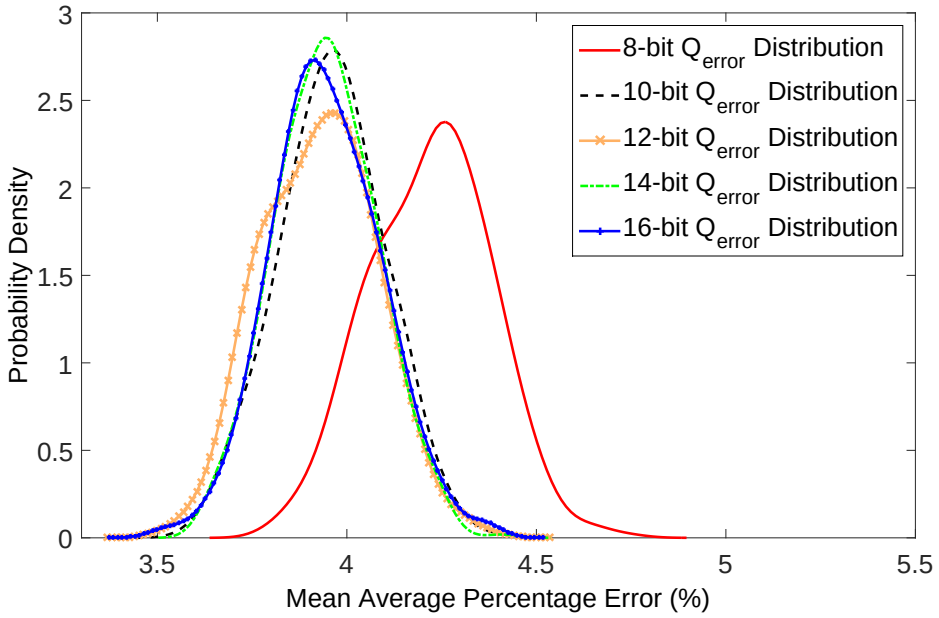

Figure 4.22: The error distribution of N-bit quantisation from 8-bit to 16-bit in the noisy environment with an SNR level of 30 dB.

procedure has little influence on the proposed MF even with the presence of noise. Moreover, from 10-bit to 16-bit quantisation, the MAPE almost maintain the same value. Hence, a 10-bit quantisation process is enough using the proposed method. Referring to the outcomes of quantisation process with or without considering the noisy environments, it is obvious that the quantisation process has little impact on the performance of the LFO extraction MF. Therefore, it can be conclude that the LFO extraction MF can be easily implemented to detect damped LFO in practical equipment.

4.4 Conclusions

In this chapter, an algorithm with the combination of MF and GSO is firstly proposed to detect continuous LFO components. This approach applies an envelope extraction MF to extract the envelopes of the target signal in the first place. GSO, an optimisation algorithm based on animal searching behaviour,

is then utilised for the estimation of the parameters of the extracted envelopes in order to reconstruct the continuous LFO component. Furthermore, another approach has also been generated for extraction of damped LFO components in power system signals. This method uses another LFO extraction MF to directly detect the existence of damped LFO components.

Signals containing continuous LFO components with time-varying frequency and amplitude are generated from a pre-built power system model to estimate the efficiency of the hybrid algorithm. From the simulation results, the proposed technique provides a more robust, accurate and steady way to estimate the parameters of the LFO in severely noisy environments and they also reveal its potential in online detection of LFO. Firstly, this method is still effective when the input signal is seriously polluted by WGN. Secondly, only 10 seconds of the input data is required to process GSO in this algorithm, whose performance is much better than the conventional methods in detecting LFO component in nowadays. Thirdly, MF uses only additions and subtractions which also decreases the computational complexity of the proposed approach. Fourthly, GSO is robust for optimising high-dimensional and multi-modal problems, which benefits the accurate estimations of both the frequency and amplitude of the LFO and proves the ability of the proposed method in online detection of LFO in power systems. Furthermore, the results with low standard deviation values consistent over 50 times experiments have been obtained which express the stability of the approach. The application of GSO in this chapter can be regarded as a double-edged sword, since this hybrid method provides the feature values of the target LFO components and benefits from its robustness in dealing with issues that are hard to accurately describe, while this algorithm is not efficient when applied signals containing damped LFO components since the computational time consumption rises greatly when applying GSO to calculate the parameters of damped ones. The performance of the hybrid scheme on detecting continuous LFO components considering more complicated circumstances, such as multi-LFO situations, will be analysed in the follow-on work.

As for detecting damped LFO components, the LFO extraction MF also has an advantage in obtaining the same performance with simpler calculations compared to conventional methods. Secondly, compared with traditional methods, for example FFT, the proposed MF is still effective for non-periodic signals. Additionally, different from popular techniques in recent years, calculating power system parameters and then reconstructing LFO components, the proposed method extracts LFO components directly and provides another way in dealing with LFO from a new point of view. However, the algorithm only based on MF is only able to extract LFO components and the parameters cannot be obtained through this process, which is also one of its drawbacks. A quantisation influence analysis has undertaken and the results have shown that the performance of the LFO extraction MF is not affected by the quantisation process, which means that this method can be easily applied for detecting damped LFO in practical equipment.

Chapter 5

Detection and Removal of Power System Harmonics

Power system harmonics lead to power quality problems within a vast variety of power electronic equipment. Additionally, with the development of semiconductor devices, power electronics technologies have been extensively utilised for a wide range of applications in the daily life, such as lighting, adjust speed drivers, and uninterruptible power supply systems. Due to their non-linear characteristics, most power electronic equipment cause non-sinusoidal currents, which result in severe harmonic contamination in the distribution grids. Therefore, proposing an effective method to detect and reduce harmonics is essential and urgent for the improvement of the performance of power systems.

This chapter proposes convolved morphological filters (CMF) to detect and eliminate power system harmonics. The main purpose of this approach is to combine convolution method, which is viewed as the linear filtering techniques, with an MF as a low-pass non-linear filter in order to take advantages of both approaches. In the whole process, the output signal filtered by MF is convolved with a proper pre-designed impulse response function and this is regarded as the CMF. Applied to synthetic power system signals with harmonic components, CMF can remove harmonics and maintain the fundamental frequency

component even in noisy environments. However, only Dirac delta function was chosen as the impulse response function in CMF and the results were not completely satisfied in [101]. Therefore, inspired by the work in [101], different impulse response functions are utilised in the convolution process of the proposed CMF and the implementations of them are firstly introduced. A variety of tests are simulated and different types of impulse response functions in the convolution process are applied. Moreover, the results of the proposed CMF are also compared with that of the MF. The outcomes of the simulation studies illustrate that harmonic components in the target signal are removed successfully and efficiently to most extent by using the CMF. In addition to the application of CMF with different impulse response functions, a refined MF with optimised SE to improve its performance in dealing with harmonics by using standard particle swarm optimiser (PSO) is also developed.

5.1 Different Impulse Response Functions

The following sections concentrate on demonstrating the implementation of different impulse response functions for the convolution process which will be applied in the simulation studies.

5.1.1 Dirac Delta Function

In [101], the Dirac delta function was applied as the impulse response function for the CMF. The process of implementing a Dirac delta function is shown as follows. Firstly, an impulse response function $h_1(t)$ is defined as below:

$$h_1(t) = \sqrt{\frac{\alpha}{\pi}} \cdot e^{-\alpha t^2}. \tag{5.1.1}$$

As a result, the corresponding frequency response $H_1(f)$ is given as:

$$H_1(f) = e^{-\frac{\pi^2 \cdot f^2}{\alpha}}. \tag{5.1.2}$$

In this case, $h_1(t)$ and $H_1(f)$ have both a shape with peak at $n = 0$ and $f = 0$ respectively. Moreover, they both decay exponentially when moving away

from 0 based on α. Consequently, it can be ideal for clearing the unexpected frequencies using a proper α. If $H_1(f)$ is shifted with f_0, then it becomes:

$$H_2(f) = H_1(f - f_0) = e^{-\frac{\pi^2 \cdot (f-f_0)^2}{\alpha}}. \tag{5.1.3}$$

The corresponding variance of the signal in the time domain is presented as:

$$h_2(t) = h_1(t) \cdot e^{j2\pi f_0 t}. \tag{5.1.4}$$

If the mirror frequency is also considered, $H(f)$ can be developed as:

$$\begin{aligned} H(f) &= H_1(f - f_0) + H_1(f + f_0) \\ &= \left(e^{-\frac{\pi^2 \cdot (f-f_0)^2}{\alpha}} + e^{-\frac{\pi^2 \cdot (f+f_0)^2}{\alpha}} \right). \end{aligned} \tag{5.1.5}$$

Therefore, in the time domain, the impulse response function $h(t)$ will have the following relation, shown as:

$$\begin{aligned} h(t) &= h_1(t) \cdot e^{j2\pi f_0 t} + h_1(t) \cdot e^{-j2\pi f_0 t} \\ &= 2h_1(t) \cdot \cos(2\pi f_0 t) \\ &= 2\sqrt{\frac{\alpha}{\pi}} \cdot e^{-\alpha t^2} \cdot \cos(2\pi f_0 t). \end{aligned} \tag{5.1.6}$$

This equation represents the Dirac delta function regarded as the impulse response function in CMF and α is normally set to be π^2.

5.1.2 Infinite Impulse Response Function

A Butterworth filter, which is a typical infinite impulse response (IIR) filter designed to have a frequency response as flat as possible in the passband, is specifically designed in this application. The major advantage of the Butterworth filter is maximally flat in the passband and rolls off towards zero in the stopband. However, the roll-off of the Butterworth filter is not sharp enough, and thus it will require a higher order to implement a particular stopband specification [120]. In order to implement a digital IIR filter, the relative analogue IIR filter will be initially designed.

Design of Analogue IIR Filters

The transfer function of the Butterworth filter can be written in the complex form as:

$$H(s) = \frac{K_0}{\prod_{k=1}^{N}(s - s_k)/\Omega_c}, \quad (k = 1, 2, \cdots, 2N), \tag{5.1.7}$$

where $s_k = \Omega_c e^{j\left(\frac{1}{2}+\frac{2k-1}{2N}\right)\pi}$ and Ω_c is the cut-off frequency. If s is divided by Ω_c in Eqn. (5.1.7), the corresponding cut-off frequency is equal to 1. Thus, the transfer function is referred as a normalised transfer function and it is shown as:

$$H(s^{'}) = \frac{K_0}{\prod_{k=1}^{N}(s^{'} - s_k^{'})}, \quad (k = 1, 2, \cdots, 2N), \tag{5.1.8}$$

where $s^{'} = s/\Omega_c$. The value of K_0 determines the amplitude of the filter. If the amplitude of the original signals needs to be maintained, the value of K_0 is always set to 1. The polynomials are also normalised by setting $\Omega_c = 1$. The normalised Butterworth polynomials then have the general form, given as:

$$\begin{cases} B_n(s) = \prod_{k=1}^{\frac{N}{2}} \left[s^2 - 2s\cos\left(\frac{2k+N-1}{2N}\,\pi\right) + 1\right], N \text{ is even} \\ \\ B_n(s) = (s+1)\prod_{k=1}^{\frac{N-1}{2}} \left[s^2 - 2s\cos\left(\frac{2k+N-1}{2N}\,\pi\right) + 1\right], N \text{ is odd} \end{cases} \tag{5.1.9}$$

Therefore, in order to design a Butterworth filter, it is necessary to determine the parameters of N and Ω_c in the first place.

Consider a power system signal consisting of a basic 50 Hz power frequency, and harmonics above 150 Hz. The requirement of the filter is:

- In passband: $0 \leq \Omega \leq 2\pi \times 50\,\text{rad/s}$,damping ratio $\delta_1 \leq 1\,\text{dB}$;
- In stopband: $\Omega \geq 2\pi \times 150\,\text{rad/s}$,damping ratio $\delta_2 \geq 15\,\text{dB}$.

The following equation is used to determine the parameter N, presented as:

$$20\log_{10}|H_a(j\Omega)| = -10\log_{10}\left[1 + \left(\frac{\Omega}{\Omega_c}\right)^{2N}\right]. \tag{5.1.10}$$

According to the requirements, it can be rewritten as:

$$-10\log_{10}\left[1+\left(\frac{2\pi\times 50}{\Omega_c/(\text{rad}\cdot\text{s}^{-1})}\right)^{2N}\right]\geq -1, \tag{5.1.11}$$

$$-10\log_{10}\left[1+\left(\frac{2\pi\times 150}{\Omega_c/(\text{rad}\cdot\text{s}^{-1})}\right)^{2N}\right]\leq -15. \tag{5.1.12}$$

Therefore, considering the equals in the equations, they become:

$$1+\left(\frac{2\pi\times 50}{\Omega_c/(rad\cdot s^{-1})}\right)^{2N}=10^{0.1}, \tag{5.1.13}$$

$$1+\left(\frac{2\pi\times 150}{\Omega_c/(rad\cdot s^{-1})}\right)^{2N}=10^{1.5}. \tag{5.1.14}$$

Dividing Eqn. (5.1.14) by Eqn. (5.1.13), the equation for calculating N is obtained:

$$\left(\frac{150}{50}\right)^{2N}=\frac{10^{1.5}-1}{10^{0.1}-1}. \tag{5.1.15}$$

Thus, N is calculated as:

$$N=\frac{\log_{10}\left(\frac{10^{1.5}-1}{10^{0.1}-1}\right)}{2\log_{10}(3)}=2.17227. \tag{5.1.16}$$

Meanwhile, Ω_c is figured as:

$$\Omega_c=\frac{2\pi\times 150}{(10^{1.5}-1)^{\frac{1}{2\times 2.17227}}}=428.76799\ \text{rad/s}. \tag{5.1.17}$$

If $N=3$, the corresponding Ω_c is:

$$\Omega_c=532.84026\ \text{rad/s}. \tag{5.1.18}$$

Referring to table 5.1, which presents the polynomials of normalised Butterworth transfer function, the normalised Butterworth transfer function is obtained as:

$$H(s^{'})=\frac{1}{1+2s'+2s'^2+s'^3}=\frac{1}{(s'+1)(s'^2+s'+1)}, \tag{5.1.19}$$

where $s^{'}=s/\Omega_c$. Hence, the corresponding Butterworth transfer function is expressed as:

$$H(s)=\frac{\Omega_c^3}{(s+\Omega_c)(s^2+\Omega_c s+\Omega_c^2)}. \tag{5.1.20}$$

$H(s)$ can then be calculated by substituting the value of Ω_c into the equation above.

Table 5.1: The polynomials of a normalised Butterworth transfer function when $K_0 = 1$

N	a_1	a_2	a_3	a_4
1	1			
2	1.414 213 6			
3	2.000 000 0	2.000 000 0		
4	2.613 125 9	3.414 213 6	2.613 125 9	
5	3.236 068 0	5.236 068 0	5.236 068 0	3.236 068 0

Transformation from $H(s)$ to $H(z)$

After designing the analogue filter, we have to transfer $H(s)$ into $H(z)$ in order to design the digital one. Two methods, impulse invariance method and bilinear transformation method, are discussed in the project.

Impulse invariance method Impulse invariance is a technique for designing discrete-time IIR filters from continuous-time filters in which the impulse response of the continuous-time system is sampled to produce the impulse response of the discrete-time system [121]. The frequency response of the discrete-time system is a sum of shifted copies of the frequency response of the continuous-time system. If the continuous-time system is approximately band limited to a frequency less than the Nyquist frequency of the sampling system, then the frequency response of the discrete-time system is approximately equal to it for frequencies below the Nyquist frequency. If the system is not band limited to a frequency less than the Nyquist frequency, aliasing distortion would occur [121].

Let $h(n)$ be the unit impulse response of the digital IIR filter and $h(t)$ be the unit impulse response function of the analogue one. The Impulse invariance method is to let $h(n)$ equals the sample value of $h(t)$, which can be shown as $h(n) = h(nT)$, where T is the sampling period of $h(t)$. If

$H(s) = L[h(t)]$, $H(z) = Z[h(n)]$, then the equation below is derived:

$$H(z)\,|_{z=e^{sT}} = \frac{1}{T}\sum_{k=-\infty}^{\infty} H\left(s - j\frac{2\pi}{T}k\right). \tag{5.1.21}$$

This equation shows that $H(s)$ is extended periodically in imaginary axis in the first place and it is then mapped into z-plane. In this way, the corresponding $H(z)$ is obtained.

If the continuous poles at $s = s_k$, the system function can be written in partial fraction expansion as:

$$H(s) = \sum_{k=1}^{N} \frac{A_k}{s - s_k}. \tag{5.1.22}$$

Therefore, applying the inverse Laplace transform, the impulse response function of the continuous-time system is:

$$\begin{aligned} h(t) &= L^{-1}[H(s)] = \sum_{k=1}^{N} A_k e^{s_k t} u(t), \\ \text{where}\, u(t) &= \begin{cases} 1, & t \geq 0 \\ 0, & otherwise \end{cases} \end{aligned} \tag{5.1.23}$$

The impulse response function $h(n)$ of the corresponding discrete-time system is then defined as:

$$h(n) = h(nT) = \sum_{k=1}^{N} A_k e^{s_k nT} u(nT) = \sum_{k=1}^{N} A_k e^{s_k nT} u(n). \tag{5.1.24}$$

Performing a z-transform on $h(n)$ produces the following function, illustrated as:

$$\begin{aligned} H(z) = Z[h(n)] &= \sum_{n=-\infty}^{\infty} h(n) z^{-n} \\ &= \sum_{n=0}^{\infty} \left[\sum_{k=1}^{N} A_k (e^{s_k T} z^{-1})^n \right] \\ &= \sum_{k=1}^{N} \left[\sum_{n=0}^{\infty} (e^{s_k T} z^{-1})^n \right] A_k \\ &= \sum_{k=1}^{N} \frac{A_k}{1 - e^{s_k T} z^{-1}}. \end{aligned} \tag{5.1.25}$$

As a consequence, the poles from the continuous-time system function are translated to poles at $z = e^{s_k T}$ and the corresponding coefficients of the system function $H(z)$ of the digital IIR filter and that of the $H(s)$ are maintained.

Since poles in the continuous-time system at $s = s_k$ transform to poles in the discrete-time system at $z = e^{s_k T}$, poles in the left half of the s-plane are mapped into inside the unit circle in the z-plane. Therefore, if the continuous-time filter is causal and stable, then the discrete-time filter would be causal and stable as well [122].

As observed from (5.1.21), the system function of the digital IIR filter is inversely proportional to T. When the value of T becomes small, the gain of the digital IIR filter will increase. In order to prevent the effect of sampling period, the impulse response function of the discrete-time system is written as:

$$h(n) = T\, h(nT). \tag{5.1.26}$$

Correspondingly, $H(z)$ becomes:

$$H(z) = \sum_{k=1}^{N} \frac{T A_k}{1 - e^{s_k T} z^{-1}}. \tag{5.1.27}$$

The frequency response of the digital IIR filter is given as:

$$H(e^{j\omega}) = \sum_{k=-\infty}^{\infty} H(j\frac{\omega}{T} + j\frac{2\pi}{T}k). \tag{5.1.28}$$

If the continuous time filter is approximately band limited, then the frequency response of the discrete-time system can be considered as the continuous-time system's frequency response for frequencies below π radians per sample (below the Nyquist frequency calculated as $1/(2T)$ Hz):

$$H(e^{j\omega}) \approx H(j\frac{\omega}{T}) \quad \text{for } |\omega| < \pi. \tag{5.1.29}$$

Bilinear transform method The bilinear transform is used in digital signal processing and discrete-time control theory to transform continuous-time system representations to discrete-time and vice versa and it is suitable for

designing band limited filters.[123]. The bilinear transform is applied to transform continuous-time transfer function $H(s)$ to discrete-time transfer function $H(z)$. To make it clearer, this transform maps positions on the $j\Omega$ axis in the s-plane to the unit circle $|z| = 1$ in the z-plane.

The first step is to shrink transfer function from s-plane to s_1-plane where the $j\Omega$ axis boundaries are limited within $[-\pi/T, \pi/T]$. The shrink transfer relationship function from s-plane to s_1-plane is expressed as:

$$\Omega = c \cdot \tan\left(\frac{\Omega_1 T}{2}\right), \tag{5.1.30}$$

where c is a undetermined constant. By applying Eular's law, this equation can be rewritten as:

$$j\Omega = \frac{e^{j\frac{\Omega_1 T}{2}} - e^{-j\frac{\Omega_1 T}{2}}}{e^{j\frac{\Omega_1 T}{2}} + e^{-j\frac{\Omega_1 T}{2}}} c. \tag{5.1.31}$$

Let $s = j\Omega$ and $s_1 = j\Omega_1$, the above equation can be expressed as:

$$s = \frac{e^{\frac{s_1 T}{2}} - e^{-\frac{s_1 T}{2}}}{e^{\frac{s_1 T}{2}} + e^{-\frac{s_1 T}{2}}} = \tanh\left(\frac{s_1 T}{2}\right) \cdot c = \frac{1 - e^{-s_1 T}}{1 + e^{-s_1 T}} c. \tag{5.1.32}$$

In the second step, the s_1-plane is transferred to the z-plane. The corresponding relationship is $\omega = \Omega_1 T$, that is $z = e^{s_1 T}$. According to the relationship, the mapping relationship between s-plane and z-plane is given as:

$$s = \frac{1 - z^{-1}}{1 + z^{-1}} c, \tag{5.1.33}$$

$$z = \frac{c + s}{c - s}. \tag{5.1.34}$$

Let $z = e^{j\omega}$, the following equation is obtained:

$$s = \frac{1 - e^{j\omega}}{1 + e^{j\omega}} c = \frac{e^{j\frac{\omega}{2}} - e^{-j\frac{\omega}{2}}}{e^{j\frac{\omega}{2}} + e^{-j\frac{\omega}{2}}} c = jc \cdot \tan\left(\frac{\omega}{2}\right) = j\Omega, \tag{5.1.35}$$

which indicates that the unit circle on z-plane is mapped into the image axis $j\Omega$ one the s-plane. Meanwhile, for z:

$$z = \frac{c + s}{c - s} = \frac{c + \sigma + j\Omega}{c - \sigma - j\Omega} \tag{5.1.36}$$

and

$$|z| = \sqrt{\frac{(c + \sigma)^2 + \Omega^2}{(c - \sigma)^2 + \Omega^2}}. \tag{5.1.37}$$

The equations above indicate that when $\sigma < 0$, the denominator is larger than numerator and $|z| < 1$. Therefore, left half side of the s-plane is mapped into the inside unit circle in z-plane and both systems remain stable. When $\sigma > 0$, the denominator is smaller than numerator and $|z| > 1$. Hence, the right half side of s-plane is mapped into the outside unit circle in z-plane. When $\sigma = 0$, $|z| = 1$ and the imaginary axis $j\Omega$ is mapped on the unit circle in z-plane [122].

The next step is to determine the value of the constant c. The equation of the shrink transfer relationship function indicates the linear relationship only happens when $\Omega_1 T$ is a very small value, which usually in the range of 0.3π. The relationship is expressed as:

$$\Omega \approx c\frac{\Omega_1 T}{2}. \tag{5.1.38}$$

Under this circumstance, a proper parameter c can determine the relationship between the frequency characteristics of the analogue filter and digital filter. There are two common ways to determine the value of c:

1. Choosing $\Omega \approx \Omega_1$ at low frequency, and $c = \frac{2}{T}$.

2. Choosing $\omega_c = \Omega_{1c} T$ as the specific frquency of the digital filter; Choosing Ω_c as the specific frequency of the analogue one, then we will have $\Omega_c = c \cdot \tan\left(\frac{\Omega_{1c} T}{2}\right) = c \cdot \tan\left(\frac{\omega_c}{2}\right)$. Thus, $c = \Omega_c \cot\left(\frac{\omega_c}{2}\right)$.

After the constant c is determined, the following equation can be utilised to obtain $H(z)$, shown as:

$$H(z) = H(s)\,|_{s=c\frac{1-z^{-1}}{1+z^{-1}}}. \tag{5.1.39}$$

As introduced previously, impulse invariance method results in aliasing distortion if it is not band-limited. The bilinear transform method can deal with this problem. Substituting $c = \frac{2}{T}$ into (5.1.30), the following equation is obtained:

$$\Omega = \frac{2}{T}\tan(\frac{\omega}{2}). \tag{5.1.40}$$

This can be rewritten as:

$$\omega = 2\arctan(\frac{T}{2}\Omega). \tag{5.1.41}$$

The equation above indicates that when Ω changes from $0 \to +\infty$, ω varies from $0 \to \pi$. In this situation, the positive imaginary axis in s-plane is mapped into upper half of the unit circle in z-plane. When Ω changes from $0 \to -\infty$, ω varies from $0 \to -\pi$. In this case, the negative imaginary axis in s-plane is mapped into lower half of the unit circle in z-plane. Therefore, aliasing distortion would not be caused. This is also the main advantage of bilinear transform method.

In this implementation, assume $T = 3200$ and the corresponding $c = \frac{2}{T} = 6.25 \times 10^{-4}$. With the normalised Butterworth transfer function previously determined, the transferring from $H(s)$ to $H(z)$ by using the bilinear transform method is obtained and the calculation procedure and parameters are shown below:

$$\begin{aligned} H(s) &= \frac{1}{1 + 2\frac{s}{\Omega_c} + 2\frac{s^2}{\Omega_c^2} + \frac{s^3}{\Omega_c^3}} \\ &= \frac{\Omega_c^3}{\Omega_c^3 + 2\Omega_c^2 s + 2\Omega_c^2 s^2 + s^3} \end{aligned} \tag{5.1.42}$$

$$s = c\frac{1 - z^{-1}}{1 + z^{-1}} = c\frac{z - 1}{z + 1} \tag{5.1.43}$$

$$\begin{aligned} H(z) &= \frac{\Omega_c^3}{\Omega_c^3 + 2\Omega_c^2 c\frac{z-1}{z+1} + 2\Omega_c^2 c^2\frac{(z-1)^2}{(z+1)^2} + c^3\frac{(z-1)^3}{(z+1)^3}} \\ &= \frac{\Omega_c^3(z+1)^3}{\Omega_c^3(z+1)^3 + 2\Omega_c^2 c(z-1)(z+1)^2 + 2\Omega_c^2 c^2(z-1)^2(z+1) + c^3(z-1)^3} \\ &= A\frac{1 + \beta_1 z^{-1} + \beta_2 z^{-2} + \beta_3 z^{-3}}{1 - \alpha_1 z^{-1} - \alpha_2 z^{-2} - \alpha_3 z^{-3}} \end{aligned} \tag{5.1.44}$$

where

$$
\begin{aligned}
A &= \frac{\Omega_c^3}{\Omega_c^3 + 2\Omega_c^2 c + 2\Omega_c c^2 + c^3} = 1 \\
\beta_1 &= 3 \\
\beta_2 &= 3 \\
\beta_3 &= 1 \\
\alpha_1 &= \frac{3\Omega_c^3 + 2\Omega_c^2 c - 2\Omega_c c^2 - 3c^3}{A} = 4.5385 \times 10^8 \\
\alpha_2 &= \frac{3\Omega_c^3 - 2\Omega_c^2 c - 2\Omega_c c^2 + 3c^3}{A} = 4.5385 \times 10^8 \\
\alpha_3 &= \frac{\Omega_c^3 - 2\Omega_c^2 c + 2\Omega_c c^2 - c^3}{A} = 1.5128 \times 10^8
\end{aligned}
\tag{5.1.45}
$$

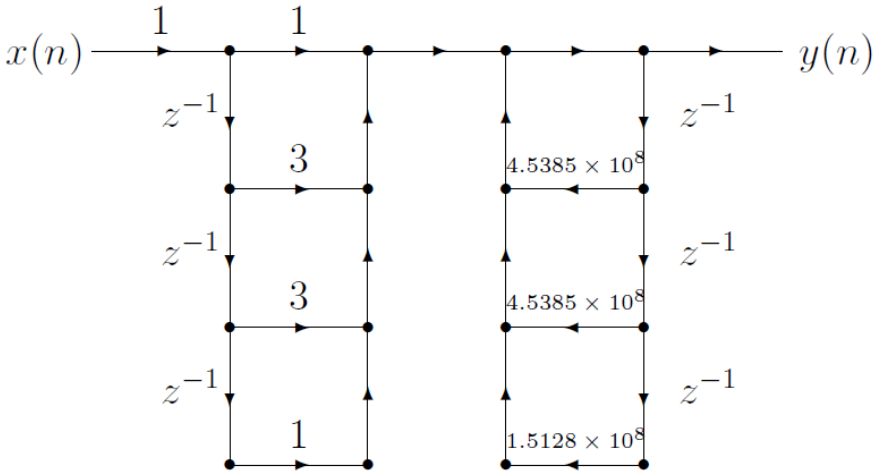

Figure 5.1: The IIR filter block diagram

Fig. 5.1 illustrates the block diagram of the designed Butterworth filter. The description and calculations above provide an clear understanding on designing a typical IIR filter. In this project, the practical design of the filter is realised by using the **butter** function in MATLAB with a given number of order and the desired cut-off frequency related to the frequency of the fundamental frequency component. Once the transfer function of the IIR filter is obtained, it can be applied as the impulse response function in the convolution process of the proposed CMF.

5.1.3 Finite Impulse Response Function

In order to design a finite impulse response (FIR) filter, selecting coefficients such that the system has specific characteristics is essential. The required properties are expressed in filter specifications and most of the time filter specifications refer to the frequency response of the filter [124]. There are different methods to find coefficients from frequency specifications for designing an FIR filter, such as window design method and frequency sampling method. In this section, window design method and frequency sampling method are introduced and discussed.

Window Design Method

In order to design a discrete FIR filter using the window design method, the first step is determining an ideal frequency response of the filter. The unit impulse response function can then be obtained through the inverse FT. Firstly, the practical frequency response of the desired FIR filter can be obtained through the designed window function. Moreover, the performance of the filter can be estimated based on the analysis of frequency response.

Assume that the frequency response of the ideal digital filter is $H_d(e^{\mathrm{j}\omega})$ and that of the designed digital filter is $H(e^{\mathrm{j}\omega})$. The basic idea of this designing method is selecting a suitable window function, which makes the $H(e^{\mathrm{j}\omega})$ as similar to $H_d(e^{\mathrm{j}\omega})$ as possible.

For the purpose of designing the window function, the first procedure is to apply the inverse FT to $H_d(e^{\mathrm{j}\omega})$ and obtain the ideal unit impulse response $h_d(n)$. After processing the first step, a time-domain window $w(n)$ is added to $h_d(n)$, which becomes unit impulse response $h(n)$ of the proposed FIR filter. The whole progress can be expressed as:

$$\left.\begin{array}{l} h_d(n) = \frac{1}{2\pi}\int_{-\pi}^{\pi} H_d(e^{\mathrm{j}\omega})e^{\mathrm{j}\omega}\mathrm{d}\omega, \\ h(n) = w(n)h_d(n). \end{array}\right\} \tag{5.1.46}$$

Let $x(n)$ and $X(e^{\mathrm{j}\omega})$ be the input of the filter and $y(n)$ and $Y(e^{\mathrm{j}\omega})$ be the output of the filter, the transfer function of the filter can be expressed as:

$$\left.\begin{array}{l} y(n) = x(n) * h(n) = x(n) * [w(n) \cdot h_d(n)], \\ Y(e^{\mathrm{j}\omega}) = X(e^{\mathrm{j}\omega}) \cdot H(e^{\mathrm{j}\omega}) \\ = X(e^{\mathrm{j}\omega}) \cdot [H_d(e^{\mathrm{j}\omega}) * W(e^{\mathrm{j}\omega})]. \end{array}\right\} \tag{5.1.47}$$

In the following part, rectangular window is chosen as an example to reveal the influence of the window function to an ideal digital low pass filter.

Assuming the frequency response $H_d(e^{\mathrm{j}\omega})$ of the ideal digital low pass filter is given as:

$$H_d(e^{\mathrm{j}\omega}) = \begin{cases} |H_d(e^{\mathrm{j}\omega})|e^{\mathrm{j}\theta\omega} = e^{-\mathrm{j}\omega a}, & (-\omega_c \le \omega \le \omega_c) \\ 0. & (\omega_c < |\omega| \le \pi) \end{cases} \tag{5.1.48}$$

where a indicates the delay, ω_c indicates the cut-off frequency.

By applying inverse discrete-time FT, the unit impulse response of the ideal digital low pass filter is obtained:

$$\begin{aligned} h_d(n) &= \mathrm{DTFT}^{-1}[H_d(e^{\mathrm{j}\omega})] \\ &= \frac{1}{2\pi}\int_{-\omega_c}^{\omega_c} e^{-\mathrm{j}\omega a}e^{-\mathrm{j}\omega n}d\omega \\ &= \frac{\omega_c}{\pi}\frac{\sin[(n-a)\omega_c]}{(n-a)\omega_c}. \end{aligned} \tag{5.1.49}$$

Because the phase is $\theta(\omega) = -\omega a$, the $h_d(n)$ is even symmetry and its centre of symmetry is a. When $n = a$, $h_d(a) = \omega_c/\pi$ reaches its maximum value. Applying the window function to the unit impulse response can be regarded

as a multiplication operation, which directly "cuts off" the data. Let $\omega_R(n)$ be the rectangular window, and applying the window to $h_d(n)$, $h(n)$ becomes:

$$h(n) = h_d(n)w_R(n) = \begin{cases} h_d(n), & (0 \le n \le N-1) \\ 0. & (n < 0,\ n > N-1) \end{cases} \tag{5.1.50}$$

Since the $h(n)$ is an even symmetry sequence, when N is the length of $h(n)$ the centre of symmetry becomes $a = (N-1)/2$. Therefore, $h(n)$ is written as:

$$h(n) = \begin{cases} \frac{\omega_c}{\pi} \cdot \frac{\sin\left[\left(n-\frac{N-1}{2}\omega_c\right)\right]}{\left(n-\frac{N-1}{2}\right)\omega_c}, & (0 \le n \le N-1) \\ 0. & (n < 0,\ n > N-1) \end{cases} \tag{5.1.51}$$

The frequency response $H(e^{\mathrm{j}\omega})$ is obtained from $h(n)$ through the discrete-time FT, presented as:

$$H(e^{\mathrm{j}\omega}) = \mathrm{DTFT}[h(n)]. \tag{5.1.52}$$

Meanwhile, in order to easily compare with $H_d(e^{\mathrm{j}\omega})$, $H(e^{\mathrm{j}\omega})$ is expressed as:

$$H(e^{\mathrm{j}\omega}) = H_d(e^{\mathrm{j}\omega}) * W_d(e^{\mathrm{j}\omega}) = \frac{1}{2\pi}\int_{-\pi}^{\pi} H_d(e^{\mathrm{j}\theta})W_d(e^{\mathrm{j}(\omega-\theta)})d\theta \tag{5.1.53}$$

In the above equation, $W_R(e^{\mathrm{j}\omega})$ is the frequency response of the rectangular window, which is derived from:

$$\begin{aligned} W_R(e^{\mathrm{j}\omega}) &= \mathrm{DTFT}[w_R(n)] = \sum_{n=0}^{N-1} w_R(n)e^{-\mathrm{j}\omega n} \\ &= \frac{\sin\frac{\omega N}{2}}{\sin\frac{\omega}{2}} e^{-\mathrm{j}\omega\left(\frac{N-1}{2}\right)} \\ &= W_R(\omega)e^{-\mathrm{j}\omega\left(\frac{N-1}{2}\right)}, \end{aligned} \tag{5.1.54}$$

where $W_R(\omega) = \sin\left(\frac{\omega N}{2}\right) / \sin\left(\frac{\omega}{2}\right)$ is the amplitude function. The rectangular window function consists of a major part and several small parts. The phase function is expressed as $\varphi(\omega) = -\left(\frac{N-1}{2}\right)\omega$.

Therefore, combining the two equations above, the frequency response of the designed FIR filter is:

$$H(e^{\mathrm{j}\omega}) = \frac{1}{2\pi}\int_{-\pi}^{\pi} |H_d(\theta)|e^{-\mathrm{j}\left(\frac{N-1}{2}\right)\theta}W_R(\omega-\theta)e^{-\mathrm{j}\left(\frac{N-1}{2}\right)(\omega-\theta)}d\theta$$

$$
\begin{aligned}
&= e^{-\mathrm{j}\left(\frac{N-1}{2}\right)\omega} \cdot \frac{1}{2\pi} \int_{-\pi}^{\pi} |H_d(\theta)| W_R(\omega-\theta) d\theta \\
&= e^{-\mathrm{j}\left(\frac{N-1}{2}\right)\omega} \cdot \frac{1}{2\pi} \int_{-\pi}^{\pi} W_R(\omega-\theta) d\theta, \qquad (5.1.55)
\end{aligned}
$$

where $H(\omega) = \frac{1}{2\pi}\int_{-\pi}^{\pi} |H_d(\theta)| W_R(\omega-\theta) d\theta$ is the amplitude function, and $\varphi(\omega) = -\left(\frac{N-1}{2}\right)\omega$ is the phase function.

The procedure for the implementation of FIR using window design method can be summarised as:

1. Design the ideal frequency response of $H_d(e^{\mathrm{j}\omega})$;
2. Calculate the unit impulse response $h_d(n) = F^{-1}[H_d(e^{\mathrm{j}\omega}]$;
3. Based on the width of excessive band and minimal reduction on stop band, find the type of the window and determine N;
4. Calculate $h(n) = h_d(n)w(n)$ or $H(e^{\mathrm{j}\omega})$.

Frequency Sampling Method

Different from the window design method, the frequency sampling method, which is analysed in the frequency domain, applies equal interval sampling to the ideal frequency response $H(e^{\mathrm{j}\omega})$ and makes the limited sampling frequency response $H_d(k)$ as similar to ideal frequency response $H(e^{\mathrm{j}\omega})\mid_{\omega=\frac{2\pi}{N}k}$ as possible.

Let $H(k)$ be the frequency response sampling values and N be the number of frequency sampling points of the FIR filter, the system function of the filter is expressed as:

$$
H(z) = \frac{1}{N}(1-z^{-N}) \sum_{k=0}^{N-1} \frac{H(k)}{1-W_N^{-k} z^{-1}}. \qquad (5.1.56)
$$

The corresponding frequency response is shown as follows:

$$
H(e^{\mathrm{j}\omega}) = \sum_{k=0}^{N-1} H(k)\phi_k(e^{\mathrm{j}\omega}), \qquad (5.1.57)
$$

where the interpolation function $\phi_k(e^{\mathrm{j}\omega})$ is:

$$
\phi_k(e^{\mathrm{j}\omega}) = \phi(\omega - \frac{2\pi}{N}k) = \frac{1}{N} \frac{\sin\frac{N\omega}{2}}{\sin\left[\frac{1}{2}\left(\omega - \frac{2\pi}{N}k\right)\right]} e^{-\mathrm{j}\left(\frac{N-1}{2}\omega + \frac{k\pi}{N}\right)}. \qquad (5.1.58)
$$

Eqn. (5.1.56) and Eqn. (5.1.57) show that the system function and frequency response of the FIR filter can be calculated by $H(k)$.

According to the theory of sampling in the frequency domain, the values of frequency sampling points can only identify the unit impulse response $h(n)$, which also can be regarded as applying the inverse discrete FT to $H(k)$, and the $h(n)$ is given as:

$$h(n) = \frac{1}{N}\sum_{k=0}^{N-1} H(k)e^{\mathrm{j}\cdot 2\pi nk/N}.(n = 0, 1, \cdots, N-1) \tag{5.1.59}$$

There are some constraint conditions for linear phase in designing FIR filters. Considering the situation where $h(n)$ is even symmetry and N is odd, the analysis of constraint conditions for linear phase are illustrated as follows.

The general expression for linear phase frequency response of FIR filters is given as:

$$H(e^{\mathrm{j}\omega}) = H(\omega)e^{-\mathrm{j}\left(\frac{N-1}{2}\right)^{\omega}}. \tag{5.1.60}$$

In this condition, the amplitude function $H(\omega)$ is even symmetry with a cycle of 2π. Therefore, it can be expressed as:

$$H(\omega) = H(2\pi - \omega). \tag{5.1.61}$$

Assume the numerical frequency on the sampling points is:

$$\omega_k = \frac{2\pi}{N}k. \tag{5.1.62}$$

As a consequence, the frequency response on the sampling points becomes:

$$H(k) = H\left(e^{\mathrm{j}\frac{2\pi}{N}k}\right) = H\left(\frac{2\pi}{N}k\right)e^{-\mathrm{j}\frac{N-1}{2}\cdot\frac{2\pi}{N}k} = H_k e^{\mathrm{j}\theta_k}, \tag{5.1.63}$$

where $H(k) = H\left(\frac{2\pi}{N}k\right)$ is the sampling value of the amplitude function and θ_k is phase angle. The phase angle can be further shown as:

$$\theta_k = -\frac{N-1}{2}\frac{2\pi}{N}\cdot k = -k\pi\left(1 - \frac{1}{N}\right). \tag{5.1.64}$$

Eqn. (5.1.64) demonstrates that on the sampling points $H(k)$ has the constraints conditions for linear phase and the even symmetry can be simplified as:

$$H(k) = H_{N-k}. \tag{5.1.65}$$

The procedure for the implementation of FIR using frequency sampling method can be listed as:

1. According to the desired characteristics, obtain the plot of the frequency sampling sequence;
2. Make the process simpler referring to the symmetry character of $\mid H_k \mid$;
3. Calculate θ_k according to the constraint conditions of linear phase;
4. Substitute $H(k) = H_k e^{j\theta_k}$ into frequency response expression of FIR;
5. Obtain the practical frequency response from the expression of $H(k)$.

Similarly, these descriptions of the two methods introduce the calculations and knowledge on designing an FIR filter. While in this project, it is realised by using the MATLAB signal processing toolbox to obtain the impulse response function for the convolution process in CMF.

A 68^{th}-order bandpass FIR filter is applied in **fir2** function as shown below. This filter is designed to preserve the signal with 50 Hz and Hanning window function is selected as the window function. Moreover, the sampling rate is set to 1 kHz, which means there are 20 sampling points in each cycle.

```
L=69;                                  %Window length
N=L-1;                                 %Order of the filter
f=[0  0.04  0.06  0.16  0.18  1];      %Normalised frequency
m=[0  0  1  1  0  0];                  %Amplitude-frequency characteristic value
b=fir2(N,f,m,hanning(L));              %Design a 68^th-order filter
[h,w]=freqz(b,1,512,1000);             %Calculate the frequency response
freqz(b,1,512,1000);                   %Plot the amplitude-frequency response
Yo=filter(b,1,sgn);                    %Filtering the input signal
```

With this design expressed above, the magnitude and frequency response characteristics of the specific FIR filter are shown in Fig. 5.2.

In order to extract different frequencies of harmonics in the signal, different normalised frequency must be applied. These normalised frequency are selected as shown below and these will be applied in CMF using FIR as the impulse response

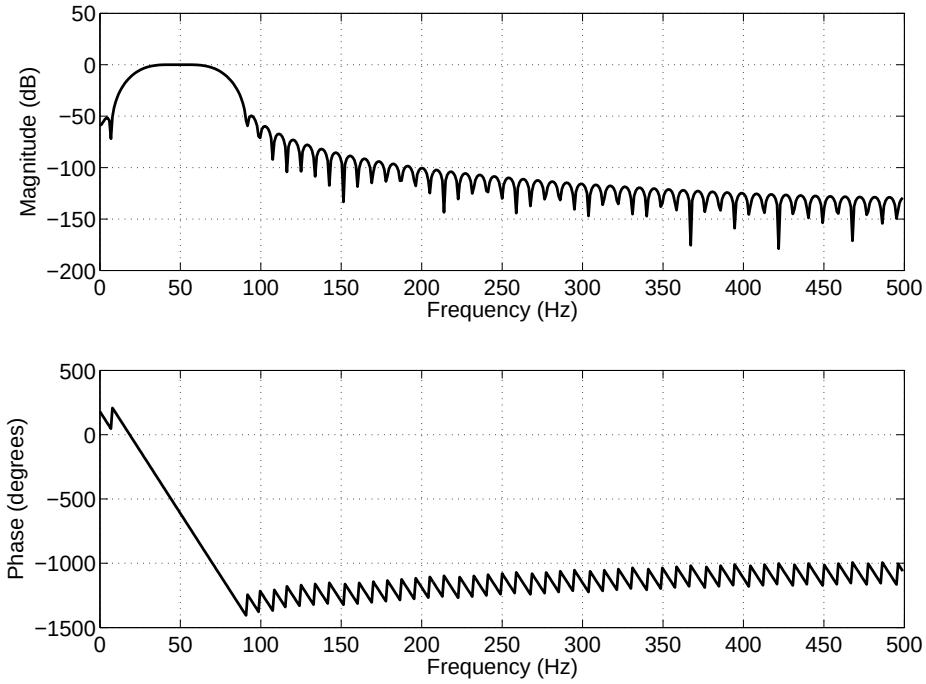

Figure 5.2: The magnitude response and frequency response of the designed FIR filter for extracting the 50 Hz fundamental component

function.

```
f=[0  0.14  0.16  0.24  0.26  1];  %Normalised frequency for 100 Hz harmonic
f=[0  0.24  0.26  0.36  0.38  1];  %Normalised frequency for 150 Hz harmonic
f=[0  0.34  0.36  0.44  0.46  1];  %Normalised frequency for 200 Hz harmonic
f=[0  0.44  0.46  0.54  0.56  1];  %Normalised frequency for 250 Hz harmonic
f=[0  0.54  0.56  0.64  0.66  1];  %Normalised frequency for 300 Hz harmonic
```

5.1.4 Sinc Function

Sinc function was introduced by Woodward in his 1952 paper "Information theory and inverse probability in telecommunication" [125]. In mathematical terms, the impulse response function and transfer function of a normalised sinc function are given by:

$$h_s(t) = 2f_0\text{sinc}(2f_0t), \tag{5.1.66}$$

$$H_s(f) = \text{rect}\left(\frac{f}{2f_0}\right), \tag{5.1.67}$$

where f_0 is the cut-off frequency. According to the transfer function, in the frequency domain, the sinc function is a rectangular function and this property is desirable since its better roll-off characteristic. Usually, the sinc function can be applied as a sinc filter which is a brick-wall low-pass filter. The band-pass sinc filter is the direct subtraction of two sinc filters and its impulse response function is shown as:

$$h_{BPs}(t) = 2f_1\text{sinc}(2f_1t) - 2f_2\text{sinc}(2f_2t), \tag{5.1.68}$$

where f_1 and f_2 are upper band edge frequency and lower band edge frequency respectively. Similarly, its transfer function is given as:

$$H_{BPs}(f) = \text{rect}\left(\frac{f}{2f_1}\right) - \text{rect}\left(\frac{f}{2f_2}\right). \tag{5.1.69}$$

For the practical realisation, **sinc** function in MATLAB is utilised and it will be applied as the impulse response function in CMF using sinc function.

5.2 Implementation of Convolved Morphological Filters

After introducing four types of impulse response functions, the residual part of the implementation of the proposed CMF is given below. As introduced previously, the MF applied in the simulation is expressed as:

$$r(t) = \frac{[f_{\text{opcl}}(i(t)) + f_{\text{clop}}(i(t))]}{2}, \tag{5.2.1}$$

where $i(t)$ is the input target signal and $r(t)$ represents the output signal after using the MF. The SE, $g(t)$, is selected as a shape of half sinusoid with its peak at its center and the length of $g(t)$ is calculated as: $\frac{f_s/2}{f}$, where f_s is the sampling frequency. Furthermore, MF is applied again to $r(t)$. In the second process of MF, the length of SE is increased to $\frac{f_s/2}{f'}$, where $f' < f$. Thus, the complete operation for the low-pass MF is shown below:

$$f_{\text{low}}(t) = \frac{[f_{\text{opcl}}(r(t)) + f_{\text{clop}}(r(t))]}{2}, \tag{5.2.2}$$

where $f_{\text{low}}(t)$ is regarded as the low-pass MF. Once the signal is filtered by MF, the next procedure is to apply the convolution to the signal with a pre-selected $h(t)$, and the convolution is expressed as:

$$f_{\text{cmf}}(t) = \sum_{\tau} h(\tau) \cdot f_{\text{low}}(t - \tau), \tag{5.2.3}$$

where $f_{\text{cmf}}(t)$ generates the output signal of CMF.

5.3 Simulation Studies

In the simulations, the performance of the proposed CMF with different impulse response functions in the convolution process have been tested. Note that all the simulation studies are carried out on a Dell PC with 3.4 GHz Intel Core i7-2600 CPU and 8.00 GB RAM using MATLAB 2015a. The corresponding results are presented in each section, respectively.

5.3.1 Harmoincs Removal Results of CMF using Dirac Delta Functions

In this section, two cases are simulated and discussed in order to evaluate the validity of the proposed CMF using Dirac delta function as the impulse response function. The first scenario intends to identify the effectiveness of CMF when the frequencies of the input signal and the harmonic component are both small and the second scenario investigates the performance of CMF when applied to synthetic power system signals containing the third harmonic component. For the purpose of comparison, the filtering results of the low-pass MF are obtained to verify the superiority of CMF. Moreover, in both cases, WGN pollutes the environment with an SNR of 30 dB.

Scenario I

In this scenario, a synthetic signal, where the sampling frequency $f_s = 128$ Hz, is generated according to the equation, given as:

$$i(t) = \cos(2\pi \cdot 5 \cdot t) + \cos(2\pi \cdot 20 \cdot t). \tag{5.3.1}$$

The corresponding waveform and spectrum of the input signal are illustrated in Fig. 5.3. It is obvious that the input signal contains a fundamental frequency component of 5 Hz and a harmonic component of 20 Hz.

For the purpose of maintaining the fundamental frequency component with 5 Hz, the SE $g_1(t)$ in the first process of designing the MF is selected to be a shape of half sinusoid with its peak at its centre. The length of $g_1(t)$ is calculated as:

$$l_{g_1} = \lfloor \frac{f_s/2}{5} \rfloor = 12.8 \simeq 13. \tag{5.3.2}$$

Correspondingly, the length of the SE $g_2(t)$ in the second process of MF is selected as $\frac{f_s/2}{4} = 16$. In this situation, $h(t)$ is calculated as:

$$h(t) = 2\sqrt{\pi} \cdot e^{-\pi^2 t^2} \cdot \cos(2\pi \cdot 5 \cdot t). \tag{5.3.3}$$

After the convolution, the output signal is expressed as:

$$o(t) = \sum_{\tau} h(\tau) \cdot f_{\text{low}}(t - \tau), \tag{5.3.4}$$

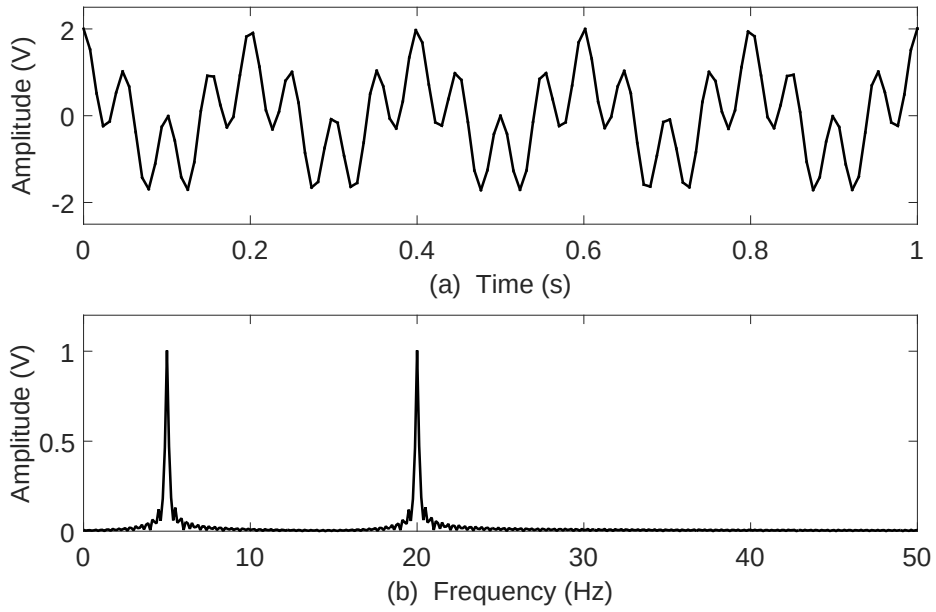

Figure 5.3: The waveform and spectrum of the input signal

where the range of τ is from -0.4 to 0.4. This integral range covers approximately 5 cycles of the output signal of MF. The waveforms of the signals filtered by MF and the proposed CMF are shown in Fig. 5.4. The corresponding spectra of the output signals of MF and CMF are illustrated in Fig. 5.5.

As can be observed from these figures, the waveform of $o(t)$ is more similar to sinusoidal wave compared to that of the signal after the MF since its waveform is slightly warped at peaks. Moreover from their spectra, the signal after the MF contains other frequency components and this is the reason that causes the slight bending at peaks. Furthermore, referring to these figures, there are still some problems of CMF. Firstly, the output signal is magnified after convolution. Secondly, with the increase in amplitude, the bandwidth of the proposed CMF also increases to some extent.

In order to make the proposed CMF more understandable, the convolution process is illustrated in Fig. 5.6. As known, the convolution of two functions in the time domain is their multiplication in the frequency domain. As a consequence, some of undesired components, such as noise and harmonics, can be mostly removed

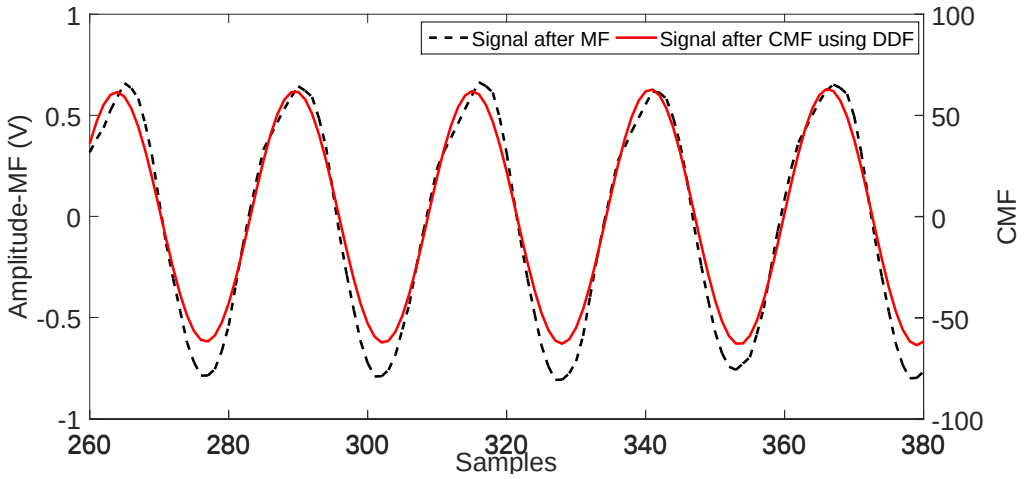

Figure 5.4: The waveforms of the signal after MF and the signal after CMF using the Dirac delta function ($-0.4 < \tau < 0.4$)

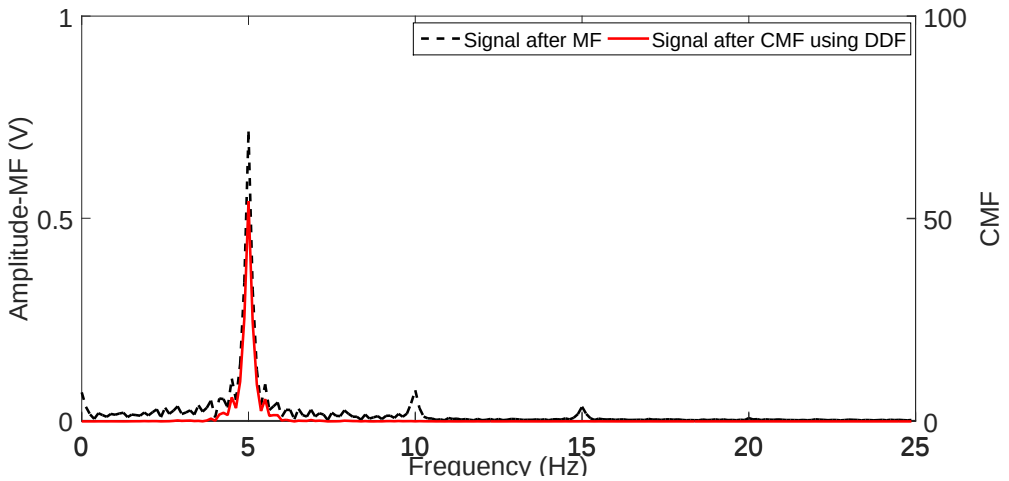

Figure 5.5: The spectra of the signal after MF and the signal after CMF using the Dirac delta function ($-0.4 < \tau < 0.4$)

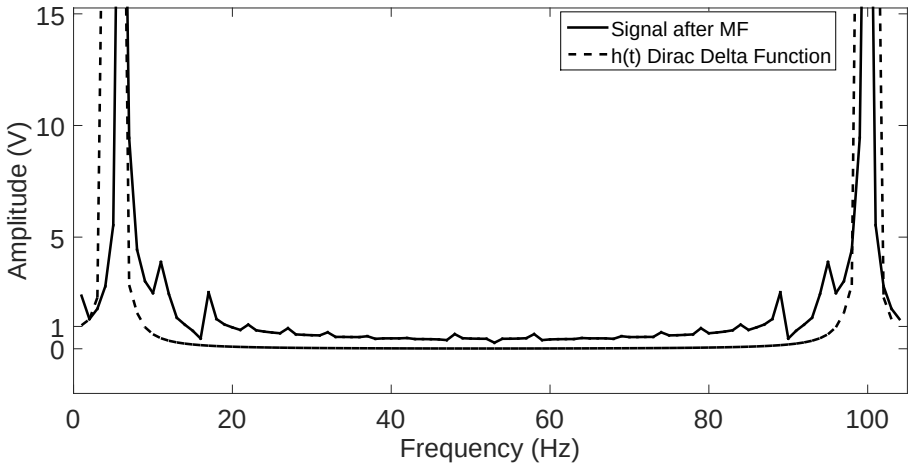

Figure 5.6: The spectra of the signal after MF and $h(t)$

after convolution. However, $h(t)$ is not narrow enough and the components, both wanted and unwanted, are amplified after the multiplication in the frequency domain. Therefore, it is necessary to adjust the width of $h(t)$ in order to improve the performance of the CMF and this will be further analysed in the following section.

Scenario II

As known, harmonic pollution influences the power quality badly and the third harmonic is normally one of the problematic harmonics in electric power networks [90]. Therefore, in scenario II, the signal consisting of a basic power frequency of 50 Hz and a third harmonic with 150 Hz frequency is estimated and the sampling frequency f_s is 6.4 kHz. The synthetic input signal is expressed as:

$$i(t) = 50\cos\left(2\pi \cdot 50 \cdot t\right) + 3\cos\left(2\pi \cdot 150 \cdot t\right). \tag{5.3.5}$$

The relative waveform and spectrum of the input signal are illustrated in Fig. 5.7.

Similarly, the SE $g_1(t)$ in the first process of MF is selected to be a shape of half sinusoid with its peak at its centre. The length of $g_1(t)$ is calculated as:

$$l_{g_1} = \lfloor \frac{f_s/2}{50} \rfloor = 64. \tag{5.3.6}$$

Accordingly, the length of the SE $g_2(t)$ in the second process of MF is selected as

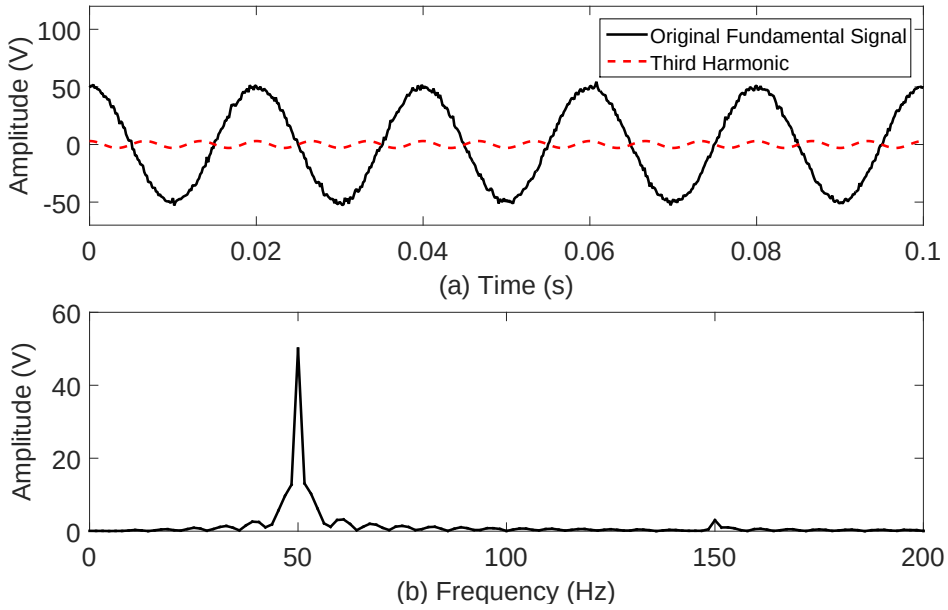

Figure 5.7: (a) The waveforms of the original fundamental signal and the third harmonic (b) The spectrum of the input signal

$\frac{f_s/2}{40} = 80$. In this scenario, $h(t)$ is estimated as:

$$h(t) = 2\sqrt{\pi} \cdot e^{-\pi^2 t^2} \cdot \cos(2\pi \cdot 50 \cdot t). \tag{5.3.7}$$

After the convolution, the output signal is expressed as:

$$o(t) = \sum_{\tau} h(\tau) \cdot f_{\text{low}}(t - \tau), \tag{5.3.8}$$

where the range of τ is from -0.05 to 0.05, which covers approximately 5 cycles of the output signal. The waveforms of the output signals of MF and CMF are illustrated in Fig. 5.8 and the corresponding spectra of the output signals of MF and CMF are shown in Fig. 5.9.

As can be observed from these figures, the third harmonic in the target signal is removed to a large extent after using the proposed CMF. In comparison to the output signal after the proposed CMF, the result after the low-pass MF is not as good as the result of the CMF and severe distortion has occurred. In addition, according to the spectra, it even generates undesired frequency components, which further indicates that power system harmonics cannot be filtered out completely after morphological filtering under this circumstance. While the proposed CMF has

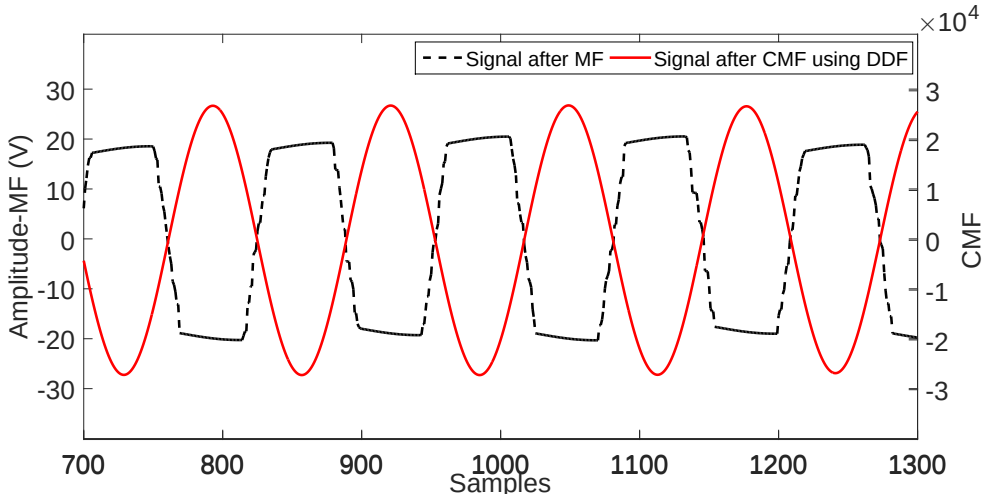

Figure 5.8: The waveforms of the signal after MF and the signal after CMF using Dirac delta function ($-0.05 < \tau < 0.05$)

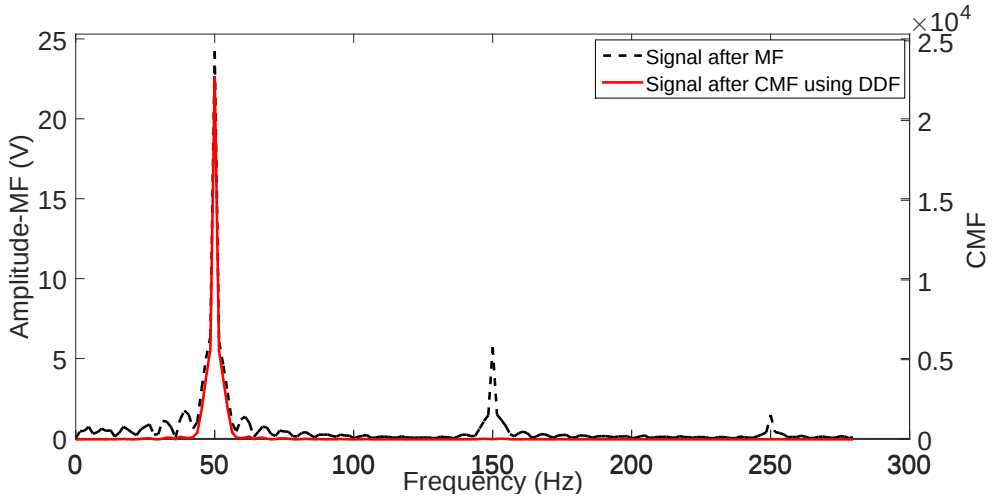

Figure 5.9: The spectra of of the signal after MF and the signal after CMF using Dirac delta function ($-0.05 < \tau < 0.05$)

achieve better performance in reducing the third harmonics and maintaining the fundamental frequency component. Various tests have been simulated by changing the amplitude and frequency, respectively, and similar results have been obtained. However, the amplitude has been increased dramatically due to the multiplication of input signal and the Dirac delta function in the frequency domain, which becomes the main drawback of the proposed CMF using Dirac delta function. For an ideal Dirac delta function as the impulse response function, the bandwidth is extremely narrow while the amplitude is infinitely large. In order to obtain narrower bandwidth of the CMF, the Dirac delta function in practical situation is designed with a narrow bandwidth, which consequently results in a large increase in amplitude. Therefore, it is necessary to find the balance between the desired bandwidth and the amplitude for better performance when using Dirac delta function in CMF. Due to this disadvantage of using Dirac delta function as the impulse response function, the applications of other types of impulse response function in CMF have been inspired.

5.3.2 Harmoincs Removal Results of CMF using IIR

In this section, the performance of the pre-designed IIR filter (Butterworth) is initially analysed, since the functionality of the IIR filter can reveal the performance of the convolution in CMF using IIR. Afterwards, the performance of CMF using both IIR and Dirac delta function are then simulated and the corresponding results are compared.

Scenario I: Results of the IIR filter

Firstly, the designed IIR filter is simulated and the corresponding filtering result is obtained in this section. The input signal consists of a basic power frequency of 50 Hz and a third harmonic with 150 Hz frequency, which is expressed as:

$$f(t) = \cos(2\pi \cdot 50\, t) + 0.2\cos(2\pi \cdot 150\, t). \tag{5.3.9}$$

In this situation, WGN is not added into the input signal. The IIR filter only aims to filter out the third harmonic component in the input signal.

A third-order low-pass filter is applied in the **butter** function in MATLAB as shown below. The sampling rate is set to 3.2 kHz in this scenario, which means there are 64 sampling points in each cycle.

```
[z,p,k] = butter(3,150/3200,'low');
[sos,g] = zp2sos(z,p,k);                % Convert to SOS form
Hd = dfilt.df2tsos(sos,g);              % Create a dfilt object
h = fvtool(Hd);                         % Plot magnitude response
set(h,'Analysis','freq')                % Display frequency response
```

The magnitude response and frequency response of the designed IIR filter are illustrated in Figure 5.10. The input signal and the output signal after using the IIR

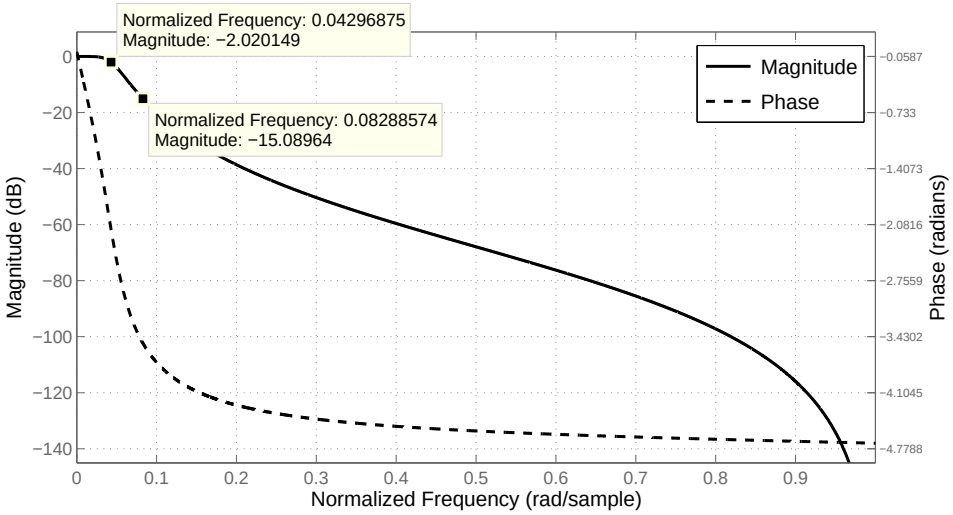

Figure 5.10: The magnitude response and frequency response of the designed IIR filter (Butterworth)

filter are shown in Fig. 5.11.

As mentioned previously, the amplitude of the output signal is enlarged greatly when using CMF with the Dirac delta function, since the amplitude of its transfer function, $h(t)$, is set to be very large. The IIR filter can almost remain or slightly reduced the amplitude of the input signal according to the result in Fig. 5.11. However, the time delay of the IIR filter is clearly observed. Although the Dirac delta function is able to reduce the time delay of CMF, it will largely increase the amplitude. For CMF using the Dirac delta function, the delay is caused by the length of $h(t)$. While, for the IIR filter, time delay is related to the order of it. Without restricting the performance of the filter, a relatively small order can be selected to reduce the time delay.

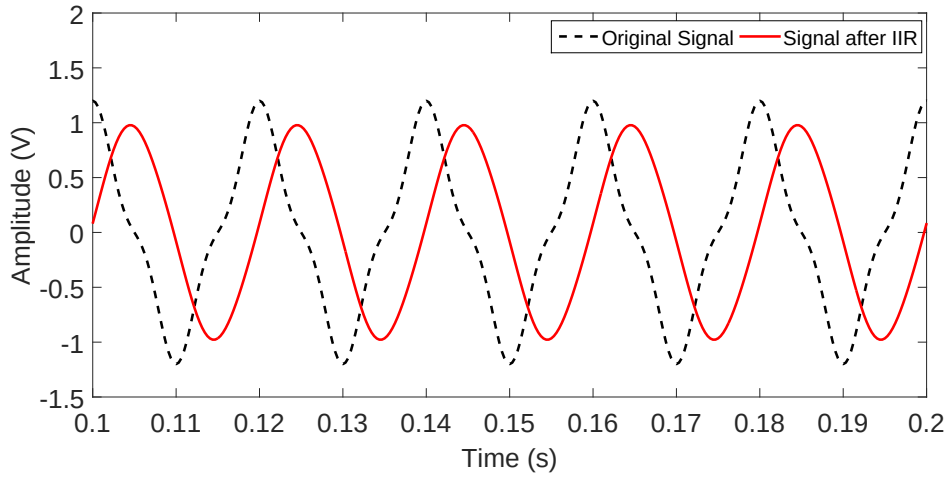

Figure 5.11: The waveforms of the input signal and the signal filtered by the IIR filter

Scenario II: Results of CMF using IIR

In this scenario, the performance of the CMF using IIR as the impulse response function is analysed. The sampling rate is also set to 3.2 kHz and the input signal consists of a basic power frequency of 50 Hz and a third harmonic with 150 Hz frequency, which is expressed as:

$$f(t) = 100\cos(2\pi \cdot 50\,t) + 30\cos(2\pi \cdot 150\,t). \tag{5.3.10}$$

Comparing with the previous situation, the environment is polluted by a WGN with SNR of 30 dB.

For the purpose of detection and extraction of the signal with 50 Hz frequency, the SEs $g1(t)$ and $g2(t)$ are selected to be a shape of half sinusoid with its peak at its center. The length of $g1(t)$ is calculated as:

$$\lfloor \frac{f_s/2}{50} \rfloor = 32. \tag{5.3.11}$$

The MF low-pass filter is applied twice to the input signal and the length of the SE $g_2(t)$ in the second process of MF is selected as $\frac{f_s/2}{40} = 40$ in order to remove WGN and partial third harmonic component. The residue signal is then convolved with $h(t)$ with the pre-designed IIR. Both the waveforms and spectra are shown in Fig. 5.12 and Fig. 5.13 respectively.

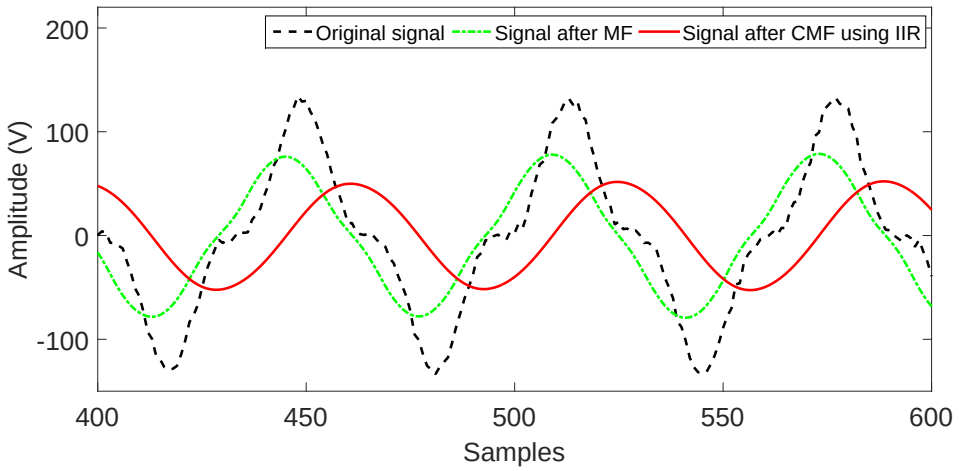

Figure 5.12: The waveforms of the input signal with 30 dB WGN, the signal after MF and the signal after CMF using IIR

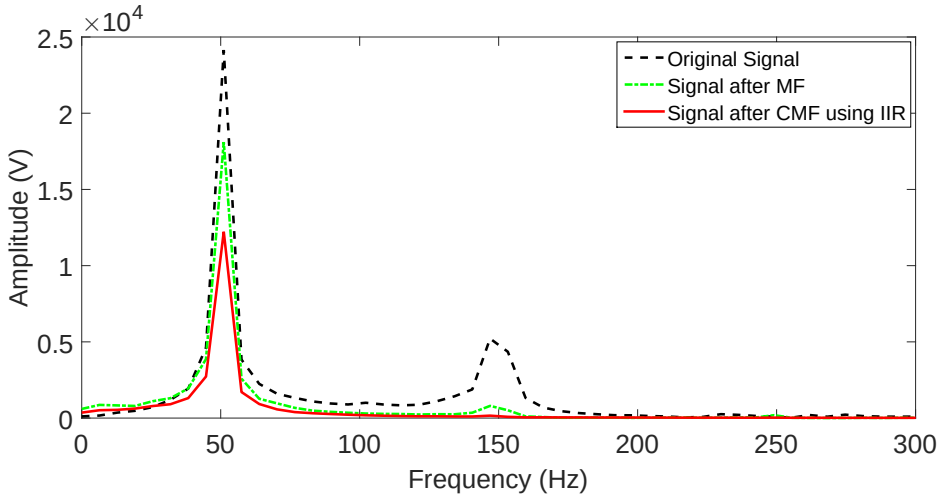

Figure 5.13: The spectra of the input signal with 30 dB WGN, the signal after MF and the signal after CMF using IIR

Referring to Fig. 5.12, the amplitude of the signal after the MF is reduced. After filtering by the proposed CMF, the amplitude continues reducing. A slight distortion on the waveform after the MF can also be observed. From the spectra of these signals, it can be found out that the majority of the third harmonic is removed by the MF. However, the proposed CMF using IIR can further reduce the third harmonic. Moreover, the extremely low frequency noise caused by the MF is also reduced to some extent by the convolution process.

The performance of the CMF using IIR is then compared with that of CMF using Dirac delta function. The waveforms and spectra of CMF using Dirac delta function and IIR are shown in Fig. 5.14 and Fig. 5.15 respectively. As can be observed from these figures, the time delay is much more obvious when using CMF with IIR. However, the amplitude of the signal is dramatically enlarged after CMF using Dirac delta function, while after CMF using IIR, the amplitude of the signal is slightly reduced. These phenomena are similar to the ones carried out in the previous section on the performance of IIR filter.

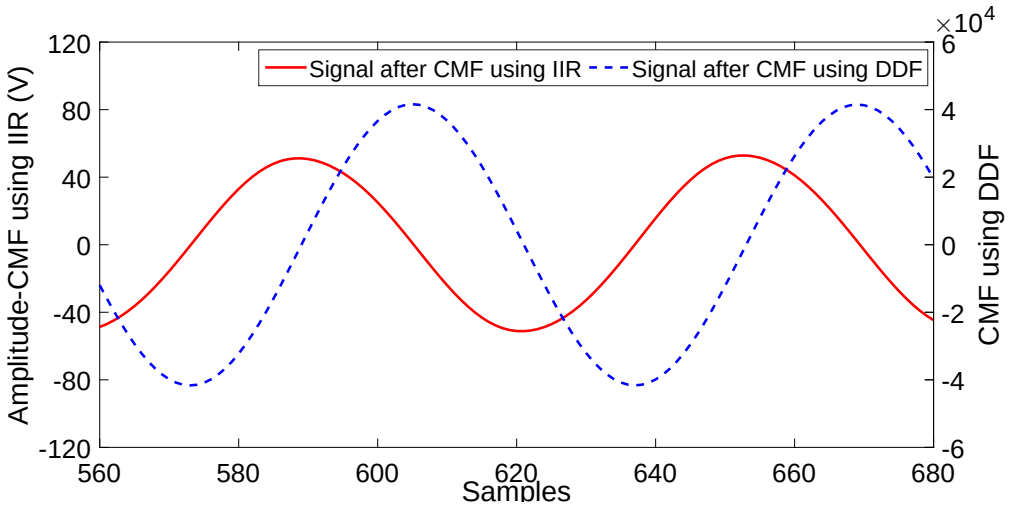

Figure 5.14: The waveforms of the signal after CMF using IIR and the signal after CMF using Dirac delta function

Furthermore, observed from characteristics of these two CMF, CMF using Dirac delta function can detect and extract desired signal with a narrower range of frequencies while CMF using IIR can pass through a wider range one. Therefore, for different and specific applications, different approaches can be chosen. For appli-

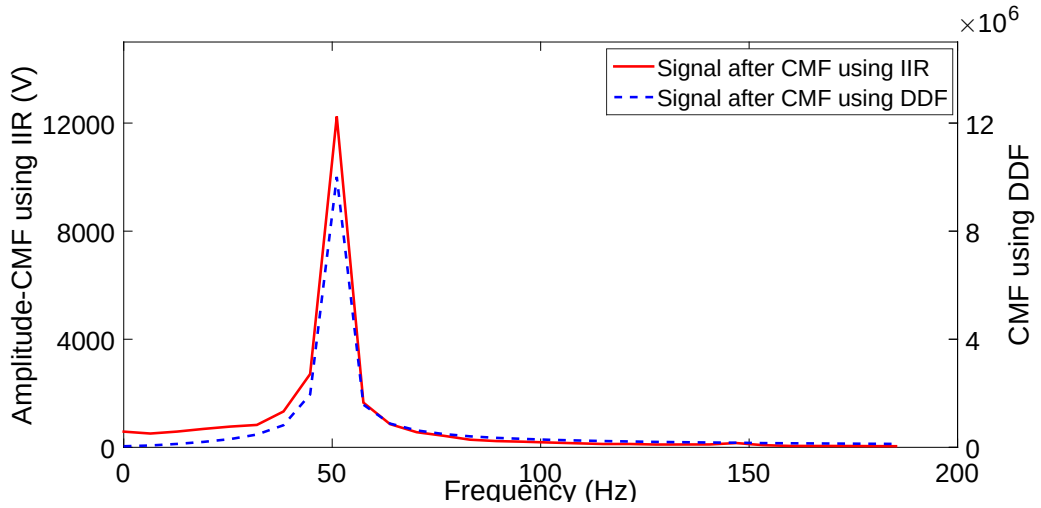

Figure 5.15: The spectra of the signal after CMF using IIR and the signal after CMF using Dirac delta function

cations which need to process the signal with a wider range of frequencies, such as sound/voice processing and image processing, CMF using IIR is preferred. However, in order to filter a specific frequency in signals, for example, harmonic analysis in power systems, CMF using Dirac delta function is more suitable. While in this situation, the amplitude of the output signal should be decreased for safety concern.

5.3.3 Harmoincs Removal Results of CMF using FIR

In this section, the performance of the proposed CMF with a pre-designed FIR as the impulse response function is simulated and analysed. A 30 dB WGN environment is considered and the sampling frequency is 1 kHz.

The input signal consists of a basic power frequency of 50 Hz and different harmonic components of 100 Hz, 150 Hz, 200 Hz, 250 Hz and 300 Hz, which is expressed as:

$$i(t) = 220\sin(2\pi \cdot 50\,t) + 50\sin(2\pi \cdot 100\,t) + 25\sin(2\pi \cdot 150\,t) + 13\sin(2\pi \cdot 200\,t) + 10\sin(2\pi \cdot 250\,t) + 5\sin(2\pi \cdot 300\,t). \quad (5.3.12)$$

The waveform and spectrum of the input signal are shown in Fig. 5.16.

Firstly, the designed FIR filter is simulated. Secondly, the lengths and shapes of the SEs applied in the MF are determined. Similarly, the SEs $g1(t)$ and $g2(t)$ are

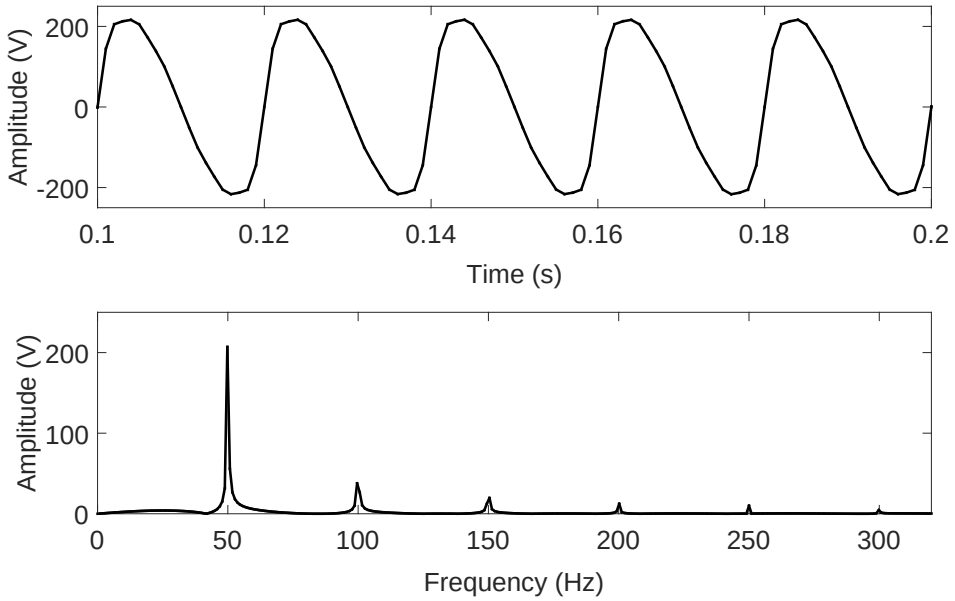

Figure 5.16: The waveform and spectrum of the input signal

selected to be a shape of half sinusoid with its peak at its center. The length of $g1(t)$ is calculated as:

$$\lfloor \frac{f_s/2}{50} \rfloor = 10. \tag{5.3.13}$$

The MF low-pass filter is applied twice to the input signal and the length of the SE $g_2(t)$ in the second process of MF is selected as $\frac{f_s/2}{40} \simeq 12$. As introduced previously, CMF using FIR is the convolution of the output signal of MF with $h(t)$ using FIR. Therefore, after applying MF, the pre-designed FIR filters are utilised aiming to detect and extract the fundamental frequency component of 50 Hz, and eliminate the residual harmonic components.

The waveform and spectrum of the output signal after applying the proposed CMF with FIR to extract 50 Hz fundamental signal are expressed in Fig. 5.17 and the waveform of the original fundamental signal and spectrum of the input signal are also shown as the comparison in the same plot. Fig. 5.17 depicts that the fundamental signal with 50 Hz is detected and extracted successfully and the residual harmonic components are eliminated accurately. Moreover, the WGN in the input signal is eliminated by applying the MF. However, there is time delay when

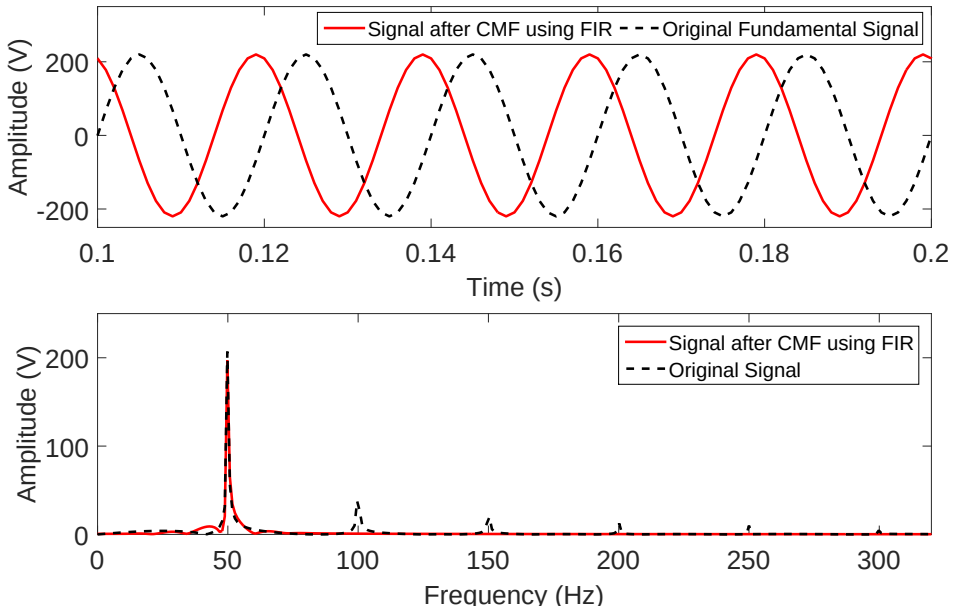

Figure 5.17: The waveforms and spectra of the original signal and the signal after CMF using FIR

applying the CMF using FIR and this time delay is also caused by the high order of FIR. Despite of the time delay, the amplitude of the extracted signal is almost the same as the fundamental one and harmonics in the signal are entirely removed. Therefore, it is also important to balance between the time delay and amplitude distortion when using CMF with FIR as the impulse response function.

The CMF using the Dirac delta function as the impulse response function in [101] is applied to the same input signal for maintaining the fundamental frequency component in the simulation. The results are demonstrated in Fig. 5.18 and Fig. 5.19. Apparently, the CMF using Dirac delta function has the ability to eliminate other undesired frequency components successfully and there still exists time delay when applying this approach. However, as mentioned in the introduction, the amplitude of the output signal increases dramatically using this method. From both figures, it is observed that the amplitude of the original signal is 220 while after the CMF using Dirac delta function it becomes more than 1×10^5. In practical situation, this huge rise of amplitude will result in the damage of electrical devices and equipment. Therefore, according to the comparison between CMF using FIR and CMF using

Dirac delta function, the CMF using FIR is more considerable and reliable to some extent.

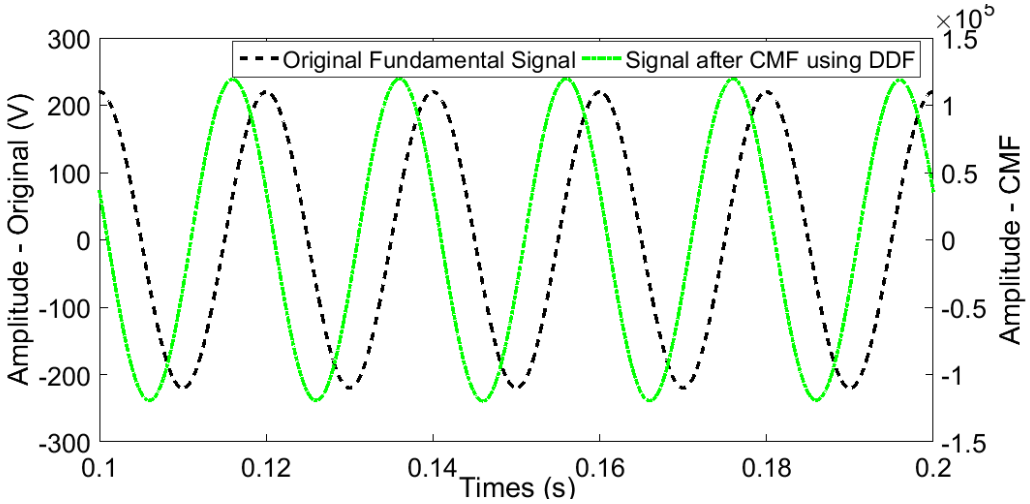

Figure 5.18: The waveforms of the original fundamental signal and the signal after CMF using Dirac delta function

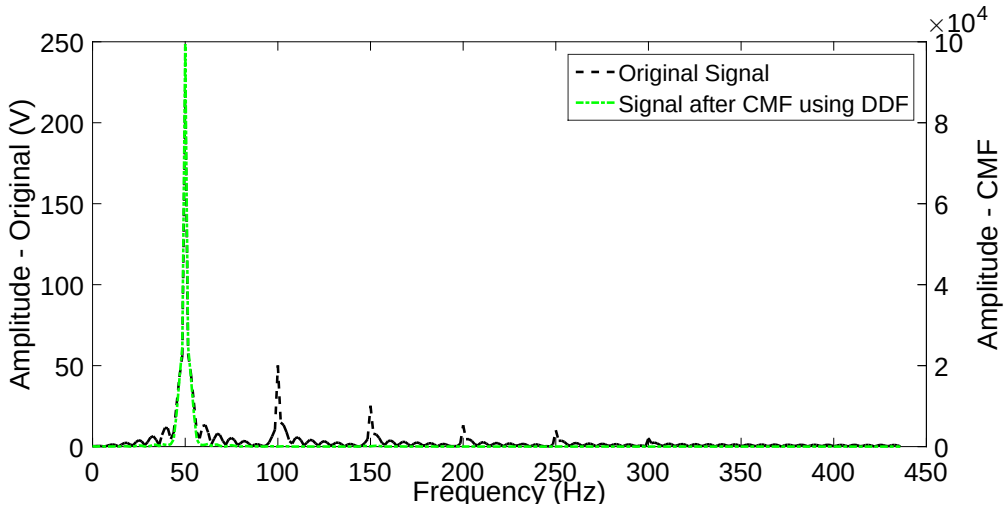

Figure 5.19: The spectra of the original signal and the signal after CMF using Dirac delta function

Through numerous simulations, CMF using FIR also has the ability to detect other frequency components in the input signal. Considering the same input signal as applied formerly and adjusting the normalized frequency in the pre-designed FIR

filter to detect and extract the 100 Hz harmonic component, the outcome is shown in Fig. 5.20. Similarly, the extracted harmonic signal of 100 Hz is approximately identical to the original one in amplitude with slight time delay. Moreover, other components in the input signal are completely suppressed and only the desired one maintains after using the proposed CMF with FIR.

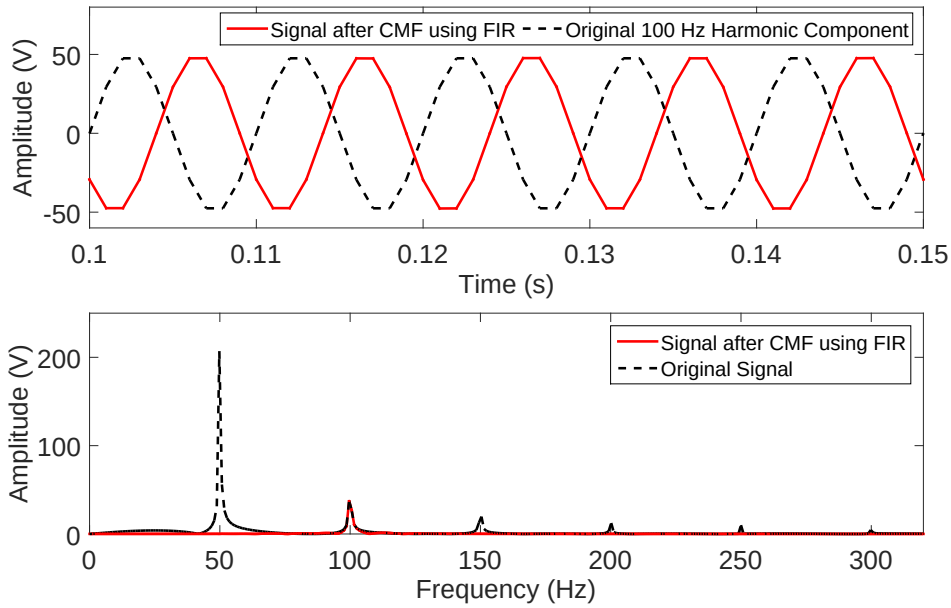

Figure 5.20: The waveforms and spectra of the original 100 Hz harmonic component and the signal after CMF using FIR to extract the harmonic component

Other harmonic components from 150 Hz to 300 Hz in the input signal are also extracted in turns by applying CMF using different normalised frequencies in FIR. The results are illustrated in Fig. 5.21 (150 Hz), Fig. 5.22 (200 Hz), Fig. 5.23 (250 Hz) and Fig. 5.24 (300 Hz) and similar outcomes are obtained. The irregular shape of the waveforms in these figures result from the low sampling frequency for high frequency harmonic component. However, these results have enough proved the robustness of the CMF using FIR in accurately extracting desired frequency components.

All the original amplitudes and the amplitudes of the extracted signals are recorded in Table 5.2. The accuracies of the detection and extraction by using the propose CMF with FIR are also demonstrated in it. The high precision of the extracting

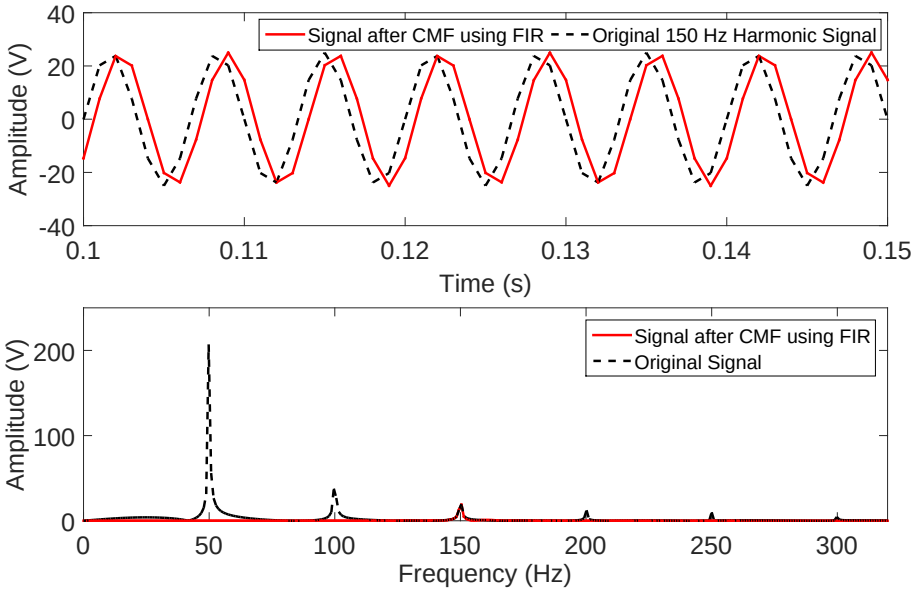

Figure 5.21: The waveforms and spectra of the original 150 Hz harmonic component and the signal after CMF using FIR to extract the harmonic signal of 150 Hz

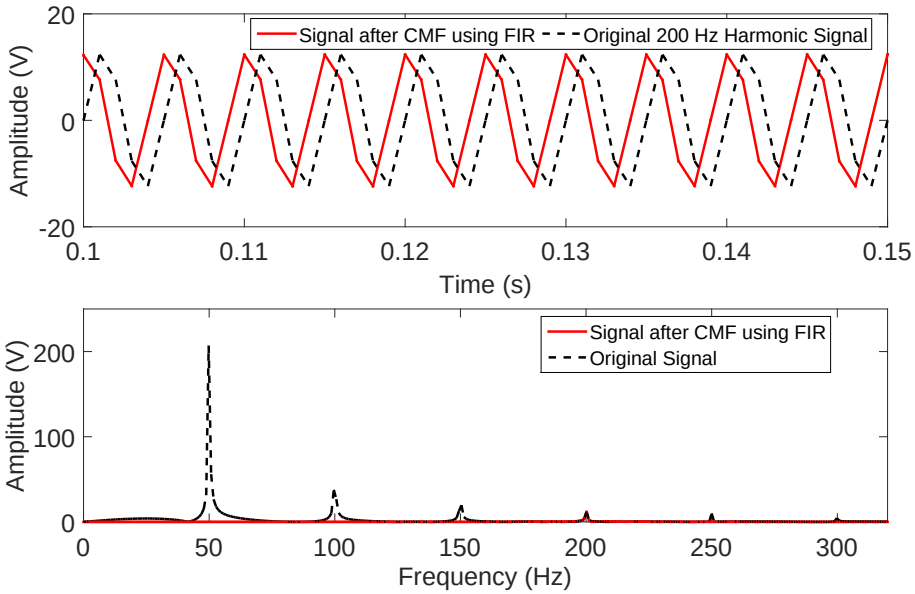

Figure 5.22: The waveforms and spectra of the original 200 Hz harmonic component and the signal after CMF using FIR to extract the harmonic component

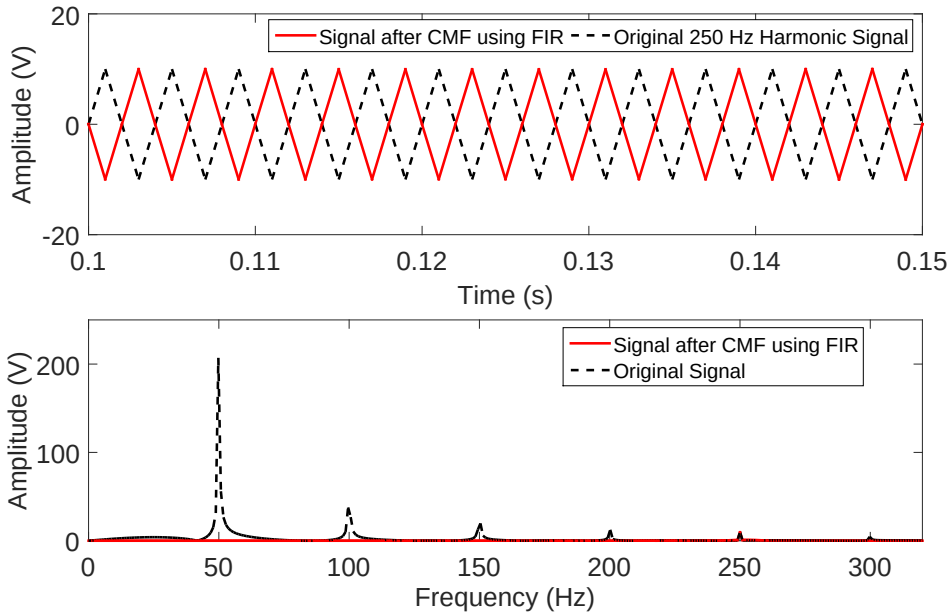

Figure 5.23: The waveforms and spectra of the original 250 Hz harmonic component and the signal after CMF using FIR to extract the harmonic component

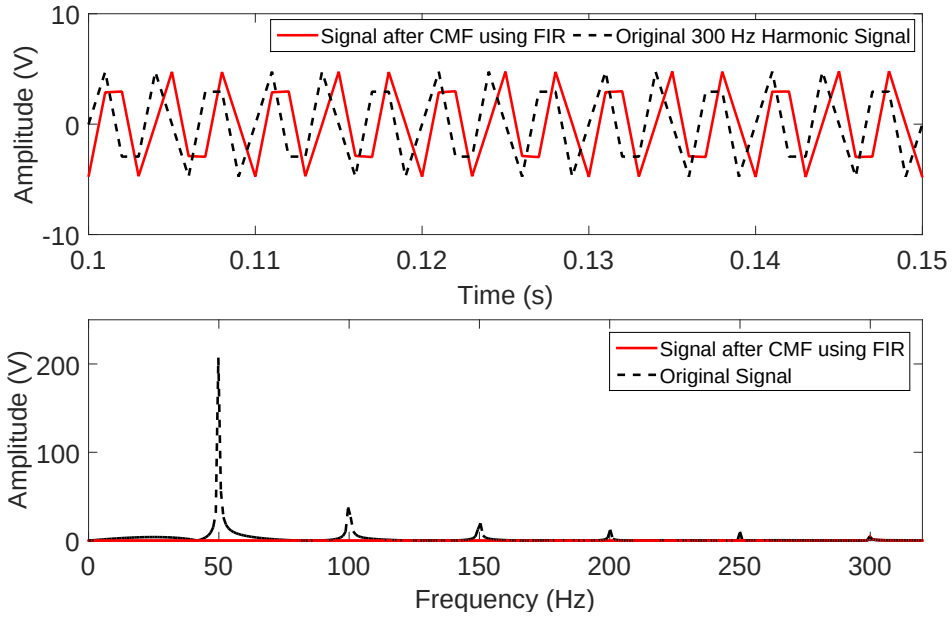

Figure 5.24: The waveforms and spectra of the original 300 Hz harmonic component and the signal after CMF using FIR to extract the harmonic component

signals with desired frequencies are clearly expressed. Furthermore, although the time delay exists when using this approach, the average accuracy is over 95% which is considerable in estimation of harmonics for analysis.

Table 5.2: Accuracy of Detection by Applying CMF using FIR

Desired Component	Original Amplitude	Practical Amplitude	Accuracy
50 Hz Fundamental	220	219.90	99.95%
100 Hz Harmonic	50	47.50	95.00%
150 Hz Harmonic	25	23.78	95.12%
200 Hz Harmonic	13	12.36	95.08%
250 Hz Harmonic	10	9.96	99.60%
300 Hz Harmonic	5	4.72	94.40%

From the simulation studies, the proposed CMF using the FIR can not only detect and eliminate harmonic components, but also has its merit in detecting and extracting different frequencies components from the input signal successfully and precisely, no matter the component is the fundamental frequency component or harmonic components. As introduced previously, with the extracted harmonic components, successful estimation on the parameters of harmonics in power systems for further harmonic analysis can be undertaken and the stability of power systems can be improved.

5.3.4 Harmoincs Removal Results of CMF using Sinc

In this section CMF using sinc function as the impulse response function is proposed and simulated. Furthermore, the comparison between the CMF using the sinc function and that using Dirac delta function are discussed in order to evaluate the performance of these two types of CMF. In the simulation studies, the sampling frequency f_s is 6.4 kHz and the environment is polluted by a WGN with SNR of 30 dB.

Similarly, in order to validate the effectiveness of these CMF when applied for filtering power system harmonics, the synthetic signal consisting of a basic power frequency of 50 Hz and a third harmonic with 150 Hz frequency is estimated. It is

expressed as below:

$$i(t) = 50\cos(2\pi \cdot 50 \cdot t) + 3\cos(2\pi \cdot 150 \cdot t)\,. \tag{5.3.14}$$

The waveform and spectrum of the input signal are illustrated in Fig. 5.25. Similarly,

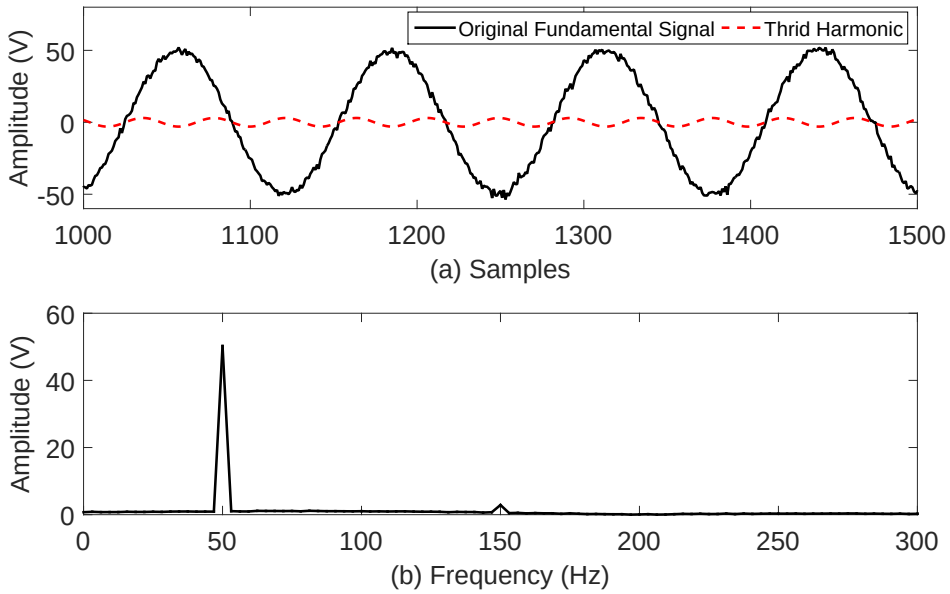

Figure 5.25: (a) The waveforms the original fundamental signal and the third harmonic (b) The spectrum of the input signal

for the purpose of maintaining the fundamental frequency component with 50 Hz frequency, the SE $g_1(t)$ in the first process of MF is also selected to be a shape of half sinusoid with its peak at its centre. The length of $g_1(t)$ is calculated as:

$$l_{g_1} = \lfloor \frac{f_s/2}{50} \rfloor = 64. \tag{5.3.15}$$

The corresponding length of the SE $g_2(t)$ in the second process of MF is selected as $\frac{f_s/2}{40} = 80$.

For the CMF using sinc function as the impulse response function, the $h_{BPs}(t)$ is selected as:

$$h_{BPs}(t) = \text{sinc}(2 \cdot 50 \cdot t) - \text{sinc}\,(2 \cdot (50-1) \cdot t) \tag{5.3.16}$$

The waveforms and spectra of the input signal and the signal of CMF using the sinc function are illustrated in Fig. 5.26. As can be observed from these plots,

the harmonic component in the signal is detected and removed to a large extent. Furthermore, the amplitude maintains approximately the same value after the convolution process and the time delay can be neglected.

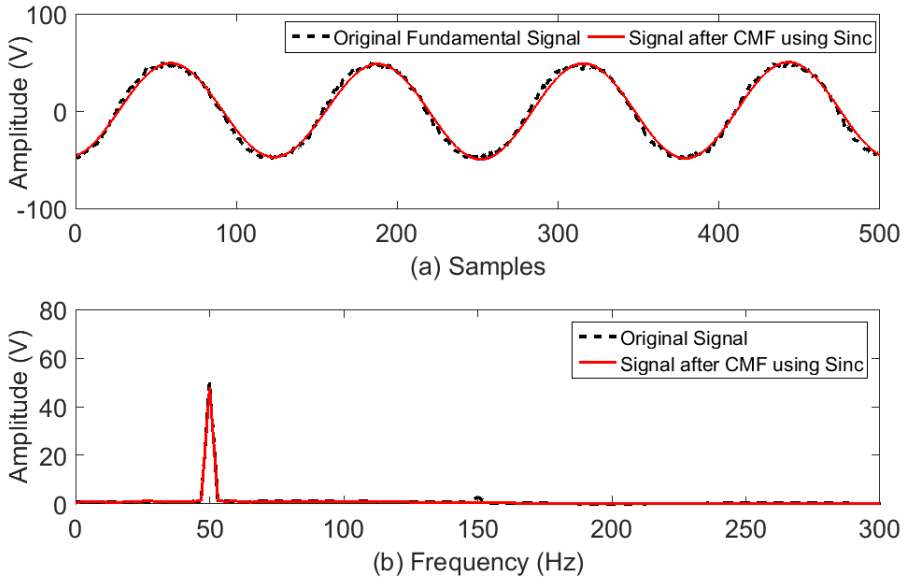

Figure 5.26: (a) The waveforms of the original fundamental signal and the singal after CMF using sinc function (b)The spectra of the input signal and the signal after CMF using the sinc function

The waveforms and spectra of the input signal and the signal of CMF using Dirac delta function are presented in Fig. 5.27. In the Fig. 5.27, there are two different scales in the Y axis. Comparing to the signal after CMF using sinc function, the third harmonic component is also filtered out almost completely. However, as mentioned previously and also shown in the figure, the amplitude of the output signal of CMF using the Dirac delta function increases dramatically. Therefore, it is obvious that the CMF using sinc function has better performance in maintaining the same amplitude while filtering system harmonics effectively and successfully compared to that of the CMF using Dirac delta function. Furthermore, these results further demonstrate that determining appropriate impulse response function in convolution procedure is also of great importance and necessity for improving the performance of CMF in filtering power system harmonics.

Different tests by changing the amplitude and frequency of the harmonic com-

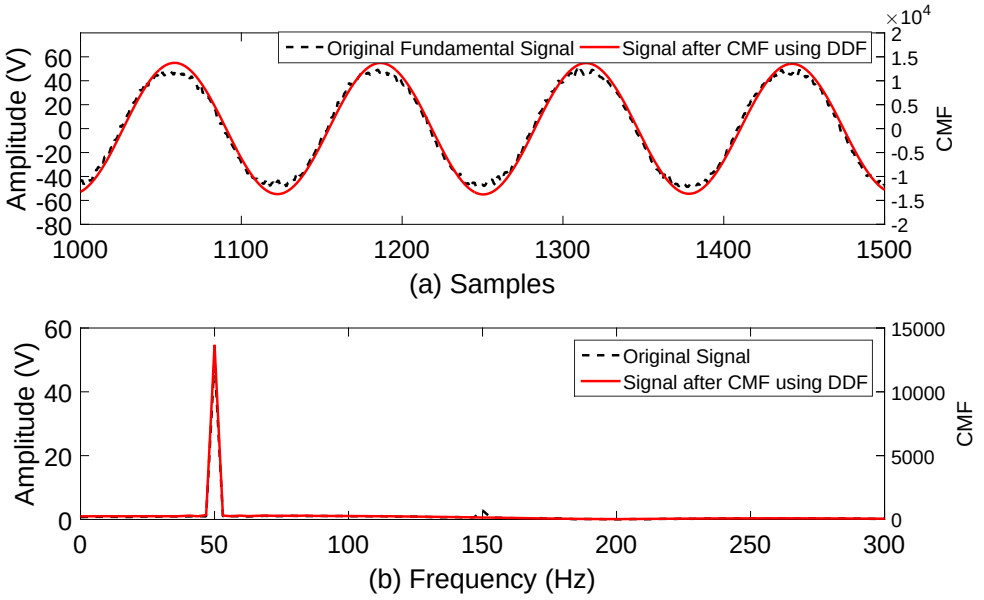

Figure 5.27: (a) The waveforms of the original fundamental signal and the signal after CMF using Dirac delta function (b) The spectra of the input signal and the signal after CMF using the Dirac delta function ($-0.02 < \tau < 0.02$)

ponent have also been simulated. However, when the amplitudes and frequencies of the fundamental frequency component and the harmonic component becomes closer, the performance of the CMF using sinc function is affected dramatically, which expresses as the existence of time delay and distortion of waveform referring to large amounts of simulation studies. Therefore, CMF using sinc function has its advantage in maintaining the amplitude and eliminating harmonic components when the difference between the fundamental frequency component and the harmonic component are obvious.

5.3.5 Harmoincs Removal Results of MF using Optimised SE

According to outcomes in the former sections, CMF with different impulse response functions have several advantages in eliminating harmonic components but also have their limits. Furthermore, the application of MF is limited to noise elimination and partial harmonic removal. As known, SE influences the performance of MF

greatly and different shape and length of SE can lead to different filtering results. As a consequence, the concentration of this section is to obtain better filtering results only applying MF with an optimised SE. The optimisation of SE is performed by using standard PSO.

Standard Particle Swarm Optimisation

A PSO is a population-based optimisation algorithm invented by Kennedy and Eberhart [126], where the population is called a *swarm* and each individual in the population is called a *particle*. It is inspired by computer simulations of various interpretations of the movement of organisms in flock of birds or a school of fish [126].

Formally, an objective (or cost) function f, which must be minimised, is formed and the function takes a candidate solution as argument in the form of a vector of real numbers and produces a real number which indicates the fitness value of the given candidate solution. The target of the PSO algorithm is to find the best optimal solution through several iterations. The i^{th} particle in the k^{th} iteration has a current position in an n-dimensional search space, $X_i^k \in (B_{\text{lo}}, B_{\text{up}})$, and a current velocity Vel_i^k, where B_{lo} and B_{up} indicate the lower and upper boundary of the search space.

After randomly initialising positions and velocities of all particles, the fitness values of each particle and entire generation are evaluated and compared to the best solution it has achieved so far, called personal best value (*pbest*) and the best solution achieved by any particle in the population, called global best value (*gbest*) respectively in every iteration. Afterwards, the particle updates its velocity and position according to the following equations:

$$\begin{aligned} Vel_i^{k+1} &= \omega Vel_i^k + c_1 r_1 (P_i^k - X_i^k) \\ &\quad + c_2 r_2 (P_{\text{g}} - X_i^k) \end{aligned} \tag{5.3.17}$$

$$X_i^{k+1} = X_i^k + Vel_i^{k+1} \tag{5.3.18}$$

where ω is the inertia weight of the particle, which reduces the velocity of the particle each iteration, c_1 and c_2 are the learning factors of the particle, P_i is the best previous position of the i^{th} particle, and P_{g} is the best position among all the particles in the swarm. Normally, r_1, r_2 are two random numbers between (0,1) and ω, c_1, c_2 are set to $\omega = 0.75$, $c_1 = c_2 = 2.05$ [127].

Equation (5.3.18) is a highly-efficient global searching method, which encourages the current individual to move towards the location that has the best fitness value [128]. Following the strategy of finding better positions, the result can be refined through iterative computations. The pseudo code for the standard PSO is listed in Algorithm 1.

Algorithm 1 The Pseudo Code for the standard PSO Algorithm

```
1: procedure SET(k := 0;)
2:    Randomly initialise positions and velocities of all particles;
3:     while k <= MaximumIterations = 300 do
4:         for each particle i in the swarm do
5:             Calculate the fitness value, f(X_i), for the current particle;
6:             Update P_i^k based on the history of fitness values of current par-
   ticles;
7:             Update P_g^k based on the fitness value of the entire generation;
8:             Calculate velocity Vel_i^k;
9:             Update positions X_i^k;
10:        end for
11:       k:=k+1;
12:    end while
13: end procedure
```

In this application, PSO is applied to find the fittest SE for the MF to detect and extract the required frequency component and remove other components. Each particle in the swarm represents one randomly generated SE. The fitness value is calculated by the following formula:

$$f = \sum (f_{\mathrm{o},j} - f_{\mathrm{target},j})^2 \tag{5.3.19}$$

where f_o, j indicates the jth sample of the practical output signal of MF, and $f_{target,j}$ indicates the jth sample of the target output signal which is also the ideal output signal. With the original input signal and the target output signal, the parameters and shape of the fittest SE can be found through several iterations using PSO algorithm. Consequently, the performance of the corresponding MF can be improved. However,

PSO is an optimisation algorithm, based on the simulation of biologic evolution and finding the fittest parameters. Considering the input signal as the environment and large numbers of parameters are "living" in this environment. Through survival of the fittest, the superior parameters can "survive", which are the best parameters to represent the objective function in this case. Hence, it can be understood that the procedure of PSO is totally independent from the objective function. As a consequence, the advantage of PSO is that this method can be applied to solve issues which can not be specifically described, while the main drawback is that the exact time to obtain reliable and stable outcomes is unknown.

In the following, two different simulations on the performance of the optimised MF by varying the desired signal are investigated. The simulation environment is polluted by a 30 dB WGN and the sampling frequency is 6.4 kHz in both scenarios.

Scenario I

The input signal, consisting of a basic power frequency of 50 Hz, a third order harmonic of 150 Hz and a fifth order harmonic of 250 Hz, is expressed as:

$$i(t) = \sin(2\pi \cdot 50\, t + \pi/3) + 0.3\sin(2\pi \cdot 150\, t + \pi/6) + 0.3\sin(2\pi \cdot 250\, t + \pi/6). \quad (5.3.20)$$

The waveform and spectrum of the input signal are shown in Fig. 5.28.

The MF aims to preserve the fundamental signal of 50 Hz and filter out the third and fifth harmonic components. The shape of the fittest SE is shown in Fig. 5.29. Comparing to conventional approaches such as FT that usually use a window with length of one cycle of the fundamental frequency component, the length of the optimised SE is 100 samples which is less than a cycle (128 samples). Moreover, the morphological operators applied in the MF is the combination of *opening* and *closing*, given as:

$$f_{\mathrm{mf}}(t) = \frac{[f_{\mathrm{opcl}} + f_{\mathrm{clop}}]}{2} \quad (5.3.21)$$

With optimised SE, the proposed MF is applied once to the target signal. After applying the optimised SE to the MF, the waveform and spectrum of the output signal after using the optimised MF are shown in Fig. 5.30 and the waveform of the original fundamental signal and the spectrum of the input signal are also presented as the comparison in the same plot.

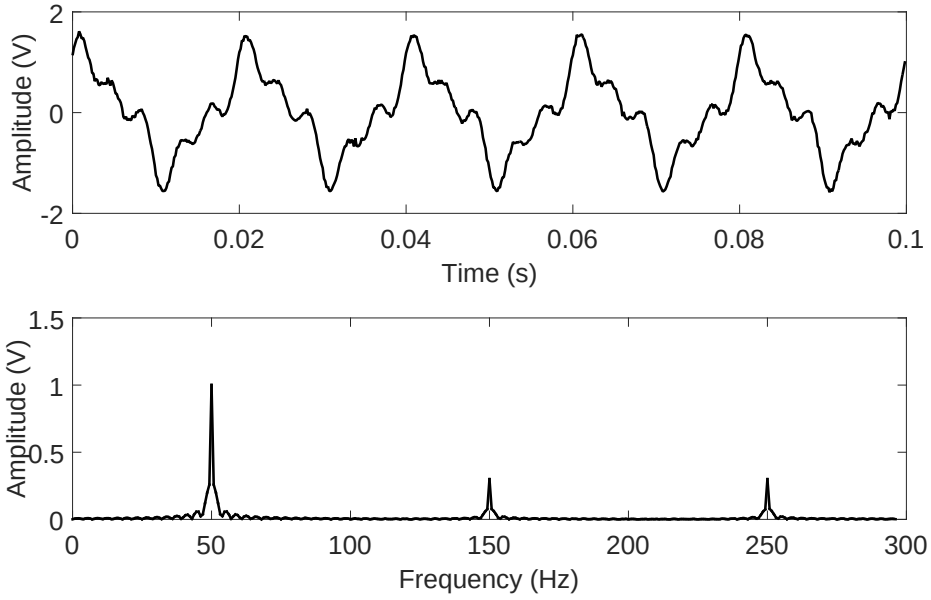

Figure 5.28: The waveform and spectrum of the input signal

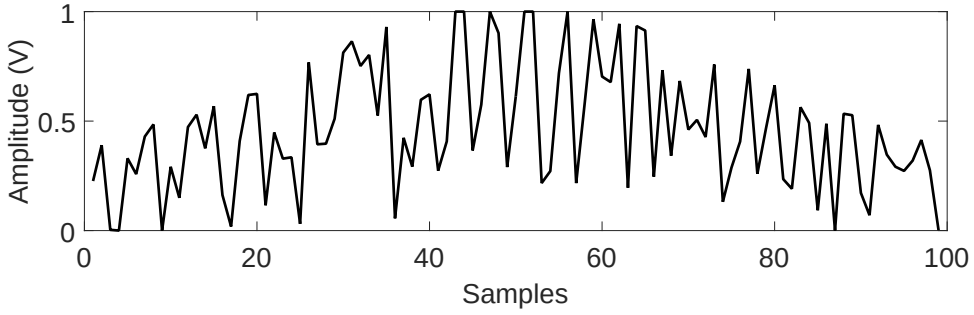

Figure 5.29: The waveform of the optimised SE

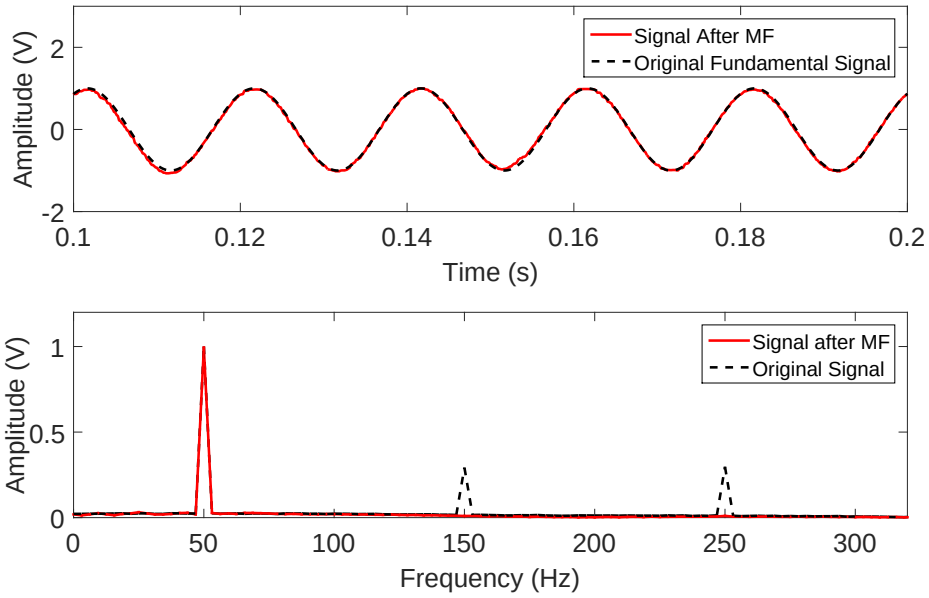

Figure 5.30: The waveforms and spectra of the input signal and the signal after the optimised MF

It is apparent that the filtering result of the proposed MF with the designed SE is unexceptionable and the 50 Hz fundamental signal is preserved successfully and accurately. According to the spectra, the harmonic components are removed completely and the amplitude of the fundamental frequency component remains the same amplitude after filtering by the MF. Even though the output signal of the MF contains very small amount of noise, the filtering effect is dramatically impressive due to the fittest SE in MF design. Moreover, the output signal of MF can be refined by applying a simple filter, the average of erosion and dilation operations. Additionally, although the shape of the optimised SE is serrated and the process of standard PSO takes some computing time, the refined SE provides a reference to select suitable shape and length of SE when designing MF.

It can be observed from Fig. 5.29, the shape of waveform of the MF is similar to half a sinusoidal wave. Therefore, following the optimisation of SE, an SE with the shape of half a sinusoidal wave with the length of 100 samples is selected for the MF in this situation. The results of the MF with the SE referring to the optimised one are illustrated in Fig. 5.31.

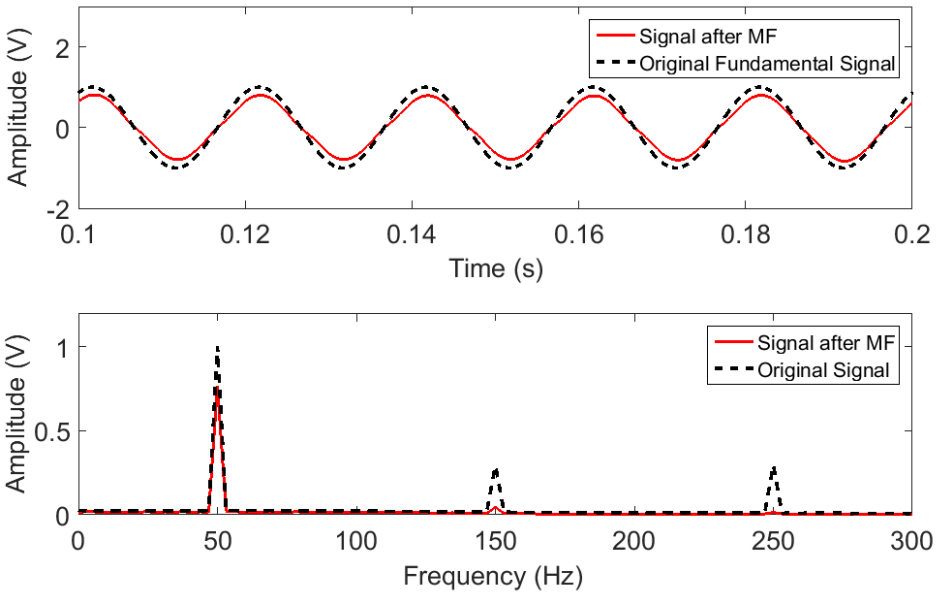

Figure 5.31: The waveforms and spectra of the inut signal and the signal after MF with a half sinusoid SE

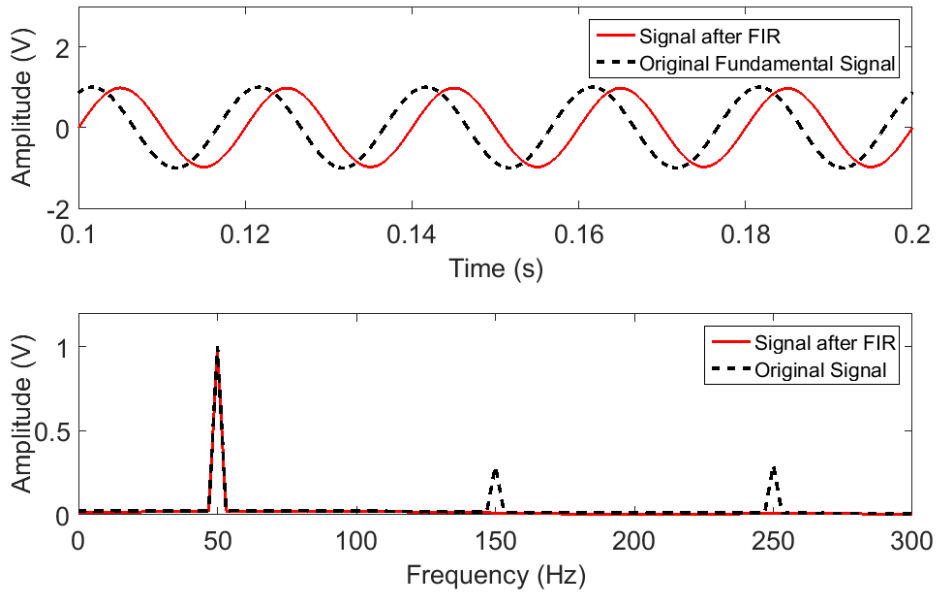

Figure 5.32: The waveforms and spectra of the input signal and the signal after FIR

An FIR bandpass filter is also applied for comparison and the outcomes are presented in Fig. 5.32. In Fig. 5.32, the output signal after using the FIR filter depicts that the shape of the 50 Hz fundamental frequency component is preserved. However, it suffers from an obvious time delay, which is hard to avoid in this type of filters. The time delay is caused by the high order of the FIR filter for better filtering result. In Fig. 5.31, the results shows that there is no time delay while the amplitude reduction of the output signal is acceptable. Comparing these two filters, the proposed MF with the optimised SE has a better performance both in reducing time delay and avoiding large amplitude attenuation when applying to preserve desired frequency component and eliminate undesired ones.

Scenario II

A different simulation is taken by varying the target signal in order to further evaluate the validity of the optimised MF. The input signal is not changed while the desired frequency component has changed from the 50 Hz frequency component to the 150 Hz frequency component. In this scenario, the shape of the optimised SE is changed and it is shown in Fig. 5.33. Both the signal after applying the MF with

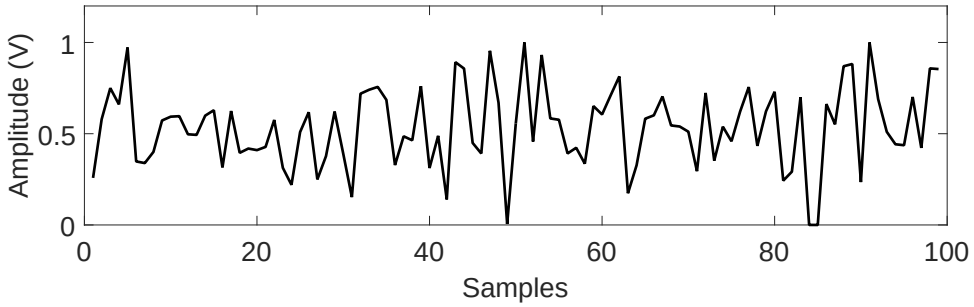

Figure 5.33: The waveform of the optimised SE

the optimised SE and the input signal are displayed in Fig. 5.34. From the results, the 150 Hz frequency component is detected and extracted by the optimised MF and the two remaining components in the input signal is suppressed dramatically. The simulation study also depicts that designing SE by means of standard PSO algorithm can improve the performance of the MF and it also shows the importance of selecting an adequate SE in designing MF. However, the optimisation process takes

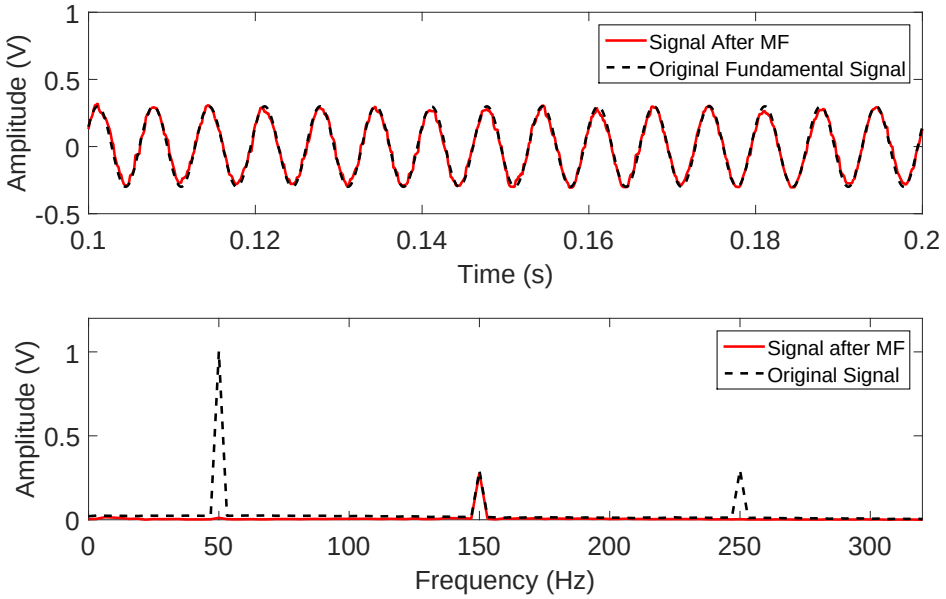

Figure 5.34: The waveform and spectrum of the input signal and the signal after the optimised MF

time to obtain the fittest SE for MF. Although more computation time is required, the optimised SE provides an idea to find the closest shape and length of the SE to the optimised one for achieving better performance and this can benefit the further analysis on selection of proper SE in MM-based algorithms.

5.4 Conclusions

A novel filter CMF, which is the combination of a low-pass MF and convolution, has been introduced and simulated in this chapter. In comparison with general MF, CMF with different impulse response functions are more capable of detecting and eliminating power system harmonics. Furthermore, general MF can remove WGN and partial harmonics in the signal. With the convolution process, the residual harmonics is further reduced and the low frequency noise is also eliminated. Besides simulations on CMF using different impulse response functions, in order to improve the performance of the MF, PSO has been introduced for optimisation of SE and impressive outcomes have also been achieved.

The simulation studies have illustrated that the proposed CMF is able to remove harmonics in power systems even in noisy environments. Generally, MF is able to rapidly extract the signal of desired frequency. However, it influences the shape of the signal and the frequency extracted is not in a very narrow range. Therefore, a convolution operation is combined with MF to overcome the deformation problem. Furthermore, the simulation studies have also demonstrated that CMF can extract the desired frequency component with a narrower band. In comparison with generally used MF, the efficiency and accuracy of elimination of power system harmonics using the proposed CMF are improved to some extent. Moreover, besides the utilisation of Dirac delta function as the impulse response function in convolution, CMF with other impulse response functions have been simulated and compared and they have led to different simulation results. For a specific requirement, determining which impulse response function can be applied in the convolution procedure is of great importance and necessity for improving the performance of CMF in filtering out harmonics. Although some consequences of the CMF are not completely satisfied, the simulations of CMF based on different types of impulse response functions provide useful information and idea for future analysis. Additionally, CMF using FIR as the impulse response function has also been used to extract not only the fundamental frequency component but also other harmonic components, which can be applied for further harmonic analysis, such as estimating the parameters of the harmonics. Besides the improvement in CMF, the enhancement of the performance of MF has also been realised by using PSO to find the fittest SE. With the optimised SE, the refined MF is capable of detecting and reducing undesired frequency component successfully and efficiently. In addition, the optimisation process of SE also provides the idea in discovering better SE (both in shape and length) for the improvement of filtering results using MF.

Chapter 6

Conclusions and Future Work

This chapter concludes the thesis and summarises the achievements of the research work done on MM-based algorithms and their applications to the detection of different disturbances in power systems. Possible directions for future research of advanced morphological operators are also included.

6.1 Conclusions

The objective of this thesis was to develop advanced MM-based algorithms and to apply them to detect different types of disturbances in power systems. MM is a non-linear approach that concentrates on the shape information of a signal or an image, which is totally different from the approach using integral transforms, such as FT and WT. This feature enables MM to initiate a new methodology to deal with these disturbances in power systems and to provide another option over traditional techniques.

The applications of basic morphological operators, such as dilation, erosion, opening and closing, have been developing rapidly in recent years. Apart from the basic operators, development of novel advanced morphological operators, such as multi-resolution decomposition, soft MM, multi-scale MM and MG, has also become one of the main streams in maintaining the stability of power systems. In order to detect and use the information to prevent damage from power quality issues, several other advanced morphological operators have been introduced and analysed in this research, which specifically intend to accomplish the tasks of detection and classi-

fication of typical power quality disturbances, the detection of LFO components in power system signals and the detection and elimination of harmonic components.

For the four types of typical power quality disturbances which exist in most power system signals, including voltage sag, momentary interruption, voltage swell and damped oscillatory transient, an improved MMG with trapezoid SEs has been designed to detect the location and duration of these disturbances. Besides the detection, a basic morphological operator, *closing*, has also been applied together with the extracted feature produced by the MMG for classification of the detected disturbances. Furthermore, it should be noted that the proposed method is able to largely preserve features caused by the power quality disturbances while removing the noise. These two MM-based algorithms have been proved to be simple and easy to implement. High accuracy in the identification of power quality disturbances has been achieved, even in noisy environments.

The core concept of LFO detection is envelope extraction, since the existence of LFO causes changes to the envelope of the power system signal. For the two types of LFO component in most power system signals, two methods have been developed to extract them respectively. In order to detect the continuous LFO components, a hybrid algorithm using an envelope extraction MF and the GSO algorithm has been proposed. The envelope extraction MF, as the name implies, has been applied to extract envelopes of target signals, where the extracted envelope contains the detail information of LFO component. In the following, GSO algorithm has been used to estimate the parameters of the extracted envelopes for reconstruction of the continuous LFO components. Considering severely noisy circumstance, this combinational approach is capable of online detecting continuous LFO components successfully and efficiently. For the extraction of damped LFO components, an LFO extraction MF is utilised to directly detect the existence of these LFO components. Two different power system models are built to generate these two types of LFO components and noisy environments have also taken into consideration during simulation studies. The research results have demonstrated that the proposed LFO extraction MF provides a new angle to deal with LFO and achieves better performance compared to conventional methods.

The thesis has also introduced another novel filter to detect and eliminate harmonic components in power systems. The scheme is the combination of a low-pass

MF and convolution process. Firstly, an MF has been designed to remove noise and partial harmonic components. Secondly, the filtered signal by the MF has been convolved with a pre-designed impulse response function. This hybrid filter is regarded as CMF. Generally, an MF with proper designed SE has the ability to extract the signal of desired frequency while the extracted frequency range is not narrow enough. Hence, the process of convolution has refined the outcomes of MF. Furthermore, besides the application of Dirac delta function as the impulse response function in the convolution, simulation studies on CMF with several other impulse response functions have been carried out to achieve better performance and the results have conveyed that different impulse response functions in CMF can be chosen for different purposes and requirements. Besides the investigation on the performance of CMF using different impulse response functions, the improvement of MF using optimised SE through PSO algorithm has also been achieved for detecting and removing undesired frequency components. Additionally, this has also provided the idea of obtaining SE with proper length and shape for MF. A large number of simulation studies have been undertaken to estimate the performance of the proposed CMF with different impulse response functions and the optimised MF and the outcomes have demonstrated that these methods are capable to deal with harmonics in power systems.

6.2 Future Work

The thesis describes the application of advanced MM-based algorithms in the detection of different disturbances in power systems. The results have proven that MM-based methods have great potential in detecting different disturbances in power systems. Therefore, due to these achievements, the applications of these methods can be further developed to other fields, for example signal/image processing in medical devices. Furthermore, the hybrid scheme of combining MM with other algorithms, such as GSO, PSO and convolution, provides a new way to expand the existing approach based on MM in order to achieve better performance. Additionally, the usage of morphological operators still need to be developed since more combinations of them are under discovered for different purposes and the researches in the thesis still have the potential to be investigated more intensively and completely. Therefore, future work will concentrate on discovering the feasibility of expanding the existing

research work, developing new algorithms based on MM and finding new areas for MM-based approaches. The following aspects would be valuable for further research:

- For the continuation of the research work in this thesis, the performance of the hybrid scheme using the envelope extraction MF and GSO will be further expanded in minimising the influence of noise on amplitude estimation of the LFO and in dealing with signals containing multiple continuous LFO components. Besides these, the potential of the proposed method will also be further developed by applying it to detect and reconstruct damped LFO components.

- More combinations of morphological operators will be investigated. The properties and features of the corresponding operators will also be analysed and these new combinations will be compared to the existing ones for improvement and enhancement. With these newly implemented morphological operators, different MF will be designed to achieve better performance than the existed ones in processing signals with various objectives.

- The previous study on optimisation of SE using standard PSO algorithm has depicted that the performance of MF can greatly improved by selecting an SE with adequate shape and length. The future work will further investigate the influence of different shapes and lengths of SE and generalise a tactic to find the specific and proper SE for MF in order to obtain required filtering results.

- The CMF designed in the thesis has achieved success to some extent and its performance will be further refined by both improving SE and morphological operators in MF and developing impulse response functions in convolution process in the future work. With these development, the new version of CMF will be enhanced and have the ability to extract certain range of frequency components or even single frequency component from target signals.

- The research work in the thesis only obtained the achievements on a theoretical level. Hence, in future work, these algorithms will be embedded into hardware and practical devices in power systems. These may include: to detect and classify different power quality disturbances, to accurately detect and analyse LFO components, to extract certain range of frequency components or single

frequency component and to remove and analyse harmonics in power system signals.

References

[1] J. Serra. *Image Analysis and Mathematical Morphology*. Academic Press, Inc., London, 1982.

[2] J. Serra. Automatic scanning device for analysing textures. Patent, U.S., 3,449,586, July 1969.

[3] G. Matheron. *Elements pour une thorie des milieux poreux*. Masson, Paris, 1967.

[4] J. Serra and P. Soille. *Mathematical Morphology and Its Applications to Image Processing*. Computational Imaging and Vision. Springer Netherlands, 2012.

[5] D. Ryan. *E - learning Modules: DLR Associates Series*. AuthorHouse, 2012.

[6] P. Sun, Q. H. Wu, A. M. Weindling, A. Finkelstein, and K. Ibrahim. An improved morphological approach to background normalization of ecg signals. *Biomedical Engineering, IEEE Transactions on*, 50(1):117–121, Jan 2003.

[7] T. Y. Ji, Z. Lu, Q. H. Wu, and Z. Ji. Baseline normalisation of ecg signals using empirical mode decomposition and mathematical morphology. *Electronics Letters*, 44(2):82–83, January 2008.

[8] L. Koskinen, J. Astola, and Y. Neuvo. Soft morphological filters. volume 1568, pages 262–270, 1991.

[9] A. Gasteratos and I. Andreadis. Soft mathematical morphology: Extensions, algorithms and implementations. In *in: P.W. Hawkes (Ed.), Advances in Imaging and Electron Physics*, pages 63–99. Academic Press, 1999.

[10] P. Kuosmanen and J. Astola. Soft morphological filtering. *Journal of Mathematical Imaging and Vision*, 5(3):231–262, 1995.

[11] T. Y. Ji, Z. Lu, and Q. H. Wu. Detection of power disturbances using morphological gradient wavelet. *Signal Processing*, 88(2):255 – 267, 2008.

[12] A. Gasteratos, I. Andreadis, and Ph. Tsalides. Realisation of soft morphological filters. *Circuits, Devices and Systems, IEE Proceedings*, 145(3):201–206, Jun 1998.

[13] D. Sinha and E. R. Dougherty. Fuzzy mathematical morphology. *J. Vis. Comun. Image Represent.*, 3(3):286–302, September 1992.

[14] I. Bloch and H. Matre. Fuzzy mathematical morphology. *Annals of Mathematics and Artificial Intelligence*, 10(1-2):55–84, 1994.

[15] M. Daoudi, R. Benslimane, D. Hamad, and J.-G. Postaire. A new interactive pattern recognition approach by multilayer neural networks and mathematical morphology. In *Systems, Man and Cybernetics, 1993. 'Systems Engineering in the Service of Humans', Conference Proceedings., International Conference on*, pages 125–130 vol.4, Oct 1993.

[16] M. S. Li, T. Y. Ji, Z. Lu, and Q. H. Wu. Optimal harmonic estimation using dynamic bacterial swarming algorithm. In *Evolutionary Computation, 2008. CEC 2008. (IEEE World Congress on Computational Intelligence). IEEE Congress on*, pages 1302–1308, 2008.

[17] T. Y. Ji, Z. Lu, and Q. H. Wu. A particle swarm optimiser applied to soft morphological filters for periodic noise reduction. In Mario Giacobini, editor, *Applications of Evolutionary Computing*, volume 4448 of *Lecture Notes in Computer Science*, pages 367–374. Springer Berlin Heidelberg, 2007.

[18] M. I. Quintana, R. Poli, and E. Claridge. Morphological algorithm design for binary images using genetic programming. *Genetic Programming and Evolvable Machines*, 7(1):81–102, 2006.

[19] T. Y. Ji, Z. Lu, and Q. H. Wu. Optimal soft morphological filter for periodic noise removal using a particle swarm optimiser with passive congregation. *Signal Processing*, 87(11):2799 – 2809, 2007.

[20] P. Soille. *Morphological Image Analysis: Principles and Applications*. Engineering online library. Springer Berlin Heidelberg, 2004.

[21] T. Y. Ji. *Advanced Mathematical Morphology and Its Applications to Signal Processing*. PhD thesis, University of Liverpool, 2009.

[22] Q. H. Wu, Z. Lu, and T. Y. Ji. *Protective Relaying of Power Systems Using Mathematical Morphology*. Power Systems. Springer London, Limited, 2009.

[23] P. Soille and M. Pesaresi. Advances in mathematical morphology applied to geoscience and remote sensing. *Geoscience and Remote Sensing, IEEE Transactions on*, 40(9):2042–2055, Sep 2002.

[24] P. Maragos. Morphological filtering for image enhancement and feature detection. In AL BOVIK, editor, *Handbook of Image and Video Processing (Second Edition)*, Communications, Networking and Multimedia, pages 135 – 156. Academic Press, Burlington, second edition edition, 2005.

[25] C. Martel, G. Flouzat, A. Souriau, and F. Safa. A morphological method of geometric analysis of images: Application to the gravity anomalies in the indian ocean. *Journal of Geophysical Research: Solid Earth*, 94(B2):1715–1726, 1989.

[26] T. Chen, Q. H. Wu, R. Rahmani-Torkaman, and J. Hughes. A pseudo top-hat mathematical morphological approach to edge detection in dark regions. *Pattern Recognition*, 35(1):199 – 210, 2002.

[27] F. Meyer and S. Beucher. Morphological segmentation. *Journal of Visual Communication and Image Representation*, 1(1):21 – 46, 1990.

[28] M. H. Sedaaghi and Q. H. Wu. Real-time implementation of grey-scale morphological operators. *Electronics Letters*, 33(21):1761–1763, 1997.

[29] L. Vincent. Morphological grayscale reconstruction in image analysis: applications and efficient algorithms. *Image Processing, IEEE Transactions on*, 2(2):176–201, Apr 1993.

[30] *An image similarity measure method based on mathematical morphology*, volume 9301, 2014.

[31] J. M. F. Moura. What is signal processing. *Signal Processing Magazine, IEEE*, 26(6):6–6, Nov 2009.

[32] J. Buse, D. Y. Shi, T. Y. Ji, and Q. H. Wu. Decaying dc offset removal operator using mathematical morphology for phasor measurement. In *Innovative Smart Grid Technologies Conference Europe (ISGT Europe), 2010 IEEE PES*, pages 1–6, Oct 2010.

[33] J. N. Yang, J. Sun, and J. Ni. Removing dc offset and de-noising for inspecting signal based on mathematical morphology filter processing. In *Proceedings of SPIE - The International Society for Optical Engineering*, Dec 2008.

[34] C. Z. Li and J. J. Cheng. Mathematical morphological filter and its application in removing noises in vibration signal. In *Electronic Measurement and Instruments, 2007. ICEMI '07. 8th International Conference on*, pages 4–101–4–104, Aug 2007.

[35] Z. Lu, J. S. Smith, and Q. H. Wu. Morphological lifting scheme for current transformer saturation detection and compensation. *Circuits and Systems I: Regular Papers, IEEE Transactions on*, 55(10):3349–3357, Nov 2008.

[36] T. Y. Ji, Q. H. Wu, W. H. Tang, and L. Jiang. A morphological scheme for the correction of ct saturation waveforms. In *Power and Energy Society General Meeting, 2011 IEEE*, pages 1–7, July 2011.

[37] T. Y. Ji, M. S. Li, and Q. H. Wu. Phasor measurement and ct saturation compensation through embedding. In *Power and Energy Society General Meeting (PES), 2013 IEEE*, pages 1–5, July 2013.

[38] Z. Lu, T. Y. Ji, and Q. H. Wu. Ehv transmission line protection using a morphological lifting scheme. *Electric Power Systems Research*, 79(10):1384 – 1392, 2009.

[39] Q. H. Wu, J. F. Zhang, and D. J. Zhang. Ultra-high-speed directional protection of transmission lines using mathematical morphology. *Power Delivery, IEEE Transactions on*, 18(4):1127–1133, 2003.

[40] G. T. Heydt. *Electrical Power Quality.* West LaFayette, IN : Stars in a Circle Publications, Indiana, USA, 1991,.

[41] G. T. Heydt. Electric power quality: a tutorial introduction. *Computer Applications in Power, IEEE*, 11(1):15–19, Jan 1998.

[42] D. D. Sabin and A. Sundaram. Quality enhances reliability [power supplies]. *Spectrum, IEEE*, 33(2):34–41, Feb 1996.

[43] L. Angrisani, P. Daponte, M. D'Apuzzo, and A. Testa. A measurement method based on the wavelet transform for power quality analysis. *Power Delivery, IEEE Transactions on*, 13(4):990–998, 1998.

[44] Ieee recommended practice for monitoring electric power quality. *IEEE Std 1159-2009 (Revision of IEEE Std 1159-1995)*, pages c1–81, June 2009.

[45] S. Chattopadhyay, M. Mitra, and S. Sengupta. *Electric Power Quality*. Power Systems. Springer Netherlands, 2011.

[46] J. Chen, J. S. Thorp, and M. Parashar. Analysis of electric power system disturbance data. In *System Sciences, 2001. Proceedings of the 34th Annual Hawaii International Conference on*, pages 738–744, Jan 2001.

[47] M. Yao, R. R. Shoults, and R. Kelm. Agc logic based on nerc's new control performance standard and disturbance control standard. *Power Systems, IEEE Transactions on*, 15(2):852–857, May 2000.

[48] J. S. Thorp, A. G. Phadke, S. H. Horowitz, and S. Tamronglak. Anatomy of power system disturbances: importance sampling. *International Journal of Electrical Power and Energy Systems*, 20(2):147 – 152, 1998.

[49] P. Hines, J. Apt, and S. Talukdar. Large blackouts in north america: Historical trends and policy implications. *Energy Policy*, 37(12):5249 – 5259, 2009.

[50] M. A. Ibrahim. *Disturbance Analysis for Power Systems*. John Wiley and Sons, Inc., 2011.

[51] Z. Lu, J. S. Smith, Q. H. Wu, and J. Fitch. Identification of power disturbances using the morphological transform. *Transactions of the Institute of Measurement and Control*, 28(5):441–455, 2006.

[52] M. A. S. Masoum, S. Jamali, and N. Ghaffarzadeh. Detection and classification of power quality disturbances using discrete wavelet transform and wavelet networks. *Science, Measurement Technology, IET*, 4(4):193–205, 2010.

[53] R. M. Haralick, S. R. Sternberg, and X. H. Zhuang. Image analysis using mathematical morphology. *Pattern Analysis and Machine Intelligence, IEEE Transactions on*, PAMI-9(4):532–550, 1987.

[54] P. Wang and S. G. Liu. Application of mathematical morphological operator in power fault signal detection. In *Electrical and Control Engineering (ICECE), 2011 International Conference on*, pages 1000–1003, 2011.

[55] L. Zhang, Y. P. Lv, and H. Yin. A multi-resolution morphology gradient based non-communication protection scheme for transmission lines. In *Electric Utility Deregulation and Restructuring and Power Technologies, 2008. DRPT 2008. Third International Conference on*, pages 1608–1613, 2008.

[56] D. Yang, C. Rehtanz, Y. Li, and D. Yang. A hybrid method and its applications to analyse the low frequency oscillations in the interconnected power system. *Generation, Transmission Distribution, IET*, 7(8):874–884, 2013.

[57] Y. Yuan, Y. Sun, L. Cheng, G. Chen, and P. Wang. Power system low frequency oscillation monitoring and analysis based on multi-signal online identification. *Science China Technological Sciences*, 53(9):2589–2596, 2010.

[58] D. C. Yang, C. Rehtanz, and Y. Li. Analysis of low frequency oscillations using improved hilbert-huang transform. In *Power System Technology (POWERCON), 2010 International Conference on*, pages 1–7, 2010.

[59] J. L. Rueda, C. A. Juarez, and I. Erlich. Wavelet-based analysis of power system low-frequency electromechanical oscillations. *Power Systems, IEEE Transactions on*, 26(3):1733–1743, 2011.

[60] K. Prasertwong, N. Mithulananthan, and D. Thakur. Understanding low-frequency oscillation in power systems. *International Journal of Electrical Engineering Education*, 47(3):248–262, 2010.

[61] M. C. J. Angammana. Analytical study of factors affecting to electromechanical oscillations in power systems. Master's thesis, Asian Institute of Technolog, May 2006.

[62] A. R. Messina. *Inter-area Oscillations in Power Systems: A Nonlinear and Nonstationary Perspective*. Springer Publishing Company, Incorporated, 1st edition, 2009.

[63] K. Prasertwong, N. Mithulananthan, and D. Thakur. Understanding low-frequency oscillation in power systems. *International Journal of Electrical Engineering Education*, 2010.

[64] X. Li, Q. W. Gong, and J. J. Jia. A detection method for low frequency oscillation dominant modes based on atomic decomposition energy entropy. *Proceeding of the CSEE*, 32(1):131, 2012.

[65] P. Tripathy, S. C. Srivastava, and S. N. Singh. A modified tls-esprit-based method for low-frequency mode identification in power systems utilizing synchrophasor measurements. *Power Systems, IEEE Transactions on*, 26(2):719–727, 2011.

[66] D. S. Laila, A. R. Messina, and B. C. Pal. A refined hilbert-huang transform with applications to interarea oscillation monitoring. *Power Systems, IEEE Transactions on*, 24(2):610–620, 2009.

[67] J. J. Sanchez-Gasca and J. H. Chow. Performance comparison of three identification methods for the analysis of electromechanical oscillations. *Power Systems, IEEE Transactions on*, 14(3):995–1002, 1999.

[68] E. Martinez and A. R. Messina. Modal analysis of measured inter-area oscillations in the mexican interconnected system: The july 31, 2008 event. In *Power and Energy Society General Meeting, 2011 IEEE*, pages 1–8, 2011.

[69] M. Jafarian and A. M. Ranjbar. Interaction of the dynamics of doubly fed wind generators with power system electromechanical oscillations. *Renewable Power Generation, IET*, 7(2):89–97, 2013.

[70] C. E. Grund, J. J. Paserba, J. F. Hauer, and S. L. Nilsson. Comparison of prony and eigenanalysis for power system control design. *Power Systems, IEEE Transactions on*, 8(3):964–971, 1993.

[71] A. E. Sarasua, C. Rehtanz, E. Handschin, and P. E. Mercado. Analysis of system-inherent oscillations in power systems with several load models. In *Power Tech Proceedings, 2001 IEEE Porto*, volume 4, page 6 pp. vol.4, 2001.

[72] J. J. Sanchez-Gasca, V. Vittal, M. J. Gibbard, A. R. Messina, D. J. Vowles, S. Liu, and U. D. Annakkage. Analysis of higher order terms for small signal stability analysis. In *Power Engineering Society General Meeting, 2005. IEEE*, pages 1745–1753 Vol. 2, 2005.

[73] M. J. Gibbard, N. Martins, J. J. Sanchez-Gasca, N. Uchida, V. Vittal, and L. Wang. Recent applications of linear analysis techniques. *Power Systems, IEEE Transactions on*, 16(1):154–162, 2001.

[74] D. J. Trudnowski, J. W. Pierre, N. Zhou, J. F. Hauer, and M. Parashar. Performance of three mode-meter block-processing algorithms for automated dynamic stability assessment. *Power Systems, IEEE Transactions on*, 23(2):680–690, 2008.

[75] T. J. Browne, V. Vittal, G. T. Heydt, and A. R. Messina. A comparative assessment of two techniques for modal identification from power system measurements. *Power Systems, IEEE Transactions on*, 23(3):1408–1415, 2008.

[76] M. Meunier and F. Brouaye. Fourier transform, wavelets, prony analysis: tools for harmonics and quality of power. In *Harmonics and Quality of Power Proceedings, 1998. Proceedings. 8th International Conference On*, volume 1, pages 71–76 vol.1, 1998.

[77] D. R. Ostojic. Spectral monitoring of power system dynamic performances. *Power Systems, IEEE Transactions on*, 8(2):445–451, 1993.

[78] A. R. Messina and V. Vittal. Nonlinear, non-stationary analysis of interarea oscillations via hilbert spectral analysis. *Power Systems, IEEE Transactions on*, 21(3):1234–1241, 2006.

[79] A. R. Messina, V. Vittal, D. Ruiz-Vega, and G. Enriquez-Harper. Interpretation and visualization of wide-area pmu measurements using hilbert analysis. *Power Systems, IEEE Transactions on*, 21(4):1763–1771, 2006.

[80] Z. H. Wu and N. E. Huang. A study of the characteristics of white noise using the empirical mode decomposition method. *Proceedings of the Royal Society of London. Series A: Mathematical, Physical and Engineering Sciences*, 460(2046):1597–1611, 2004.

[81] J. F. Hauer. Application of prony analysis to the determination of modal content and equivalent models for measured power system response. *Power Systems, IEEE Transactions on*, 6(3):1062–1068, 1991.

[82] J. A. de la O Serna. Synchrophasor estimation using prony's method. *Instrumentation and Measurement, IEEE Transactions on*, 62(8):2119–2128, Aug 2013.

[83] V. S. Patil, P. P. Jambhulkar, and V. P. Kamble. Real-time identification of electromechanical modes using controlled window-size multi-prony analysis. *International Journal of Engineering Research and Technology (IJERT)*, 3(4):1627–1634, Nov 2014.

[84] S. Bruno, M. De Benedictis, and M. La Scala. Taking the pulse of power systems: Monitoring oscillations by wavelet analysis and wide area measurement system. In *Power Systems Conference and Exposition, 2006. PSCE '06. 2006 IEEE PES*, pages 436–443, 2006.

[85] S. L. Chen, J. J. Liu, and H. C. Lai. Wavelet analysis for identification of damping ratios and natural frequencies. *Journal of Sound and Vibration*, 323(12):130 – 147, 2009.

[86] S. He, Q.H. Wu, and J.R. Saunders. Group search optimiser: An optimisation algorithm inspired by animal searching behavior. *Evolutionary Computation, IEEE Transactions on*, 13(5):973–990, Oct 2009.

[87] H. Akagi. New trends in active filters for power conditioning. *Industry Applications, IEEE Transactions on*, 32(6):1312–1322, 1996.

[88] Z. Lu, Q. H. Wu, and J. Fitch. A morphological filter for estimation of power system harmonics. In *Power System Technology, 2006. PowerCon 2006. International Conference on*, pages 1–5, 2006.

[89] T. L. Lee, J. C. Li, and P. T. Cheng. Discrete frequency tuning active filter for power system harmonics. *Power Electronics, IEEE Transactions on*, 24(5):1209–1217, 2009.

[90] P. Rodriguez, J. I. Candela, A. Luna, L. Asiminoaei, R. Teodorescu, and F. Blaabjerg. Current harmonics cancellation in three-phase four-wire systems by using a four-branch star filtering topology. *Power Electronics, IEEE Transactions on*, 24(8):1939–1950, 2009.

[91] M. Cirrincione, M. Pucci, G. Vitale, and A. Miraoui. Current harmonic compensation by a single-phase shunt active power filter controlled by adaptive neural filtering. *Industrial Electronics, IEEE Transactions on*, 56(8):3128–3143, 2009.

[92] Z. Zheng and C. Wang. Measures of suppressing harmonic pollution generated by power electronic equipment. In *Power and Energy Engineering Conference, 2009. APPEEC 2009. Asia-Pacific*, pages 1–4, March 2009.

[93] Q. Wang, W. Yao, and Z. Wang. A study about influence of high and low pass filters on detecting effect of harmonics detection circuits. *Transactions of China Electrotechnical Society*, 1999.

[94] M. T. Chen and Z. M. Yu. Determination of frequency variation effect on dft-based algorithms for harmonic and flicker measurements. In *Transmission and Distribution Conference and Exposition, 2003 IEEE PES*, volume 1, pages 422–427 Vol.1, Sept 2003.

[95] C. I. Chen, G. W. Chang, R. C. Hong, and H. M. Li. Extended real model of kalman filter for time-varying harmonics estimation. *Power Delivery, IEEE Transactions on*, 25(1):17–26, 2010.

[96] H. Ma and A. A. Girgis. Identification and tracking of harmonic sources in a power system using a kalman filter. *Power Delivery, IEEE Transactions on*, 11(3):1659–1665, Jul 1996.

[97] Y. N. Fei, Z. Lu, W. H. Tang, and Q. H. Wu. Harmonic estimation using a global search optimiser. In *EvoWorkshops*, volume 4448 of *Lecture Notes in Computer Science*, pages 261–270. Springer, 2007.

[98] R. N. Ray, D. Chatterjee, and S. K. Goswami. Harmonics elimination in a multilevel inverter using the particle swarm optimisation technique. *Power Electronics, IET*, 2(6):646–652, 2009.

[99] L. Holanda, R. Rabelo, M. Lemos, and D. Barbosa. Power system harmonics estimation using clonal selection algorithm. *Latin America Transactions, IEEE (Revista IEEE America Latina)*, 11(1):525–530, 2013.

[100] P. Vogel. Discrete-time lti systems beyond convolution. *Signal Processing, IEEE Transactions on*, 60(8):4055–4064, 2012.

[101] M. H. Sedaaghi. *Morphological Filtering in Signal/image Processing.* PhD thesis, University of Liverpool, 1998.

[102] J. Mattioli. Minkowski operations and vector spaces. *Set-Valued Analysis*, 3(1):33–50, 1995.

[103] Z. Lu. *Development of advanced power system protection and power quality measurement algorithms using mathematical morphology.* PhD thesis, University of Liverpool, 2006.

[104] S. R. Sternberg. Grayscale morphology. *Computer Vision, Graphics, and Image Processing*, 35(3):333 – 355, 1986. Special Section on Mathematical Morphology.

[105] R. van den Boomgaard. *DMathematical morphology: Extensions towards computer vision.* PhD thesis, University of Amsterdam, 1992.

[106] E. R. Dougherty. *An introduction to morphological image processing.* Tutorial texts in optical engineering. SPIE Optical Engineering Press, 1992.

[107] J. F. Rivest, P. Soille, and S. Beucher. Morphological gradients. *Journal of Electronic Imaging*, 2(4):326–336, 1993.

[108] X. N. Lin, L. Zou, Q. Tian, H. L. Weng, and P. Liu. A series multiresolution morphological gradient-based criterion to identify ct saturation. *Power Delivery, IEEE Transactions on*, 21(3):1169–1175, July 2006.

[109] D. J. Zhang, Q. Li, J. F. Zhang, Q. H. Wu, and D. R. Turner. Improving the accuracy of single-ended transient fault locators using mathematical morphology. In *Power System Technology, 2002. Proceedings. PowerCon 2002. International Conference on*, volume 2, pages 788–792 vol.2, 2002.

[110] J. Serra and L. Vincent. An overview of morphological filtering. *Circuits, Systems and Signal Processing*, 11(1):47–108, 1992.

[111] D. Lauria and C. Pisani. On hilbert transform methods for low frequency oscillations detection. *Generation, Transmission Distribution, IET*, 8(6):1061–1074, Jun 2014.

[112] P. Kundur. *Power System Stability And Control*. EPRI power system engineering series. McGraw-Hill, 1994.

[113] M. Klein, G. J. Rogers, S. Moorty, and P. Kundur. Analytical investigation of factors influencing power system stabilizers performance. *Energy Conversion, IEEE Transactions on*, 7(3):382–390, Sep 1992.

[114] *IEEE Standard for Synchrophasors for Power Systems*. IEEE Std C37. 118. 1-2011 (Revision of IEEE Std C37. 118-2005), 2011.

[115] S. Das and T. Sidhu. A simple synchrophasor estimation algorithm considering ieee standard c37.118.1-2011 and protection requirements. *Instrumentation and Measurement, IEEE Transactions on*, 62(10):2704–2715, Oct 2013.

[116] R. K. Mai, L. Fu, Z. Y. Dong, B. Kirby, and Z. Q. Bo. An adaptive dynamic phasor estimator considering dc offset for pmu applications. *Power Delivery, IEEE Transactions on*, 26(3):1744–1754, Jul 2011.

[117] K. Binder and D. Heermann. *Monte Carlo Simulation in Statistical Physics: An Introduction*. Graduate Texts in Physics. Springer Science & Business Media, 2010.

[118] P. F. Ribeiro, C. A. Duque, P. M. Ribeiro, and A. S. Cerqueira. *Power Systems Signal Processing for Smart Grids*. Wiley, 2013.

[119] F. Fooladgar, S. Samavi, S. M. R. Soroushmehr, and S. Shirani. Geometrical analysis of localization error in stereo vision systems. *Sensors Journal, IEEE*, 13(11):4236–4246, Nov 2013.

[120] G. Bianchi. *Electronic Filter Simulation & Design*. McGraw-Hill Education, 2007.

[121] A. Antoniou. *Digital signal processing*. McGraw-Hill Education, 2006.

[122] M. L. Liu and Y. Guo. *Basic Tutorial of Digital Signal Processing*. Beijing University of Aeronautics and Astronautics Press, 2011.

[123] S. Butterworth. On the Theory of Filter Amplifiers. *Wireless Engineer*, 7, 1930.

[124] J. Treichler. Notes on the design of optimal fir filters. Technical report, Connexions, 2009.

[125] P. M. Woodward and I. L. Davies. Information theory and inverse probability in telecommunication. *Proceedings of the IEE - Part III: Radio and Communication Engineering*, 99(58):37–44, March 1952.

[126] J. Kennedy and R. Eberhart. Particle swarm optimization. In *Neural Networks, 1995. Proceedings., IEEE International Conference on*, volume 4, pages 1942–1948 vol.4, Nov 1995.

[127] M. Clerc and J. Kennedy. The particle swarm - explosion, stability, and convergence in a multidimensional complex space. *Evolutionary Computation, IEEE Transactions on*, 6(1):58–73, Feb 2002.

[128] M. S. Li. *Bacteria-inspired algorithms and their applications to power system optimisation*. PhD thesis, University of Liverpool, 2010.